

DESIGN AND IMPLEMENTATION OF HIGH FILL FACTOR STRUCTURES
ON LOW-COST UNCOOLED INFRARED SENSORS

A THESIS SUBMITTED TO
THE GRADUATE SCHOOL OF NATURAL AND APPLIED SCIENCES
OF
MIDDLE EAST TECHNICAL UNIVERSITY

BY

OZAN ERTÜRK

IN PARTIAL FULFILLMENT OF THE REQUIREMENTS
FOR
THE DEGREE OF MASTER OF SCIENCE
IN
ELECTRICAL AND ELECTRONICS ENGINEERING

SEPTEMBER 2015

Approval of the thesis:

**DESIGN AND IMPLEMENTATION OF HIGH FILL FACTOR
STRUCTURES ON LOW-COST UNCOOLED INFRARED SENSORS**

submitted by **OZAN ERTÜRK** in partial fulfillment of the requirements for the degree of **Master of Science in Electrical and Electronics Engineering Department, Middle East Technical University** by,

Prof. Dr. Gülbin Dural Ünver
Dean, Graduate School of **Natural and Applied Sciences**

Prof. Dr. Gönül Turhan Sayan
Head of Department, **Electrical and Electronics Eng.**

Prof. Dr. Tayfun Akın
Supervisor, **Electrical and Electronics Eng. Dept., METU**

Examining Committee Members

Prof. Dr. Haluk Külâh
Electrical and Electronics Eng. Dept., METU

Prof. Dr. Tayfun Akın
Electrical and Electronics Eng. Dept., METU

Assist. Prof. Dr. Kıvanç Azgın
Mechanical Eng. Dept., METU

Assist. Prof. Dr. Mehmet Ünlü
Electrical and Electronics Eng. Dept., YBU

Assist. Prof. Dr. Mahmud Yusuf Tanrıkulu
Electrical and Electronics Eng. Dept., ADANA STU

Date:

I hereby declare that all information in this document has been obtained and presented in accordance with academic rules and ethical conduct. I also declare that, as required by these rules and conduct, I have fully cited and referenced all referenced material and results that are not original to this work.

Name, Surname: Ozan Ertürk

Signature:

ABSTRACT

DESIGN AND IMPLEMENTATION OF HIGH FILL FACTOR STRUCTURES ON LOW-COST UNCOOLED INFRARED SENSORS

Ertürk, Ozan

M.S., Department of Electrical and Electronics Engineering

Supervisor: Prof. Dr. Tayfun Akın

September 2015, 122 pages

This thesis presents the design and implementation steps of high fill factor structures for existing SOI diode low-cost microbolometer FPAs. Advancements in uncooled infrared detectors enable high performance military grade uncooled microbolometers as well as ultra-low-cost infrared imagers for civilian applications. The trend in uncooled microbolometers to reduce the pixel pitch has become increasingly significant to lower the cost of detector and system integration due to optics, and increase spatial resolution with range. However, reducing pixel size reduces the temperature sensitive area, not to mention the need for larger space to design longer thermal isolation legs. Therefore, many uncooled infrared imaging arrays employ additional structures that increase the fill factor. A second level of sacrificial layer is used to form the high fill factor structure (referred as umbrella) to form an optical cavity in order to maximize the absorption.

This study demonstrates the design of umbrella layer in mechanical, thermal, and optical domain by providing simulations and examples from the literature. Challenges and optimization steps of realizing the umbrella structure are also conveyed. Successful implementation of umbrella structures onto SOI diode pixels with pixel sizes of 50 μm and 70 μm is demonstrated. The fill factor of the low-cost detector pixels with 50 μm pitch is increased from 46 % to 92 % while the fill factor of the pixels with 70 μm pitch is increased from 36 % to 94 %.

The umbrella integrated FPAs are tested under vacuum conditions to obtain responsivity data and evaluate the contribution to the signal generated by addition of umbrella structures. It is concluded that the addition of umbrella structures improve the responsivity of FPAs with 50 μm pitch pixels by 30 % while the responsivity of FPAs with 70 μm pitch pixels is improved by 40 %.

Keywords: Uncooled Infrared Detectors, Microbolometers, Fill Factor, Uncooled Infrared Focal Plane Array, MEMS Fabrication.

ÖZ

YÜKSEK DOLULUK ORANLI YAPILARIN DÜŞÜK MALİYETLİ KIZILÖTESİ DEDEKTÖRLER ÜZERİNE TASARIMI VE UYGULAMASI

Ertürk, Ozan

Yüksek Lisans, Elektrik ve Elektronik Mühendisliği Bölümü

Tez Yöneticisi: Prof. Dr. Tayfun Akın

Eylül 2015, 122 sayfa

Bu tez, diyot tipli düşük maliyetli kızılötesi odak düzlem matrisi (ODM) üzerine oluşturulan yüksek doluluk oranlı yapıların tasarımını ve üretim süreçlerini sunmaktadır. Soğutmasız dedektör alanında yapılan gelişmeler sayesinde yüksek performanslı askeri amaçlı mikrobolometreler ve çok düşük maliyetli sivil amaçlı mikrobolometreler üretilmektedir. Dedektör boyutunu küçültme yönündeki eğilimler, dedektör üretim maliyetini ve sistem maliyetini düşürmek ve uzamsal çözünürlüğü ve menzili artırmak amacıyla önem kazanmıştır. Fakat, dedektör boyutunu küçültürken, ısıya duyarlı aktif alanı da küçülmekte; ayrıca aktif alanın toplam dedektör boyutuna olan oranı da ısı izolasyonu yapılarına duyulan daha büyük alandan dolayı büyük ölçüde azalmaktadır. Bunun sonucu olarak birçok soğutmasız kızılötesi dedektör dizilimi sonradan eklenen doluluk oranını artırıcı yapılar kullanılmaktadır. İkinci bir feda katmanı kullanılarak yapılan doluluk oranı

artırıcı (şemsiye olarak adlandırılan) yapılar optik boşluk oluşturarak emilimi mümkün olduğu kadar yükseltmeyi hedeflemektedir.

Bu çalışma şemsiye yapıların tasarımını mekanik, termal, ve optik alanlarda yapılan simulasyonlarla ve verilen örneklerle desteklemektedir. Ayrıca, şemsiye yapıları üretimi sırasında çıkan zorluk ve optimizasyon süreçleri de aktarılmıştır. Şemsiye yapılarının 50 µm ve 70 µm boyutlarındaki sensörlere başarılı bir şekilde uygulanması gösterilmiştir. Doluluk oranı 50 µm boyutundaki dedektörlerde % 46'dan % 92'ye ve 70 µm boyutundaki dedektörlerde % 36'dan % 92'ye çıkarılmıştır.

Şemsiye yapıları içeren ODM'ler vakum ortamında duyarlılık testi ile ölçülmüş ve performansları değerlendirilmiştir. Şemsiye yapıları, 50 boyutundaki dedektörlerin duyarlılığını % 30 ve 70 boyutundaki dedektörlerin duyarlılığını % 40 artırmıştır.

Anahtar Kelimeler: Soğutmasız Kızılötesi Dedektör, Mikrobolometre, Doluluk Oranı, Soğutmasız Kızılötesi Odak Düzlem Matrisi, MEMS Üretimi

To,

My dearly loved ones who remind me, as the ax bites into the wood, to be comforted in the fact that the ache in our heart and the confusion in our soul means that we are still alive, still human, and still open to the beauty of the world, even though we have done nothing to deserve it.

ACKNOWLEDGEMENTS

First of all, I would like thank to my thesis advisor Prof. Dr. Tayfun Akın for his support, guidance, and encouragement during my graduate studies. I also would like to thank to Assist. Prof. Yusuf Tanrikulu for his support and help throughout my research. Special thanks to Orhan Şevket Akar, for his valuable presence and assistance.

I would like to thank the METU-MEMS members, Özgecan Dervişoğlu, Ramazan Çetin, Başak Kebabcı, Mert Torunbalcı, Adem Saraç, Mustafa Yıldırım, Evren Erdil, Taylan Töral, Ahmet Murat Yağcı, Akın Aydemir, Selçuk Keskin, Eren Çanga, Talha Köse, Hasan Doğan Gavcar, Gülşah Demirhan, Eyüp Can Demir, Oğuzhan Temel, Yunus Terzioglu, Ulaş Aykutlu, Ferhat Yeşil.

I would like to express my gratitude to entire MikroSens family -that is not noted here completely- Firat Tankut being the first, Beril Uğur, Bilge Temiz, Feyza Oruç, and Murat Tepegöz.

Last, but not least, I would like to thank to my dearly loved family members Sefer and İsmigül Ertürk, Hafize Karaca, Emir and Uçcaryılmaz family for their endless support, love, and encouragement. As for the spark of life, I would like to thank to my companion for everything we have been through.

TABLE OF CONTENTS

ABSTRACT	v
ÖZ	vii
ACKNOWLEDGEMENTS	x
TABLE OF CONTENTS	xi
LIST OF FIGURES	xiii
LIST OF TABLES	xxiii
CHAPTERS	
1. INTRODUCTION	1
1.1 Infrared Detector Types	2
1.1.1 Thermoelectric Detectors	3
1.1.2 Pyroelectric Detectors	4
1.1.3 Microbolometers	5
1.2 Performance Parameters of Uncooled Microbolometers	7
1.2.1 Temperature Sensitivity	7
1.2.2 Responsivity	8
1.2.3 Noise Equivalent Temperature Difference (NETD)	10
1.3 Low-cost Infrared Detectors Developed at METU MEMS	11
1.4 Absorption Enhancement in Pixel Level	15
1.4.1 Diode-type Microbolometers employing high fill factor designs	16
1.4.2 Resistive microbolometers employing high fill factor designs	20

1.4.3	Fill Factor Improving Designs on Other Uncooled FPAs	22
1.5.	Research Objectives and Thesis Organization	24
2.	PIXEL LEVEL UMBRELLA STRUCTURE DESIGN	27
2.1.	Mechanical Properties of Silicon Dioxide and Silicon Nitride	28
2.1.1.	Mechanical Properties of PECVD Silicon Dioxide (SiO ₂)	28
2.1.2.	Mechanical Properties PECVD Silicon Nitride (SiN).....	30
2.2.	Optical Properties of Silicon Dioxide and Silicon Nitride	32
2.2.1.	IR-VASE measurements and Characterizations.....	33
2.2.2.	FDTD Simulations of basic 2D umbrella slab.....	40
2.2.3.	3D FDTD Simulations of low-cost Pixel Geometries	53
2.3.	Transient Thermal Simulations	61
2.3.1.	Thickness simulations.....	63
2.3.2.	Anchor variation simulations.....	66
3.	FABRICATION OF UMBRELLA STRUCTURES.....	69
3.1.	Dummy fabrication with amorphous-Silicon (a-Si) sacrificial layer	70
3.2.	Die level CMOS with a-Si sacrificial layer	79
3.3.	Dummy fabrication with PI layer	81
3.4.	CMOS fabrication with PI sacrificial layer	83
3.5.	Umbrella structure integration onto 70- μ m pitched pixels.....	87
3.6.	Umbrella structure integration onto 50- μ m pitched pixels.....	91
4.	PERFORMANCE EVALUATION TESTS	95
4.1.	Measured FTIR Results	95
4.2.	Responsivity Tests	98
5.	CONCLUSION AND FUTURE WORK.....	105
	REFERENCES.....	113

LIST OF FIGURES

FIGURES

Figure 1.1: Atmospheric transmission plot of the infrared radiation. Note that there is almost no transmission in the 5-8 μm range due to absorption of water molecules, hence this region is not utilized [17].	2
Figure 1.2: Schematic representation of a typical thermoelectric detector. The temperature difference between the cold junction (T_c) and the hot junction (T_h) induces a voltage (V_{ind}) due to different Seebeck coefficients of Material-1 and Material-2 [22].....	3
Figure 1.3: Schematic representation of a typical pyroelectric sensor.....	4
Figure 1.4: Schematic view of a typical microbolometer consisting of micro bridge structure that is connected to substrate and the readout circuit through metal connecting lines [22].	5
Figure 1.5: Simplified thermal equivalent circuit diagram of the microbolometer.....	9
Figure 1.6: Thermal image of a soldering iron obtained with the 64 x 64 SOI-CMOS low-cost microbolometer FPA [58].....	12
Figure 1.7: Thermal images obtained using the 128 x 128 array of SOI-CMOS microbolometer FPA. The NETD of the FPA is reported to be 1.1 K with F/1 optics [46]	13
Figure 1.8: Thermal image obtained by the 160 x 120 SOI-CMOS microbolometer array with pixels of 70 μm pitch. The reported NETD value is 350 mK with optics of F/1.....	13
Figure 1.9: Thermal image obtained using the first generation 160 x 120 SOI-CMOS low-cost microbolometer FPA as a result of two revisions. The reported peak NETD is 280 mK with the optics of F/1 [48].....	14
Figure 1.10: Schematic representation of a unit low-cost pixel (a) without any additional structures, (b) with additional structure that increases the fill factor.	16

Figure 1.11: Cross-sectional schematic view of the SOI diode uncooled microbolometer pixel with high fill factor (90 %) achieved using umbrella structure that spans the pixel [53].	17
Figure 1.12: Cross-sectional schematic view of the SOI diode uncooled microbolometer pixel with high fill factor (90 %) achieved using umbrella structure that spans the pixel with reflector on the pixel body and the arms [53].	17
Figure 1.13: Cross-sectional schematic view of the SOI diode uncooled microbolometer pixel with improved reflector structure that is tailored for smaller pixels to obtain high fill factor (90 %) achieved using umbrella structure that spans the pixel with reflector on the pixel body and the arms [53].	18
Figure 1.14: SEM images of three-level SOI diode uncooled pixel structure with a pitch of 28 μm (a) top view and (b) side view [53].	18
Figure 1.15: SEM image of the SOI diode 15 μm pitch pixels including absorber umbrella structures developed by [62].	19
Figure 1.16: SEM image of the fabricated uncooled SOI-diode FPA with the umbrella design [64].	20
Figure 1.17: SEM image of one-level VO _x microbolometer designed with absorbing umbrella structures to increase the fill factor [65].	20
Figure 1.18: SEM image of the pixels with 23.5 μm pitch having an absorbing high fill factor structure that extends through each pixel [68].	21
Figure 1.19: Uncooled thermoelectric sensor including an umbrella structure to increase the fill factor, where (a) schematic representation and (b) SEM image of the completed device is provided [69].	22
Figure 1.20: Schematic view of the thermoelectric bolometer employing a two-level structure that expands through the unit cell [71].	23
Figure 1.21: Schematic diagram of the thermoelectric detector structure involving an umbrella absorber to produce high fill factor [14].	24
Figure 2.1: 3D FEM simulation results, exaggerated for visual convenience, displayed with absolute value of the maximum surface displacement. Note that the stress gradient applied bends down the umbrella layer with a maximum of 30% strain in the growth direction, which is a significant deflection for this geometry.	29

Figure 2.2: 3D FEM simulation results –exaggerated for visual convenience– displayed with absolute value of the maximum surface displacement in z-direction. Note that the stress gradient applied bends up the umbrella layer with a maximum of 7.5% strain in the growth direction, which is relatively low compared to the SiO₂ material umbrella structure. 31

Figure 2.3: Maximum displacement of the simulated square umbrella structures (800nm thick and 48μm wide with 5μm anchor in the center) under varying stress gradient values. Under increasing stress gradient, SiO₂ evidently produces more deflection, which is an undesired effect. 32

Figure 2.4: Schematic representation of ellipsometric measurement. Linearly s- and p- polarized light is reflected from the sample surface at varied incident angles (Φ_0) producing phase difference (Δ) and different amplitude ratios (ψ) picked up by the detector. The interaction of the light determines the material characteristics in the infrared region [82]. 33

Figure 2.5: Schematic view of the dielectric deposited wafers for IR-VASE measurement. Note that the gold layer underneath the dielectric layers is thick enough to be optically opaque, hence no light interaction occurs with silicon substrates. Dashed arrows represent polarized the infrared radiation. 34

Figure 2.6: Fitted spectral ψ and Δ data of SiO₂ film deposited on gold using PECVD. Note the abrupt change in both plots implying a strong oscillator around 8.5μm wavelength. 35

Figure 2.7: Fitted spectral ψ and Δ data of Si₃N₄ film deposited on gold using PECVD. Note the change in both plots implying a broader oscillator around 9μm wavelength. 36

Figure 2.8: Optical constants (refractive index and extinction coefficient) of (a) PECVD SiO₂ and (b) PECVD SiN deposited using two separate tools –solid lines correspond to one tool while the dashed lines correspond to the material deposited using another tool as noted with a number in parenthesis. Note that the optical characteristics of each material is similar regarding the difference in the tool they are deposited in. 38

Figure 2.9: Extinction coefficient of SiO₂ and SiN overlaid. Note that the absorbing wavelength regions are complementary for both materials; meaning while SiO₂

absorbs relatively lower wavelengths of the LWIR window, SiN absorbs in the longer wavelength region.	39
Figure 2.10: Comparison of the FDTD absorption simulation results (colored and marked) and the FTIR measurements (lines) of the SiO ₂ film (dashed lines) and SiN film (solid lines). The films are coated on optically opaque gold with thickness values of 600 nm and 620 nm for SiO ₂ and SiN respectively.	41
Figure 2.11: Schematic representation of the FDTD simulation setup for the varying air gap size of umbrella layer (SiN and SiO ₂) on the SiO ₂ low-cost pixel surface. Incident plane wave (red arrow) is placed normal to the surface while the reflection and transmission data monitors (blue lines) are spanned through the unit cell above the light source and underneath the structure respectively.	42
Figure 2.12: 2D FDTD simulation results when both the bottom and the umbrella layers are selected to be SiO ₂ . The simulated (a) reflection, (b) transmission, (c) absorption, and (d) the average of all three in the LWIR window is calculated and plotted.	44
Figure 2.13: 2D FDTD simulation results when the bottom layer is SiO ₂ and the umbrella layer is selected to be SiN. The simulated (a) reflection, (b) transmission, (c) absorption, and (d) the average of all three in the LWIR window is calculated and plotted. Note that there is a maximum point in the average absorption when the air gap is around 2.5 μm.	46
Figure 2.14: 2D FDTD simulation results when the bottom SiO ₂ thickness is 2 μm and the umbrella layer is selected to be SiN. The simulated (a) reflection, (b) transmission, (c) absorption, and (d) the average of all three in the LWIR window is calculated and plotted.	48
Figure 2.15: 2D FDTD simulation results when the bottom SiO ₂ thickness is 3 μm and the umbrella layer is selected to be SiN. The simulated (a) reflection, (b) transmission, (c) absorption, and (d) the average of all three in the LWIR window is calculated and plotted.	49
Figure 2.16: 2D FDTD simulation results when the bottom SiO ₂ thickness is 4 μm and the umbrella layer is selected to be SiN. The simulated (a) reflection, (b) transmission, (c) absorption, and (d) the average of all three in the LWIR window is calculated and plotted.	50

Figure 2.17: Average absorption, transmission, and reflection plots calculated in LWIR window of SiN umbrella layer with 1 μm bottom SiO ₂ layer (color-filled markers with solid lines) compared with the averages calculated in LWIR window of SiN umbrella layer with 3 μm bottom SiO ₂ layer (white-filled markers with dashed lines).	51
Figure 2.18: Schematic view of the 2D FDTD simulation run with varying gap between the bottom slab and the umbrella, as well as varying umbrella thickness. Note that the bottom boundary condition is chosen to be metal, meaning that it will reflect the incoming radiation at the boundary fully, regardless of the wavelength.....	52
Figure 2.19: 2D FDTD simulation results of varying gap and thickness of the SiN umbrella layer on top of 2 μm SiO ₂ pixel layer.	53
Figure 2.20: 3D model of low cost pixels (a) 70- μm pixel perspective view, (b) 50- μm pixel perspective view. Cross-sectional views of the (c) 70- μm pixel and (d) 50- μm are presented along with denoted dimension information.	54
Figure 2.21: Snapshot of the 50- μm low-cost pixel 3D model that is used in the FDTD solver software where in (a) the inverted pyramid effect of the TMAH etching is not accounted for while in (b) the inverted pyramid surface is added. Only the oxide layers and Metal-1 layer is modeled for both simulations.	55
Figure 2.22: Optical response comparison of the 50- μm low-cost pixel. Note that the solid lines represent the added inverted pyramid surface as shown in Figure 2.21 (b) while the dashed lines represent the simulation results correspond the results obtained without the inverted pyramid effect as seen in Figure 2.21 (a).	55
Figure 2.23: Snapshot of the simulated 50- μm low-cost pixel including the umbrella structure that spans 48 μm throughout the unit cell; standing on the pixel with 4 square posts with 5 μm square openings.....	56
Figure 2.24: Simulated absorption, reflection, and transmission plots of the 50- μm low-cost pixel with various umbrella structure having thickness values of (a) 200 nm, (b) 400 nm, (c) 600 nm, and (d) 800 nm. The dashed lines on each plot is the simulated spectra of the same pixel geometry with no umbrella structure integrated.	57
Figure 2.25: Computed average optical response of the 50- μm low-cost pixel with and without umbrella structures while varying the umbrella layer thickness in the LWIR window.	57

Figure 2.26: Simulated absorption, reflection, and transmission plots of the 50- μm low-cost pixel having only the pixel body with various umbrella thickness values of (a) 200 nm, (b) 400 nm, (c) 600 nm, and (d) 800 nm. The dashed lines on each plot is the simulated spectra of the same pixel geometry with no umbrella structure integrated. 59

Figure 2.27: Computed average optical response of the 50- μm low-cost pixel consisting of only the pixel body (34 μm x 34 μm) with and without umbrella structures while varying the umbrella layer thickness in the LWIR window. 60

Figure 2.28: Computed average optical response of the 50- μm low-cost pixel with varying the 0.4- μm thick umbrella post size that is shaped square. 0 μm width means there is no umbrella structure at all. Note the decrease in absorption as the post width comprises 78 % of the pixel body. 60

Figure 2.29: Snapshot of the CoventorWare FEM modeling of the (a) 70- μm pixel and (b) 50- μm pixel. Note that the active region silicon layers (light blue) and poly-silicon interconnects (light green) that are embedded in the pixel body are modeled as well. 62

Figure 2.30: Snapshot of the temperature distribution of 50 μm low-cost pixel comprising 4 square posts to support a 600-nm thick SiN umbrella structure. 63

Figure 2.31: Computed transient thermal response of the 70- μm pixel with and without the umbrella structure. It is evident that the addition of umbrella structure with varying thickness values do not change the transient response substantially. 64

Figure 2.32: Computed transient thermal response of the 50- μm pixel with and without the umbrella structure. It is evident that the addition of umbrella structure with varying thickness values do not change the transient response substantially. 65

Figure 2.33: GDS model schematic of the 70- μm low-cost pixel and the umbrella structure with varying post numbers. Note that the period (p) of the pixel is 70- μm while the umbrella spans (f) 68 μm standing on a post size (a) of 5 μm 67

Figure 2.34: Thermal simulation results of the 600 nm thick umbrella structure integrated to the 70- μm low-cost pixel with various post numbers connecting the umbrella to the pixel body. It should be noted that the results of each simulation are almost identical. 67

Figure 2.35: Thermal simulation results of the 600 nm thick umbrella structure integrated to the 70- μm low-cost pixel with various post numbers connecting the umbrella to the pixel body. It should be noted that the results of each simulation are almost identical..... 68

Figure 3.1: Schematic representation of the 2D pattern of low-cost pixel geometry. The period of the pixel is denoted as p while the body width is b . The arm width is w_a and the spacing between the body-arm-frame geometry is w_s , which is also symmetric. 70

Figure 3.2: Schematic view of the full unit cell as well as the cross-section of the dummy structure fabrication on bare silicon wafer. 72

Figure 3.3: Schematic view of the full unit cell as well as the cross-section of the dummy structure fabrication on bare silicon wafer. (continued) 73

Figure 3.4: SEM images of (a) 50- μm dummy pixel and (b) 70- μm dummy pixel etched in DRIE in one step to form the arm grooves. 75

Figure 3.5: SEM image of a 70- μm dummy pixel after the release process. Note, however, that the sacrificial layer underneath pixel body region is not etched since umbrella layer covers the side walls of the arm trenches due to not being able to seal the arm spacing properly. 76

Figure 3.6: SEM image of a 50- μm dummy pixel before release process. Note that the umbrella layer continuously spans above the arm spacing not getting into the trenches. Moreover, the umbrella frames are formed and etched separating each one with a distance of 2.5 μm for this particular dummy structure. 77

Figure 3.7: SEM images of dummy pixels integrated with 600-nm thick silicon nitride layer umbrella. There are various post size and numbers employed in (a) post diameter is 5 μm with of circular posts, (b) post diameter is 3 μm on four circular posts, and in (c) post size is 30 μm which is a single square resting on the pixel body. 79

Figure 3.8: SEM image of the cross-section of the 70 μm low-cost pixel after depositing 3 μm thick a-Si as the sacrificial layer in the most non-conformal method using PECVD. There is a wide opening atop the arm that prevents proper umbrella material deposition as the succeeding step. 80

Figure 3.9: SEM image of the cross-section of the 50 μm low-cost pixel after depositing 6 μm thick a-Si as the sacrificial layer in the most non-conformal method

using PECVD. The complete sealing of the arm spacing is only possible after 6 μm a-Si deposition, which is not a realistic air gap height for the considered umbrella geometry..... 81

Figure 3.10: SEM images of modified (a) 50- μm dummy pixel and (b) 70- μm dummy pixel. Even though there is a slight alignment problem of the second etching patten, the arm height is reduced to realistic levels relative to the pixel frame and the body. 82

Figure 3.11: SEM image of the cross-section of 70- μm dummy pixel after top layer of the cured PI 2556 is removed. Note that the arm spacing is completely filled with the polymer acting as desired..... 83

Figure 3.12: Schematic process flow of the low-cost pixel umbrella integration on a 70 μm pitch pixel with single square post..... 85

Figure 3.13: Schematic process flow of the low-cost pixel umbrella integration on a 70 μm pitch pixel with single square post. (continued) 86

Figure 3.14: SEM image of the 70- μm pitched low-cost pixel before coating sacrificial layer..... 87

Figure 3.15: SEM image of the 70- μm pitched low-cost pixels after etching the anchor openings on the sacrificial layer. Note that there are four posts on each pixel body and the arm topology is still visible. 88

Figure 3.16: SEM image of the cross-section of a 70- μm pitched low-cost detector array with integrated umbrella structures. Note that the sacrificial layer is not completely removed around the posts. Also, the pixel is not completely released since it is connected to the substrate although anisotropic etching has started below the arms. 89

Figure 3.17: SEM images of the completed umbrella structures on low-cost pixels with 70 μm pitch. Note that in (b) some umbrella structures are detached from the post where it connects due to thinning during TMAH etching, while some are stuck to the surface while drying due to stiction problem..... 90

Figure 3.18: SEM image of the low-cost pixel with 50 μm pitch after being fully released in TMAH. Note that this particular design includes 9 circular posts that connect the umbrella to the pixel body. 92

Figure 3.19: Schematic representation of the placement of different umbrella designs with a row of 30 on the low-cost FPA with a size of 160x120 pixels..... 93

Figure 3.20: SEM image of the low-cost pixel with 50 μm pitch after being fully released in TMAH, where inverted pyramid geometry can be seen as the result of anisotropic wet etching. Also, the FPA is designed to have umbrella structures (with perforations) and pixels having no umbrella for a fair comparison. 93

Figure 4.1: Measured FTIR response of the low-cost detector with 70 μm pitch in array format. Pixels with umbrella structure and without umbrella structure are compared. It should be noted that different umbrella designs yield almost identical results in optical domain..... 96

Figure 4.2: Measured FTIR response of the low-cost detector with 50 μm pitch in array format, measured on the same die. Pixels with umbrella structure and without umbrella structure are compared. It should be noted that different umbrella designs yield almost identical results in optical domain. 97

Figure 4.3: Measured (a) input referred responsivity and (b) NETD of the 160 x 120 array of FPA with 70 μm pitch pixels. The peak responsivity occurs at 70 $\mu\text{V} / 10^\circ\text{C}$ resulting a peak NETD of 1.16 K. 99

Figure 4.4: Measured (a) input referred responsivity and (b) NETD of the 160 x 120 array of FPA with 70 μm pitch pixels with umbrella structures integrated that are 600 nm thick comprising 4 posts with a size of 5 μm . The peak responsivity occurs at 100 $\mu\text{V} / 10^\circ\text{C}$ resulting a peak NETD of 774 mK. 100

Figure 4.5: Responsivity map of the low-cost detector with 50 μm pixel pitch. Note that that the top 30 rows of the FPA has darker color, indicating that the responsivity of this region is lower than the rest of the FPA. Moreover, within the different umbrella structures, there seems no visible distinct responsivity result..... 101

Figure 4.6: Input referred responsivity histogram of the tested low-cost detector with 50 μm pitch. There are two main distributions due to having regions with and without umbrella. The lower responsivity region, making up one quarter of the FPA, has lower number of distribution as well as average responsivity that is 30 % lower. 102

Figure 4.7: NETD histogram of the low-cost pixel with 50 μm pitch with average NETD of 278 mK while the peak NETD is 260 mK. Note that the distribution of pixels

generate a tail that broadens the peak towards larger NETD values due to the region with no umbrella integrated. 103

Figure 4.8: Input referred responsivity histogram of the tested low-cost detector with 50 μm pitch under different bias conditions. Two main distributions are observed regardless of the biasing condition, which implies the fill factor contribution to the responsivity. 104

Figure 5.1: Measured FTIR spectra of Au/SiN/NiCr stack where the thickness of the NiCr layer is varied. Note that addition of NiCr increases the absorption significantly. 108

Figure 5.2: Comparison of the computed absorption using CTL and measured absorption spectrum of 620 nm of silicon nitride on gold substrate with and without NiCr coating. 109

Figure 5.3: Measured FTIR spectra of Au/SiN/NiCr stack before and after being exposed to TMAH release procedure as well as 10 min of oxygen plasma. 110

LIST OF TABLES

TABLES

Table 2.1: Extracted time constant data of 70- μm and 50- μm low-cost pixels while including umbrella structures of different thicknesses compared with pixels including no umbrella structure.....	66
Table 3.1: Lateral dimension information provided for the low-cost pixel geometries. These dimensions are used to define the structures in the FEM modeling as well as the lithography of the real structures.....	71

CHAPTER 1

INTRODUCTION

Infrared radiation has been known since 1800s when W. Herschel demonstrated the temperature of each color and beyond the visible spectrum, labeled as “infra-red” [1]. Following this discovery, enormous studies have been executed in the next hundred years to conceive and to “see” the infrared radiation. As stated by the modern physics, all objects having temperature above 0 K, emit electromagnetic radiation. The endeavor to see the temperature ranges that correspond to mid-infrared regime has been crucial since the region of interest covers temperature of everyday objects as well as the molecular vibrational and rotational resonances for commonly studied compounds. This results in myriad of application areas for the developing infrared detector domain. Imaging in infrared can be used in medical imaging [2-4], civil and military defense [2, 5-7], food and agriculture industry [8], construction [9], fire-detection [10-12], and space applications [11, 13, 14] among many that are not mentioned here.

Depending on the specific application and the atmospheric transmission, there are four major spectral windows that incorporate infrared imaging, and they are labeled as short-wave infrared (SWIR) for 1-3 μm , mid-wave infrared (MWIR) for 3-5 μm , long-wave infrared (LWIR) for 8-14, and far-infrared (FIR) for wavelengths greater than 16 μm [15, 16]. Most of the applications that target human detection, whether commercial or military, optimize device parameters to work in the LWIR range, and more specifically in the 8-12 μm wavelength range since the temperature range of interest has maximum spectral exitance around 10 μm wavelength. The 8-12 μm range will be referred as LWIR window henceforth. The range of this window as well as

the range of aforementioned spectral windows are limited with the atmospheric transmission as shown in Figure 1.1.

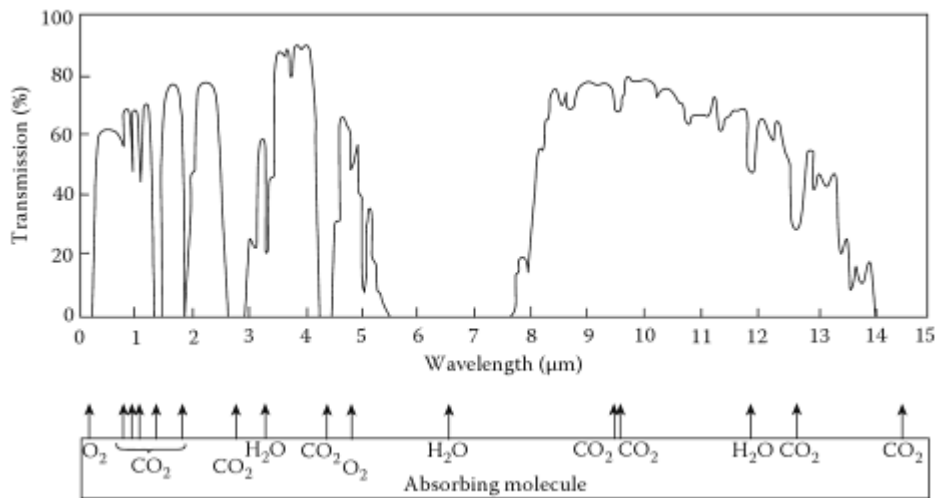


Figure 1.1: Atmospheric transmission plot of the infrared radiation. Note that there is almost no transmission in the 5-8 μm range due to absorption of water molecules, hence this region is not utilized [17].

1.1 Infrared Detector Types

There are two major infrared detector classes; one is based on photon detection while the other is based on thermal detection [18, 19]. Photon detectors respond to the incoming photons at infrared wavelengths by generating electrical current within the material due to generated electron-hole pairs [11, 13, 17, 19]. However, the interaction of photons with electrons is difficult to distinguish from the thermally generated electrons at room temperature, thus the photon sensing material needs to be cooled down to cryogenic temperatures [1, 17-20]. The cooling requirement increases the cost of the system and its maintenance, not to mention decreased mobility due to increased size with the addition of cooling system [21, 22].

The second type of detection mechanism is based on thermal detection, which has a sensing material that absorbs the infrared radiation and produces heat in response. These systems do not require cryogenic cooling systems, hence referred as “uncooled” systems. Although uncooled detectors usually have slower response time, and lower

performance compared to the cooled detectors, their low-cost implementation has made them worth studying. The sensing structure is thermally isolated from the surrounding through supporting structures in order to enable the temperature difference sensing relative to the surrounding temperature. There are different transducing mechanisms of the absorbed infrared energy into various physical properties of the materials used in the sensors. The differentiation in transducing systems generates distinct classes of uncooled imagers, of which most commonly used ones are: thermoelectric detectors, pyroelectric detectors, and microbolometers [1]. Next subsection elaborates on each of these technologies.

1.1.1 Thermoelectric Detectors

Thermoelectric effect is used to detect infrared based on different *Seebeck coefficients* of materials used in physical junction [11, 13, 14, 19]. Figure 1.2 depicts the schematic view of a typical thermoelectric detector. Seebeck coefficient is the measure of a material's potential to induce a voltage when subjected to temperature difference across that material. When a junction (hot junction: T_h) is exposed to infrared radiation while the other junction (cold junction; T_c) is at a fixed temperature heat sink, there exists a voltage induced at the cold junction due to different Seebeck coefficients that each material incorporates.

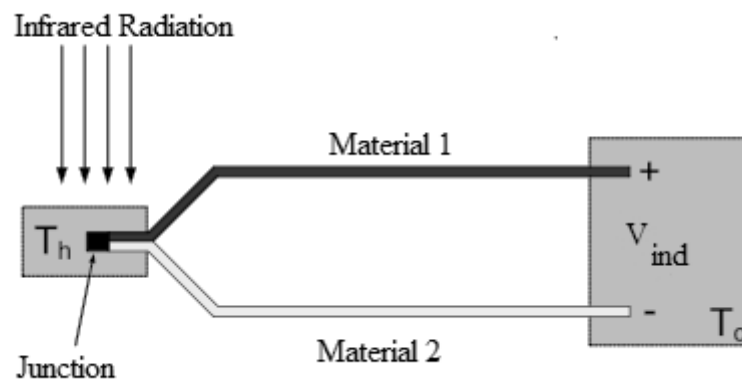


Figure 1.2: Schematic representation of a typical thermoelectric detector. The temperature difference between the cold junction (T_c) and the hot junction (T_h) induces a voltage (V_{ind}) due to different Seebeck coefficients of Material-1 and Material-2 [22].

The advantage of thermoelectric detectors is that they can operate under no bias condition, which implies the elimination of self-heating problem and enables very low power systems. Although there are numerous advantages in terms materials and fabrication cost, the application areas for the thermoelectric detectors are mostly in low-end fields since the responsivity of these detectors are substantially low compared to other uncooled technologies, and the implementation of arrays of thermoelectric detectors (thermopiles) require very large area [14, 19].

1.1.2 Pyroelectric Detectors

Pyroelectric effect can be observed in materials that respond to sudden temperature change in spontaneous electric polarization [18, 19, 22]. The electric polarization can be measured as voltage across the material. At constant temperature, the polarization is neutralized by the mobile charges at a finite time constant. Therefore, the pyroelectric effect can be utilized in modulated signals only.

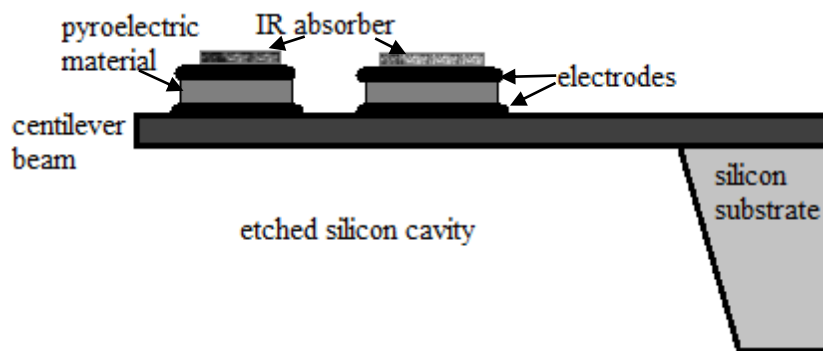


Figure 1.3: Schematic representation of a typical pyroelectric sensor.

Although pyroelectric detectors do not require biasing voltage and can be realized in array format, the need for input radiation modulation and the low responsivity limit its application areas. There are number of examples demonstrating arrays of detectors [23, 24] , however, the use of ferroelectric materials as the active material precludes CMOS compatibility. Moreover, the requirement of modulation and poor performance under mechanical vibration bring substantial disadvantage to employ pyroelectric technology in imaging systems.

1.1.3 Microbolometers

Although etymologically “bolometer” refers to sensors that induce temperature rise when exposed to electromagnetic radiation regardless of their temperature sensing mechanism, “infrared microbolometer” commonly refers to sensing mechanism that changes its electrical conductivity [18], which implies that the sensing material can be a resistor or a diode [16]. The first thin-film resistive microbolometer was proposed in 1982 [25], and enormous amount of studies have been published regarding the development of microbolometers in various aspects since then.

Figure 1.4 shows a typical microbolometer pixel consisting of a suspended microbridge structure that is connected to the substrate via thermal isolation arms and thin-film temperature sensitive element coated on top. Notice that the suspended bridge is elevated from the substrate surface in order to realize a cavity resonance, and underneath the pixel, there is usually a reflector layer to optimize absorption of the pixel.

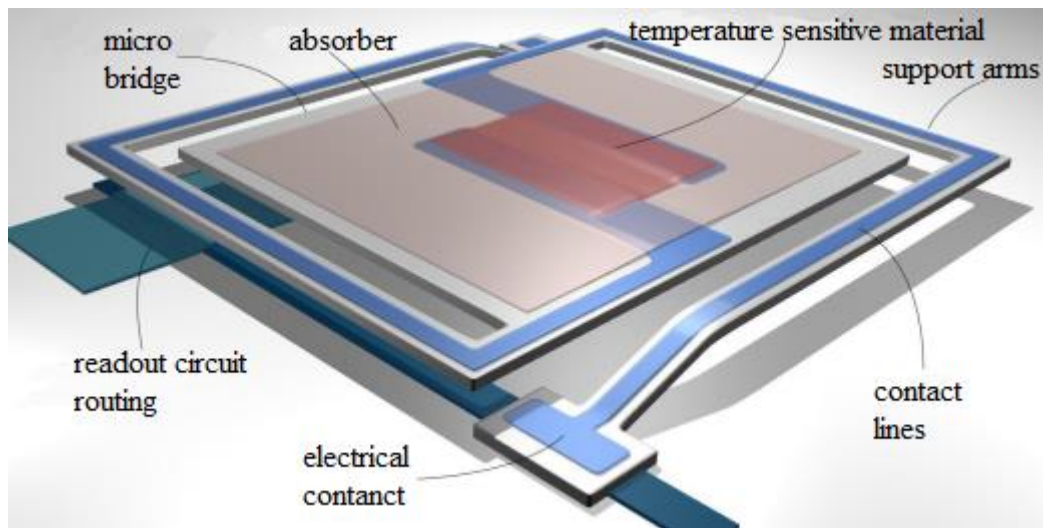


Figure 1.4: Schematic view of a typical microbolometer consisting of micro bridge structure that is connected to substrate and the readout circuit through metal connecting lines [22].

Microbolometer pixels are generally arranged in two-dimensional arrays in order to form focal plane arrays (FPA) for imaging purposes. The early thin-film

microbolometer arrays in the early 1880s were constructed using metal films due to being easily fabricated [26]. However, materials having superior temperature sensitivity were investigated and vanadium oxide (VO_x) films dominated the microbolometer industry being the most commonly used active material in uncooled microbolometers, even today [1]. There are other resistive elements common with comparable temperature coefficient of resistance (TCR) values such as 3 %/K. The most common films that are used as the temperature sensitive elements are amorphous silicon (a-Si) [27, 28], polycrystalline silicon germanium (poly SiGe) [29-32], and yttrium barium copper oxide (YBaCuO or YBCO) [22, 33-35].

Compared to the photonic detectors, microbolometers have not been exploited in the same scale until recently mainly because microbolometers are relatively slow and attain less infrared sensitivity. Nonetheless, recent developments in the microbolometer FPA discourse had paved the way for high performance microbolometers with noise equivalent temperature difference (NETD) values below 25 mK with an F-number of the optics of $F/\# = 1$ [36-42].

As a result of the promising developments in the uncooled imagers, various application areas and markets have been emerged [43]. In return, these markets have promoted further performance enhancement and cost reduction. A popular approach to low-cost detector fabrication is constructing the temperature sensitive element using silicon diodes [44-50]. Silicon diode elements enable the use of standard CMOS technologies to fabricate uncooled microbolometer FPAs that reduces the cost of production significantly [16, 44, 45, 51]. In addition, ability to reduce pixel pitch in CMOS line, combined with the advanced wafer level vacuum packaging (WLVP) technology developed by MEMS industry, the market for low-cost infrared imagers in the LWIR window has evolved immensely [43, 52]. This study focuses on the low-cost detector scene, in the context of uncooled infrared FPAs that target commercial application requirements.

1.2 Performance Parameters of Uncooled Microbolometers

This section explains, in detail, the performance parameters of an uncooled microbolometer that defines the overall quality of an FPA. Geometrical design of microbolometers are centered around four important parameters in order to realize high performance. First important parameter is the high absorption in the region of interest, since the signal generated by the detector is directly linked with the amount of infrared power it absorbs. The second parameter is the high temperature sensitivity of the active material with low 1/f noise characteristics since it is the first place where the temperature difference is transduced into an electrical signal that can be measured. This parameter brings along the necessity for low thermal conductance of the infrared sensing body from the heat sink in order to realize significant temperature rise due to absorbed infrared power. Finally, a sufficiently low thermal time constant to integrate adequate electrical signal without compromising the frame rate of the imaging system.

These properties are categorized under three subsections labeled as “temperature sensitivity” that expands the temperature rise in response to infrared power absorbed by the pixel; while “responsivity” explains the electrical signal produced by the temperature change. Finally, as the most important figure of merit, NETD is introduced that incorporates system level overall performance of the imaging system.

1.2.1 Temperature Sensitivity

When silicon diode is forward biased, the voltage drop across the terminals has a finite temperature sensitivity [49, 53]. This property is analytically expressed as seen in Equation 1.1 , where n_i is the ideality factor, T is the temperature, k is the Boltzmann constant, q is the electron charge, I_D is the bias current, and I_S is the reverse saturation current of the diode [53].

$$V_F = n_i \frac{kT}{q} \ln \left(\frac{I_D}{I_S} \right) \quad (1.1)$$

Temperature dependency of I_S is expressed in Equation 1.2, where K and m are temperature independent constants [54].

$$I_S = KT^m e^{\frac{-E_g}{kT}} \quad (1.2)$$

When the expression in Equation 1.2 is substituted into Equation 1.1 to fully express the temperature dependency of the forward bias voltage of a diode, and derived with respect to temperature, T , the simplified expression is written in Equation 1.3.

$$\frac{dV_F}{dT} = \frac{k}{q} \ln\left(\frac{I_D}{I_S}\right) - m \frac{kT}{qT} - \frac{E_g}{qT} = -\frac{m \frac{kT}{qT} + \frac{E_g}{qT} - V_F}{T} \quad (1.3)$$

Equation 1.3, that signifies the temperature sensitivity of the forward bias voltage (V_F), also referred as TC_D , can be simplified by inserting 25 mV for kT/q at room temperature, and by inserting 1.12 V for E_g/q as an acceptable value for the band gap of silicon. The resulting expression is displayed in Equation 1.4, where m is a temperature independent constant that is usually between 2.5 and 5.

$$\frac{dV_F}{dT} \equiv TC_D = -\frac{0.025m + 1.12 - V_F}{T} \quad (1.4)$$

It is evident that there is not much room to alter the temperature sensitivity of a silicon diode, however, serially connected multiple diodes multiply the expression in Equation 1.4 linearly. Therefore, an important parameter is to place as many diodes in a given pixel pitch as possible to increase the sensitivity. On the other hand, the pixel pitch should be as low as possible to allow low-cost production and higher spatial resolution.

1.2.2 Responsivity

Responsivity (\mathfrak{R}) defines the ratio of the output signal produced to the incident infrared power. The electrical output signal may either be voltage or current depending on the readout electronics, in which case the ratio has units of Volts/Watt (V/W) or Amps/Watt (A/W). As an analytical approach to responsivity in terms of infrared light

and detector properties, a simplified thermal circuit model is introduced in Figure 1.5, where the thermal conductance of the support arms are modeled as G_{th} and the thermal mass of the detector is modeled as C_{th} . The infrared power modeled as ηP_o , where η is the optical absorption coefficient, and modulated with a frequency of ω , generates temperature difference on the microbolometer body that is shown as ΔT .

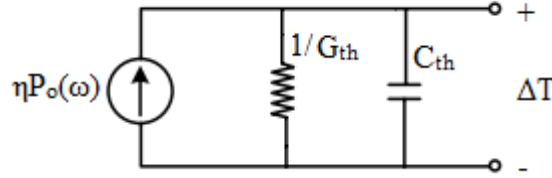


Figure 1.5: Simplified thermal equivalent circuit diagram of the microbolometer

The currents through the thermal paths equal the current provided by the source in analogy to the heat flow. Therefore, the heat flow equation is expressed as shown in Equation 1.5 below [26]. In this simplified model, Joule heating effect of the active element is not taken into account and the equation provided is for a pulsed input, not a steady state equation.

$$C_{th} \frac{d\Delta T}{dt} + G_{th} \Delta T = \eta \beta P_o e^{j\omega t} \quad (1.4)$$

The infrared source model includes a factor β that is called the “fill factor” signifying what fraction of the incoming infrared radiation is actually incident upon the temperature sensitive body on the repeating unit cell. Solution to this first order equation is expressed in Equation 1.5, and solved for the absolute value of the temperature difference, $|\Delta T|$.

$$|\Delta T| = \frac{\eta \beta P_o}{G_{th} \sqrt{1 + \left(\omega \frac{C_{th}}{G_{th}}\right)^2}} \quad (1.5)$$

In Equation 1.5, C_{th}/G_{th} term can be summarized into τ , which is known as the *time constant* of the detector. Time constant of the detector limits the operation speed of a microbolometer. Expression of the generated signal output can easily be obtained as provided in Equation 1.6.

$$\Delta V_{out} = |\Delta T| TC_D \quad (1.6)$$

Then dividing the expression by the infrared power supplied P_o , gives the responsivity result in AC domain. Equation 1.7 provides the final expression of the responsivity of a microbolometer.

$$\frac{\Delta V_{out}}{P_o} \equiv \mathfrak{R} = \frac{\eta \beta TC_D}{G_{th} \sqrt{1 + (\omega\tau)^2}} \quad (1.7)$$

It is indisputable that the responsivity is inversely proportional to the thermal conductance of the sensor that is as the thermal isolation gets better, greater responsivity is obtained for unit infrared power absorbed.

1.2.3 Noise Equivalent Temperature Difference (NETD)

Noise equivalent temperature difference (NETD) is the most commonly used figure of merit to evaluate the performance of infrared detectors as it incorporates a system level approach including infrared optics and the electronics. It physically defines the smallest temperature change that is distinguishable from the overall noise of the system. Analytically, NETD can be expressed as seen in Equation 1.8 [18],

$$NETD = \frac{4 F^2 V_N}{\tau_o A_D \mathfrak{R} (\Delta P/\Delta T)_{\lambda_1-\lambda_2}} \quad (1.8)$$

where V_N is the total voltage noise of the system, τ_o is the normalized transmission of the optics in the region of interest denoted by $\lambda_1 - \lambda_2$, A_D is the detector area, \mathfrak{R} is the

voltage responsivity of the sensor, and $(\Delta P/\Delta T)_{\lambda_1-\lambda_2}$ is a constant in the noted wavelength range of $\lambda_1 - \lambda_2$, which signifies the change of power with per unit area radiated by a blackbody at a temperature T . The term labeled as, F , is related with the infrared optics that can be expanded into an expression in terms of F-number ($F/\#$) of the optics, which is the ratio of the focal length to the diameter of the infrared lens (f/D):

$$4 F^2 = 4(f/D)^2 + 1 = 4(F/\#)^2 + 1 \quad (1.9)$$

For a lens with $F/\#$ of 1, the $4 F^2$ expression equals to 5. It is apparent that low F-number of the optics yield lower NETD results since more light is collected from the scene compared to a high F-number lens.

The significance of \mathfrak{R} also appears in direct relation to NETD. Therefore, for a detector geometry where fill factor, β is close to unity, and high responsivity, the incoming infrared potential is utilized more efficiently yielding a lower NETD for identical systems in consideration.

1.3 Low-cost Infrared Detectors Developed at METU MEMS

There has been tremendous research on low-cost microbolometers in the last decade globally, and the early FPA design and development at METU-MEMS had started in 1997 [46]. The first realized detector arrays utilize standard CMOS n-well resistors as the temperature sensitive element due to rather high TCR compared to other materials available in the CMOS line fabrication [51, 55, 56]. The fabricated 16 x 16 array of infrared detectors have a fill factor of 13 % with a pixel pitch of 80 μm . However, due to large pixel pitch, low performance, and low temperature sensitivity, a new approach is followed altering the temperature sensitive element to p + -active/n-well diodes. Three distinct designs were realized with arrays sizes of 128 x 128, 64 x 64, and 16 x 16 using a 0.35 μm standard CMOS line for the first two arrays, and 0.8 μm CMOS technology for the 16 x 16 array [44, 57, 58]. Among these detector arrays, the latter

one with array size of 16 x16 was successfully used to obtain infrared images. The pixel pitch of this detector was 60 μm with an improved fill factor of 34.8 %.

In order to ease the requirements for the post-CMOS processes, later generation arrays are designed using a different CMOS line (X-FAB 1.0 μm SOI-CMOS) while this process also allows smaller diode sizes due to the nature of standard SOI-CMOS methodology [46]. Detector FPA with an array size of 64 x 64 incorporating pixels with a pitch of 70 μm and a fill factor of 32.65 %. Successful fabrication of these detectors enabled obtaining thermal images as shown in Figure 1.6.



Figure 1.6: Thermal image of a soldering iron obtained with the 64 x 64 SOI-CMOS low-cost microbolometer FPA [58]

Using the same SOI-CMOS process, an attempt to increase the fill factor has been executed by introducing “umbrella” in the CMOS line [59]; however the complexity brought by the post-CMOS process had forestalled the realization of these arrays, hence no image was obtained.

In a proceeding research, development of the SOI-CMOS process yields 128 x 128 array using similar pixels with 70 μm with slightly increased fill factor of 36 % [46]. Figure 1.7 shows the thermal images obtained with this FPA. The quality of the images are significantly improved compared to Figure 1.6.

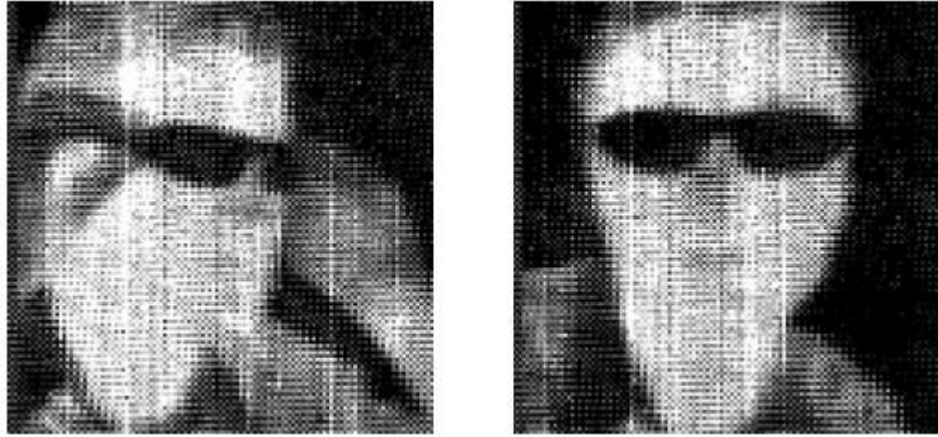


Figure 1.7: Thermal images obtained using the 128 x 128 array of SOI-CMOS microbolometer FPA. The NETD of the FPA is reported to be 1.1 K with F/1 optics [46]

In the same generation of 70 μm SOI-CMOS microbolometers, a revision is performed by [60] by constructing an array of 160 x 120 with 70- μm pixels (36 % fill factor) and improving the electronics.

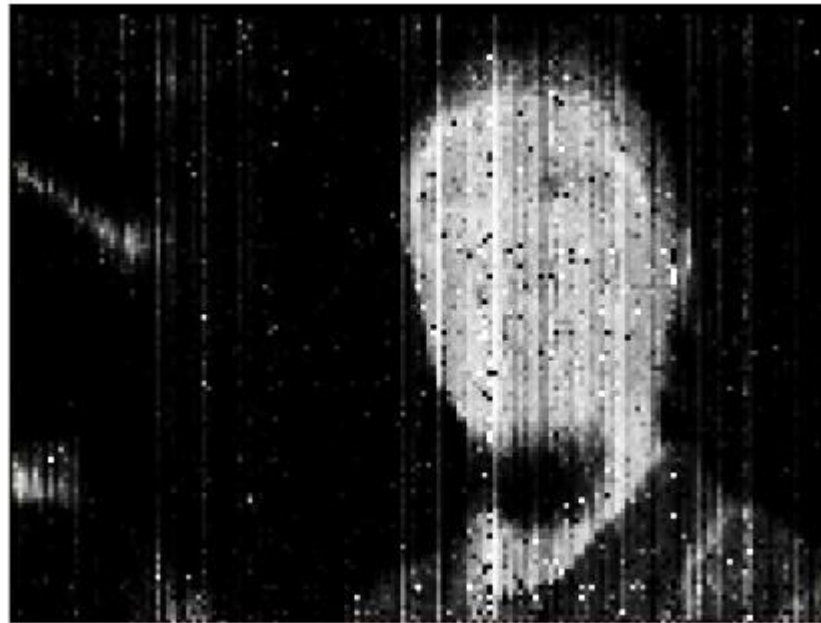


Figure 1.8: Thermal image obtained by the 160 x 120 SOI-CMOS microbolometer array with pixels of 70 μm pitch. The reported NETD value is 350 mK with optics of F/1.

Using the same generation pixel geometry, slight alterations are performed as explained in [48]. Several electronic noise sources were alleviated and power consumption of the chip had been reduced in two distinct revisions. Thermal images are recorded as a result of these revisions as shown



Figure 1.9: Thermal image obtained using the first generation 160 x 120 SOI-CMOS low-cost microbolometer FPA as a result of two revisions. The reported peak NETD is 280 mK with the optics of F/1 [48].

The same investigation of the first generation low-cost microbolometer FPAs conducted in [48], includes the development of second generation FPAs that embodies pixels with 50 μm pitch that has narrower arm widths and narrower etch gaps that are utilized in post-CMOS processes. The fill factor of these detectors is 46.2 %, which is the highest value obtained within the low-cost pixels designed and produced concerning the studies conducted at the METU-MEMS Research Center. Although there are no studies reported regarding the measured performance of the second generation low-cost microbolometer FPAs, the expected NETD value is reported to be 290 mK as a result of series of simulations and modeling [48].

1.4 Absorption Enhancement in Pixel Level

Performance can be improved in system level such as better vacuum level, greater average transmission of the optics in the region of interest or lower noise in the readout electronics; however, pixel level improvements are advantageous if the low-cost nature of the FPA fabrication is kept intact. The parallel processing technology when combined with wafer level vacuum packaging causes the fabrication cost to be reduced significantly. Therefore, implementing pixel arrays that are superior in terms of harvesting and transducing the incident infrared power brings a great advantage to lower the NETD of the system without increasing the cost much. Considering an uncooled microbolometer camera with given specifications of the readout electronics, optics, and vacuum performance, it is crucial to take advantage of the incident infrared power as much as possible. Equation 1.7 shows that fill factor affects the responsivity of the detector immensely since it defines what fraction of the incoming radiation is actually sensed by the temperature sensitive element. Due to the requirement of one-level pixel design that is brought by the limits of bulk micromachining, the past FPAs fabricated and reported [46, 48, 55, 57, 58, 60] all suffer from low fill factor since highest fill factor reported is 46.2 %. There are however, multiple approaches that are presented in order to increase the fill factor of the microbolometers. One simple way to increase the fill factor is to implement an additional structure that spans the pixel so that the infrared light that would have interact with the areas outside the pixel body, are turned into measurable signal due to being absorbed by the added structure. These structures are commonly referred as *umbrella* structure due to physical resemblance. Figure 1.10 shows the comparison of identical low-cost pixels with and without umbrella structures. It is evident that the light that would transmit through the pixel arms and the pixel frame are collected by the umbrella structure and the absorbed energy is transferred to the pixel body via heat transfer.

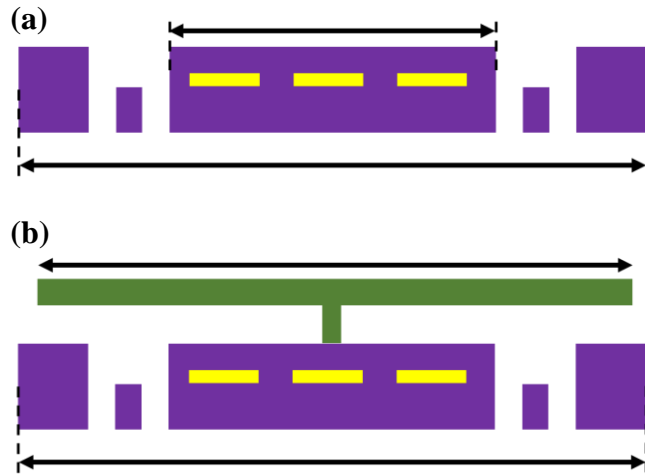


Figure 1.10: Schematic representation of a unit low-cost pixel (a) without any additional structures, (b) with additional structure that increases the fill factor.

In the next subsections, various approaches to pixel level performance improvement are presented in order to construct a healthy context for the objective of this study.

1.4.1 Diode-type Microbolometers employing high fill factor designs

The first successful SOI diode uncooled microbolometer FPA fabrication by Mitsubishi is presented in 1999 [47]. The FPA comprises an array format of 320 x 240 consisting of pixels with 40 μm pitch. Figure 1.11 shows the first low-cost diode uncooled microbolometer implementing a structure to increase the fill factor. The measured NETD of this array is reported to be 200 mK at F/1 optics. After the first successful demonstration, series of different pixel structures are proposed and tested in terms of performance and fabrication complexity by the same group. The first improvement made aims to lower the thermal time constant since a thick dielectric layer is required ($\sim 2.5\text{-}\mu\text{m}$ thick) to create a resonant structure between the reflector and the absorber. Moreover, the post numbers are increased to allow better heat transfer and the reflector position is altered to allow more efficient cavity resonance; the resulting NETD value of this FPA is reported to be 120 mK at F/1 optics [49].

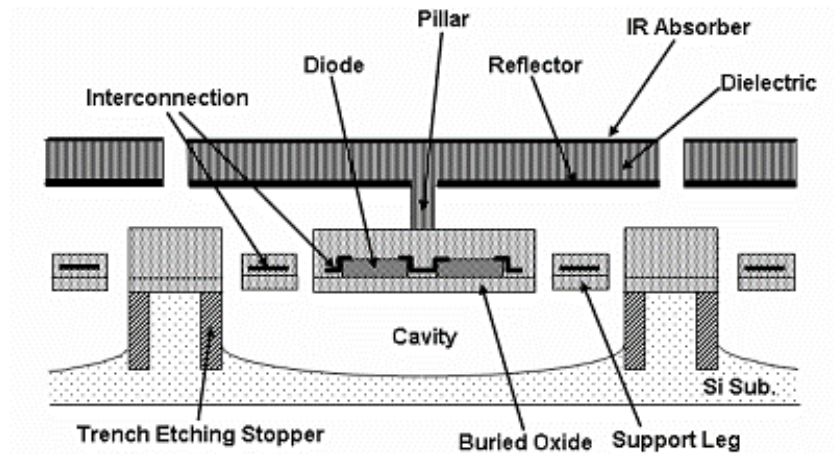


Figure 1.11: Cross-sectional schematic view of the SOI diode uncooled microbolometer pixel with high fill factor (90 %) achieved using umbrella structure that spans the pixel [53].

Figure 1.12 shows the schematic view of the improved design, where the absorbing structure is much thinner and the reflector planes are moved into the body to allow cavity resonance.

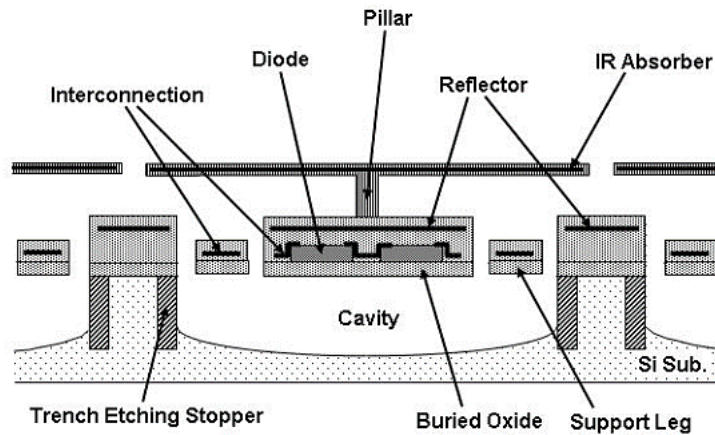


Figure 1.12: Cross-sectional schematic view of the SOI diode uncooled microbolometer pixel with high fill factor (90 %) achieved using umbrella structure that spans the pixel with reflector on the pixel body and the arms [53].

For smaller pixel sizes below $35\mu\text{m}$ pixel pitch, it is claimed that the reflector metals are not feasible due to small body and greater space to provide longer arms to meet

the required thermal conductance (G_{th}) specification. Therefore, another improvement has been introduced, where the reflector deliberately covers the pixel body and the space between the pixel body and the frame as seen in Figure 1.13 .

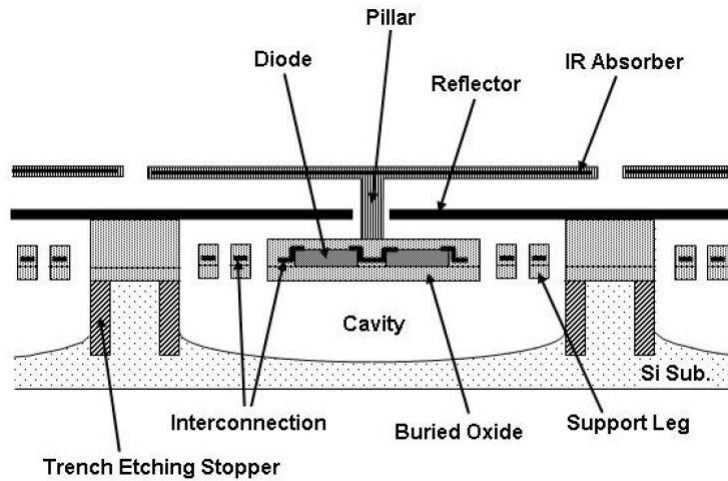


Figure 1.13: Cross-sectional schematic view of the SOI diode uncooled microbolometer pixel with improved reflector structure that is tailored for smaller pixels to obtain high fill factor (90 %) achieved using umbrella structure that spans the pixel with reflector on the pixel body and the arms [53].

This particular umbrella structure is implemented on pixels with 28 μm pitch that has longer arms and the measured NETD of the same array size with 28- μm pixels is 87 mK at F/1 optics [61]. Figure 1.14 shows the SEM images of this detector.

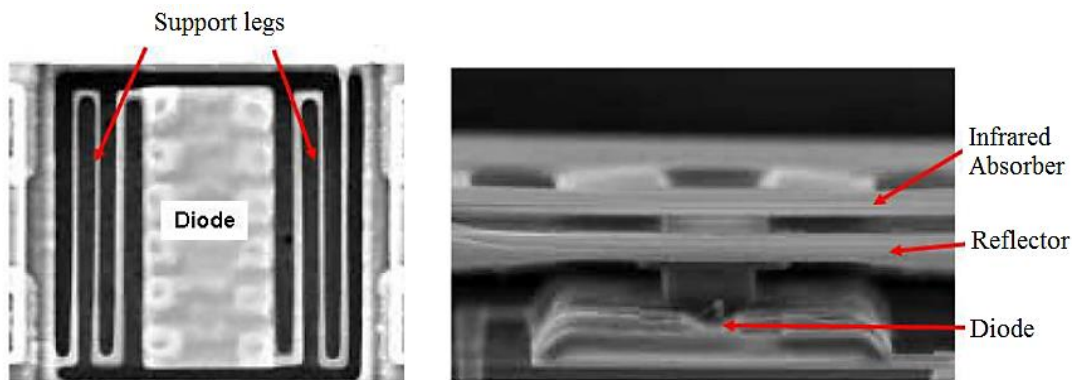


Figure 1.14: SEM images of three-level SOI diode uncooled pixel structure with a pitch of 28 μm (a) top view and (b) side view [53].

Using the pixel structure shown in Figure 1.13, smaller pixels are designed with pitch length of $17\ \mu\text{m}$ to form the same array size of 320×240 on an FPA. The measured NETD of the $17\ \mu\text{m}$ pixel pitch FPA is reported to be $77\ \text{mK}$ at F/1 optics [42]. All of the umbrella structures that are exemplified above utilize PECVD grown silicon nitride (SiN) due to its superior mechanical, thermal, and optical properties that will be discussed in Chapter 2 in a detailed manner. In addition, amorphous silicon is used as the sacrificial layer due to availability and ease of fabrication. The entire pixel and the umbrella structures are then released in a dry isotropic etching process with XeF_2 gas [42].

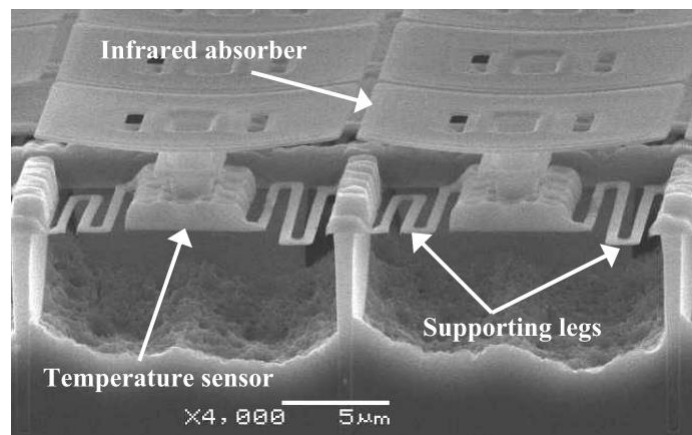


Figure 1.15: SEM image of the SOI diode $15\ \mu\text{m}$ pitch pixels including absorber umbrella structures developed by [62]

Another SOI diode uncooled microbolometer detector involving high fill factor design is presented on a pixel with $35\ \mu\text{m}$ pitch [63, 64]. The study has been focused on mechanical and thermal properties of the fabricated pixel arrays, where residual stress problems are addressed. Although the operability is not reported, measured NETD of the pixel array is reported to be $42\ \text{mK}$ at F/1 optics [63]. The difference of this structure is to utilize three material stack (silicon nitride, titanium nitride, and silicon dioxide) to form a tunable cavity.

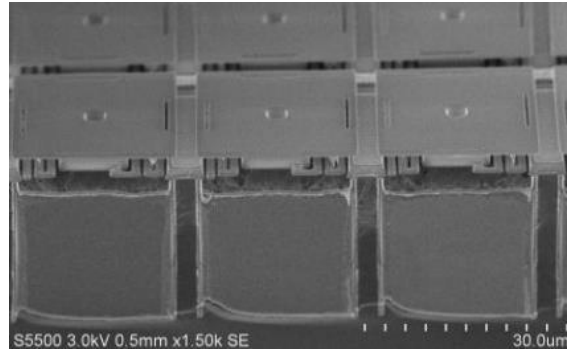


Figure 1.16: SEM image of the fabricated uncooled SOI-diode FPA with the umbrella design [64]

1.4.2 Resistive microbolometers employing high fill factor designs

Similar approach to the aforementioned method has been followed by one of the major uncooled imager providers, DRS Technologies. The resistive, VO_x microbolometers are used to construct the FPA. Due to down-scaling of the pixel pitch trend in the last decade, the low responsivity problem is inherent since the detector area is decreased while more space is needed for longer support arms to maintain the necessary thermal conductance. Therefore, the fill factor of the detectors are reduced significantly in one-level design, where $17\ \mu\text{m}$ pitch pixels are used to construct an array of 320×240 and 640×480 incorporating umbrella absorbing structures [65, 66]. Figure 1.17 shows the SEM image of the constructed FPA with the umbrella structure implemented atop.

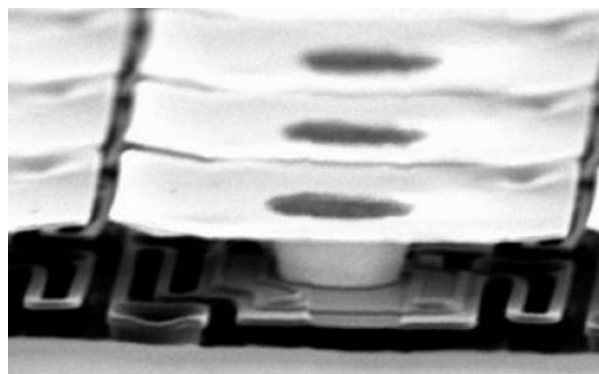


Figure 1.17: SEM image of one-level VO_x microbolometer designed with absorbing umbrella structures to increase the fill factor [65].

Experimental work on tuning the sheet impedance of the umbrella structure is also performed while reducing the thermal mass of the umbrella structure in order to achieve low time constant values for the microbolometer pixels [66]. The measured NETD value for the FPA is reported as <50 mK at F/1 optics [65]. Further improvements are tuned to overcome the residual stress problems as the structural layers are thinned in order to decrease the thermal mass of the sensor [67]. One of the unique properties of this design is that the sensor layer stack benefits from double optical cavity as seen in Figure 1.17 since there is a reflector underneath the pixel structure that comprises the first optical cavity.

Another two-level design (referred as *eaves structure*) is implemented in the same manner on pixels with 23.5 μm pitch forming an array of 640 x 480 by another industrial supplier [68]. The resistive VOx type microbolometer is used in the design, and umbrella structures are added to compensate for the loss of infrared signal due to down-scaling the pixel pitch from 37 μm to 23.5 μm . In addition, the space occupied by the thermal isolation structures is increased to maintain the desired thermal conductance so that the fill factor is reduced from 72 % to 60 % [68]. Figure 1.18 shows the SEM image of the pixels with the umbrella structure.

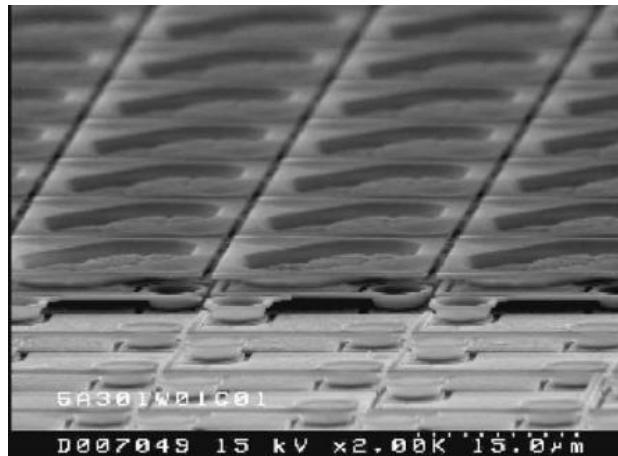


Figure 1.18: SEM image of the pixels with 23.5 μm pitch having an absorbing high fill factor structure that extends through each pixel [68].

The fill factor is increased up to 92 % from 60 % with the addition of umbrella structures; and the resulting responsivity is increased by a factor of 1.3 [68].

1.4.3 Fill Factor Improving Designs on Other Uncooled FPAs

Apart from microbolometers, other types of uncooled detectors that suffer from low fill factor are implemented with umbrella-type structures to improve their responsivity [14, 69, 70]. One example is given on a thermoelectric detector that exploits similar geometry to that of microbolometer pixels [69, 70]. Polysilicon wires construct the main body of the hot junction of the thermoelectric detector while most of the absorption is provided by the silicon nitride (SiN) that is approximately 1 μm thick.

The choice of material is justified with the ease of fabrication, high extinction coefficient, and having low residual stress. Longer wires are utilized than usual in this study to fully take advantage of the thermal isolation since thermoelectric effect yields lower temperature sensitivity compared to resistive and diode type microbolometers [69]. Therefore, the probability of mechanical failure due to the umbrella structure is analyzed as well.

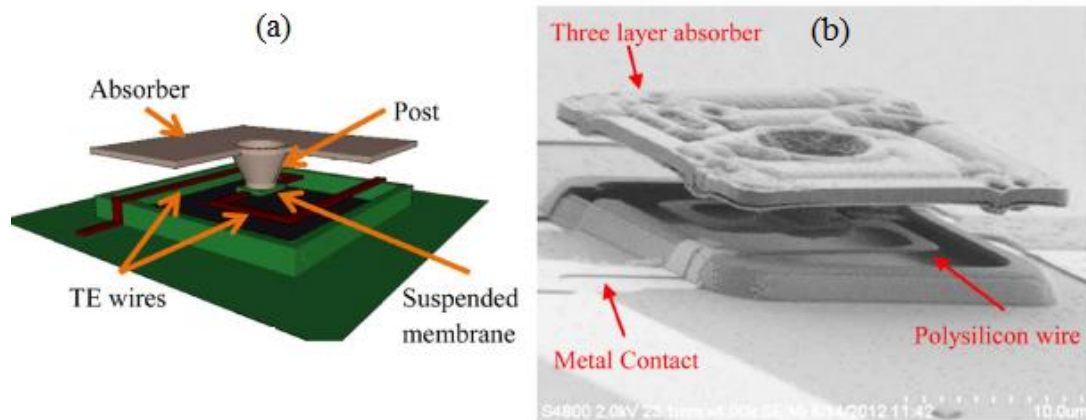


Figure 1.19: Uncooled thermoelectric sensor including an umbrella structure to increase the fill factor, where (a) schematic representation and (b) SEM image of the completed device is provided [69].

Another work on increasing fill factor of the metallic thermoelectric array as elaborated in [71]. In order to achieve high fill factor without compromising from the thermal isolation structure geometries, the umbrella layer constructed where the temperature sensitive element itself lies on, which provides a slightly different approach. Figure 1.20 shows the representative view of the thermoelectric sensor with the umbrella structure of which the fill factor is 92 %.

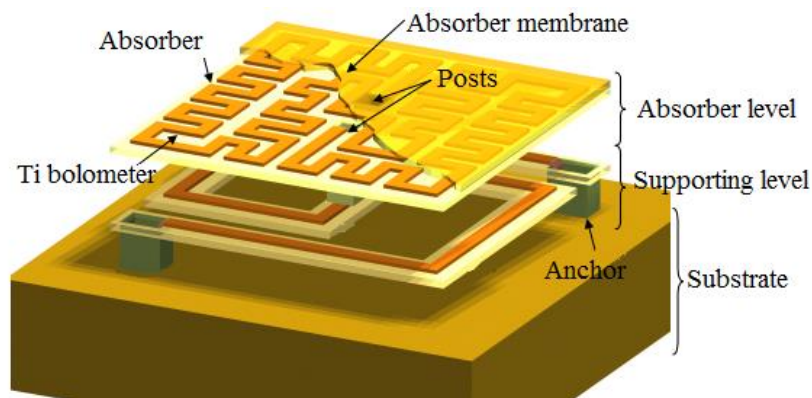


Figure 1.20: Schematic view of the thermoelectric bolometer employing a two-level structure that expands through the unit cell [71].

This structure, however is somewhat different since the umbrella layer itself embodies a part of the temperature sensitive element. It is similar to a conventional method usually applied on the high-performance surface micromachined uncooled detectors, where the thermal isolation legs of the detector are hidden underneath the absorbing layer in a two-level process [35, 40, 72].

A different example of high fill factor structure implemented on a thermoelectric detector array (thermopile) is introduced in [14].

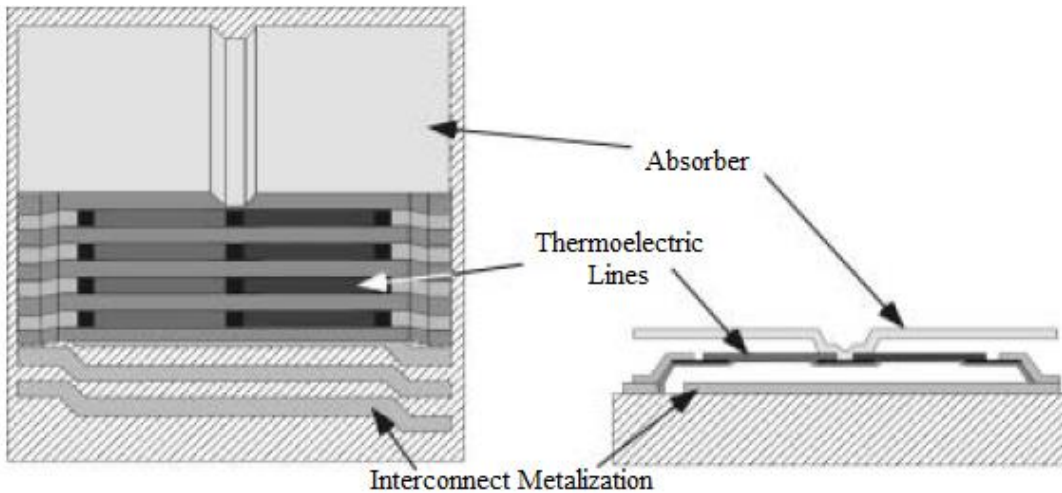


Figure 1.21: Schematic diagram of the thermoelectric detector structure involving an umbrella absorber to produce high fill factor [14].

The insensitivity of the detector to the variations of the substrate temperature makes the thermopiles a suitable candidate for many applications, however the required temperature sensitivity precludes them to be a major choice of detector in many cases. On the other hand, modifications on the pixels that enable efficient infrared absorbing mechanisms pave the way for meeting the requirements for myriad of applications, in this case Mars Climate Sounder [14].

In short, there are multiple uncooled infrared detectors that utilize additional mechanical structures in order to obtain high fill factor designs for high responsivity. Most commonly, these additional structures consist of an optical cavity tuned to absorb the most at the desired wavelength range. The thermal energy absorbed by the high fill factor design is then transferred to the temperature sensitive element.

1.5. Research Objectives and Thesis Organization

In accordance with the context that is introduced in this chapter, the main objective of this study is to design and implement an umbrella-type structure that increases the fill factor up to 94 % in order to maximize the responsivity of the detectors. To verify the desired goal, the implemented umbrella structures are tested on existing low-cost detector testing platform.

Firstly, the compatibility of several materials are considered including the methodologies pertaining to deposition, patterning, and removal of these materials and the compatibility of the required tools to achieve the final desired geometry. Chapter 2 deals with the compatibility of two main candidate materials to be used as the umbrella material on the existing low-cost microbolometers. Mechanical simulations are performed using finite element method (FEM) software to assess the profile of the umbrella structures after being suspended. In addition to the mechanical stability, optical properties of two candidate dielectric layers are discussed and optical simulations are performed in 2D and 3D to design an efficient umbrella structure comprising an optical cavity using a commercial finite difference time domain (FDTD) solver. Since the absorbed optical power is transferred via thermal energy through the posts of the umbrella structure on low-cost microbolometers, transient thermal simulations are run on the same FEM software to evaluate the contribution of the umbrella mass to the total thermal mass of the microbolometer.

Upon concluding the discussion on applicable umbrella material and the window of design parameters, in Chapter 3, realization of umbrella structures are reviewed firstly on bare silicon substrate as proof of concept. Then optimized fabrication steps are explained to overcome the problems that are addressed while fabricating umbrella structures on low-cost microbolometers on wafer level.

After the demonstration of successful integration of umbrella structures on low-cost FPAs, Chapter 4 describes the optical response testing as well as the responsivity measurement procedure of the low-cost microbolometers in vacuum conditions.

Finally, Chapter 5 conveys the conclusions drawn as a result of this research in the context formed in Chapter 1. Moreover, the ongoing and future work are remarked concerning the performance enhancement in reference to existing approaches reported in literature. Some of the preliminary results are also presented.

CHAPTER 2

PIXEL LEVEL UMBRELLA STRUCTURE DESIGN

In order to realize umbrella geometries for the low-cost microbolometers that were developed under the roof of METU-MEMS Research Center, series of feasibility studies are reviewed. Considering that the structures to be employed as to increase the fill factor of the predefined detectors are mechanically significant, their residual stress must be low enough to allow free-standing assemblies. In addition, the material to be used to realize these structures must have enough mechanical strength to endure the free-standing layer throughout the entire pixel span of tens of microns.

Moreover, the umbrella material must be sufficiently absorbing in the imaging window of 8–12 μm wavelength for high performance. The absorption coefficient indicated as α in Equation 2.1 is linearly proportional to the extinction coefficient, k , of the material. Thus, the requirement indicates a material with high extinction coefficient in the wavelength region of interest for high absorption.

$$\alpha = \frac{4\pi k}{\lambda} \quad (2.1)$$

Therefore, optical and mechanical properties of two dielectric layers are investigated and surveyed in the following two sections specifically for the application of umbrella structures on low-cost uncooled infrared detectors. Then, thermal simulations are performed to analyze the contribution of the umbrella structures to the total thermal mass of the detectors. It is, however, worth mentioning that the design procedure of these structures is highly modular, meaning that the outcome of the optimization

modeling can simply be tailored to fit with myriad of detector arrays regardless of their FPA size, material, and geometry although slight alterations may be required.

2.1. Mechanical Properties of Silicon Dioxide and Silicon Nitride

The selection of materials was narrowed down to two major candidates due to ease of fabrication, compatibility with MEMS fabrication techniques, and having non-transparent IR characteristics. The deposition of umbrella layer has to be within certain temperature limits due to having CMOS interconnect metals; hence plasma enhanced chemical vapor deposition (PECVD) devices must be used for low temperature deposition of the umbrella layer. In order to obtain free-standing structures without buckling problem, residual stress of the deposited material has to be as low as possible [73-75]. While the average stress comprises two main components being in-plane and vertical gradient, the latter mainly causes the buckling of free standing monolayer structures [74, 76]. Although rapid thermal annealing (RTA) has been proven to be effective in reducing the stress gradient in growth direction [77], such thermal treatments may cause degradation of temperature sensitive bolometric materials not to mention the damage it will cause to the CMOS metal layers.

The requirement of low stress gradient is applicable to monolayer cantilever-type mechanical structures as this is the case for the umbrella layer since the anchor of the umbrella layer sets a fixed constraint on one side only [76]. Therefore, the feasibility of the two dielectric materials will be investigated mechanically in the following subsections.

2.1.1. Mechanical Properties of PECVD Silicon Dioxide (SiO₂)

Silicon dioxide deposited using PECVD tools, has been studied extensively for MEMS integration and realization of 3D structures in the literature due to being a common passivation layer in the integrated circuit (IC) industry [73, 78]. Although stress values as low as 51 MPa as the bulk residual stress values are obtained as exemplified in [74], having free standing structures using PECVD silicon dioxide has been problematic due to high vertical variation of the stress [76]. METU-MEMS

facility offers two separate PECVD tools with various optimized recipes to deposit silicon dioxide, and the measured stress values change between -120 MPa and -200 MPa (tensile) with relatively high variation in the direction of the growth.

A sweep of stress gradient is applied to FEM simulations using COMSOL Multiphysics tool for a simple umbrella geometry. A square slab that is 800nm thick with a span of 48 μm is fixed with a 5 μm x 5 μm square single post. The entire geometry material is chosen to be SiO₂ from the built-in library of the software, and -150 MPa average stress is added to the material. Then, a linear stress gradient is applied to the square membrane only varied from 5 MPa/ μm to 25MPa/ μm with steps of 5 MPa/ μm . As experimental form suggests in [79], more compressive stress is induced on the top surface of the 800nm thick umbrella layer while the bottom surface is defined as more tensile. Figure 2.1 shows the resulting displacement plot for 25MPa/ μm gradient (The 3D plot is exaggerated for visual convenience).

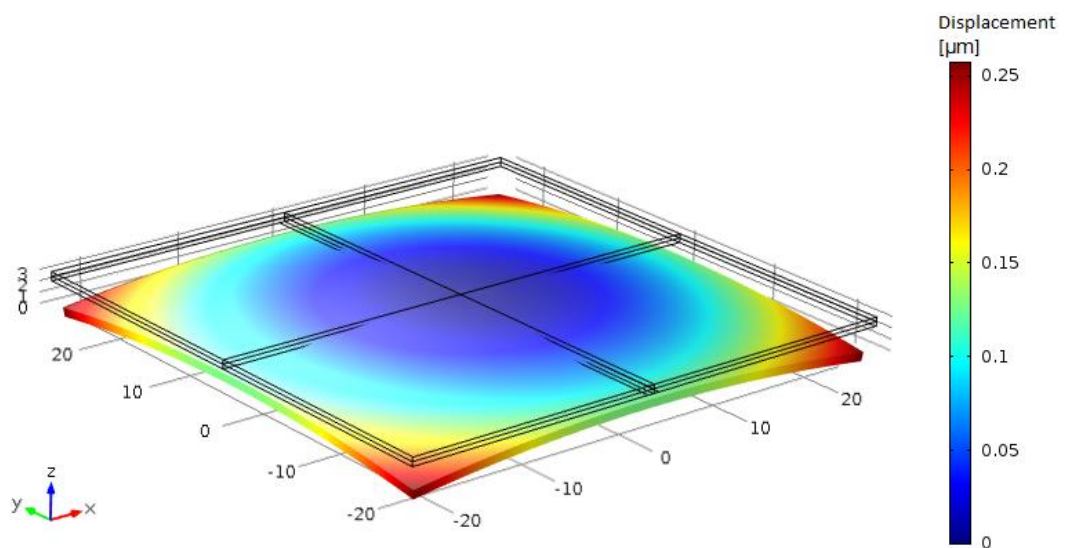


Figure 2.1: 3D FEM simulation results, exaggerated for visual convenience, displayed with absolute value of the maximum surface displacement. Note that the stress gradient applied bends down the umbrella layer with a maximum of 30% strain in the growth direction, which is a significant deflection for this geometry.

It is evident that under such stress gradient, the umbrella membrane undergoes a 30% strain in the vertical direction. Considering the modularity of the umbrella structure, if any additional layers or geometries are designed to be integrated, the resulting deformation may easily jeopardize the proceeding steps.

2.1.2. Mechanical Properties PECVD Silicon Nitride (SiN)

In contrast to SiO₂, non-stoichiometric silicon nitride deposited using PECVD tool (SiN) has advantages considering stress related applications. It is possible to tune the residual stress of the silicon nitride in a wide range from +850MPa (compressive) to -300MPa (tensile) by alternating plasma excitation frequency in the PECVD tool as demonstrated in [74]. Using various gas flow ratios into the chamber during deposition is also proven to be an effective method to produce stress free SiN films [80]. Another study produces results on tuning the stress gradient of SiN films deposited utilizing PECVD by changing the RF power [81]. The aforementioned two PECVD tools used in METU-MEMS Research Center are both capable of depositing silicon nitride films below 10 MPa compressive stress with very little vertical stress gradient by changing excitation plasma frequency. The same two PECVD tools, however, have significantly less control over intrinsic stress of the SiO₂ film. It is also shown in [74] that changing excitation frequency has no effect on the intrinsic stress of SiO₂ grown using PECVD.

A sweep of stress gradient is applied to the same geometry as explained in the previous subsection (800nm-thick square slab with a span of 48 μ m and anchor size of 5 μ m square). The built-in material properties are used as they are defined in the COMSOL Multiphysics MEMS module. Initial average stress of +10 MPa is also applied to the square slab. Then, a linear stress gradient is applied to the square structure only, varied from 5 MPa/ μ m to 25 MPa/ μ m with steps of 5 MPa/ μ m. Figure 2.2 shows the exaggerated 3D perspective view of the SiN umbrella structure under 25 MPa/ μ m stress gradient.

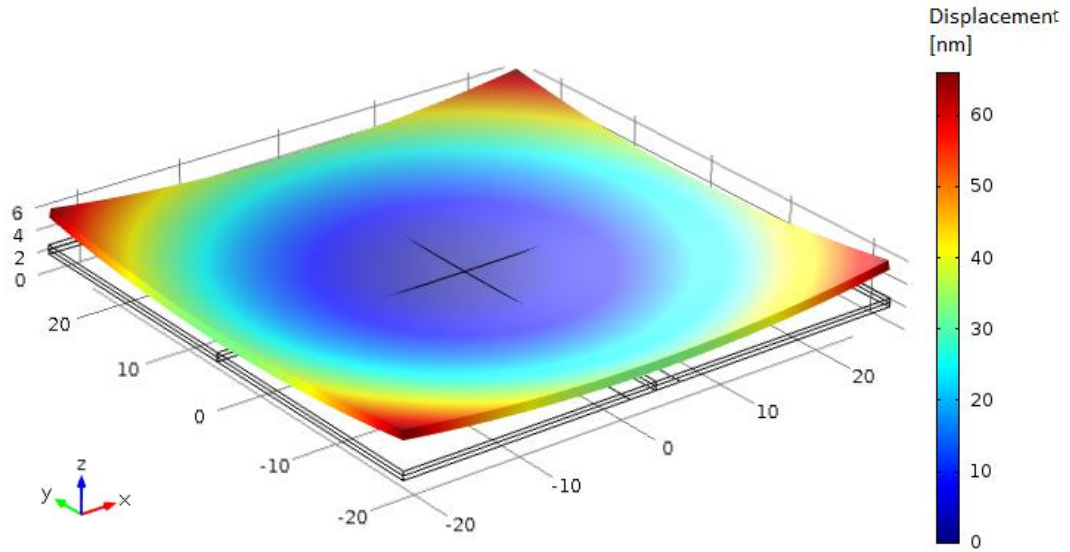


Figure 2.2: 3D FEM simulation results –exaggerated for visual convenience– displayed with absolute value of the maximum surface displacement in z-direction. Note that the stress gradient applied bends up the umbrella layer with a maximum of 7.5% strain in the growth direction, which is relatively low compared to the SiO₂ material umbrella structure.

It is conspicuous that the maximum curl points of the square umbrella structure is significantly less than that of SiO₂ umbrella structure. Under the same stress gradient values (25 MPa/μm), the maximum deflection that SiN produces is 67 nm while the same stress gradient causes 257 nm deflection for SiO₂ film. Figure 2.3 shows the absolute value of maximum deflection occurs due to stress gradient at various gradient values. Indubitably, SiO₂ film is more prone to deflections under stress gradient.

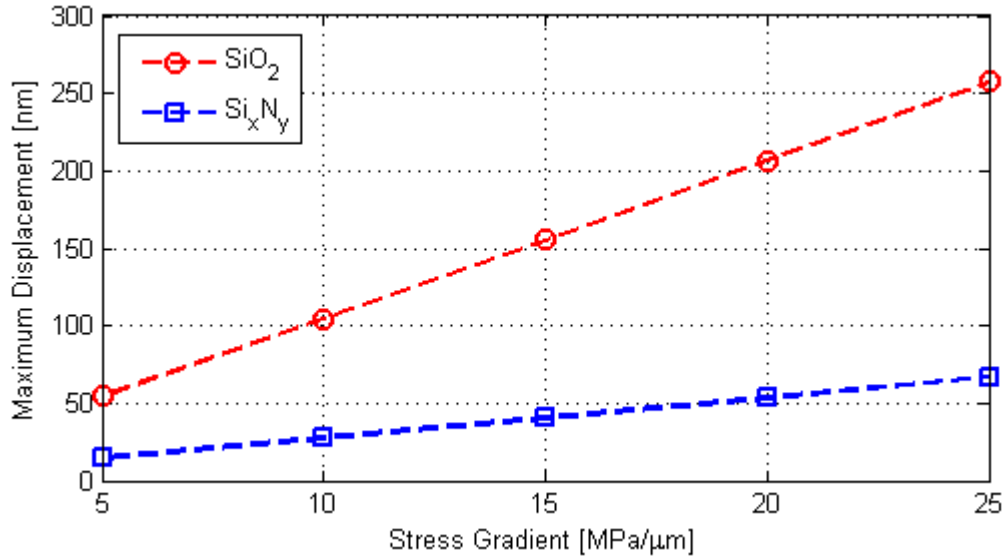


Figure 2.3: Maximum displacement of the simulated square umbrella structures (800nm thick and 48μm wide with 5μm anchor in the center) under varying stress gradient values. Under increasing stress gradient, SiO₂ evidently produces more deflection, which is an undesired effect.

In summary, silicon nitride exhibits mechanical characteristics that are more suitable for the intended umbrella fabrication. The next section deals with the optical characteristics of the two dielectrics in juxtaposition.

2.2. Optical Properties of Silicon Dioxide and Silicon Nitride

As mentioned in the beginning of this chapter, high extinction coefficient materials are desired in the LWIR window for high absorption, hence high responsivity and performance. The optical characteristics of the two aforementioned dielectric layers in the region of interest were investigated using Infrared Variable Angle Spectroscopic Ellipsometer (IR-VASE). As a result of this measurement technique, two important parameters (ψ and Δ) are measured spectrally. ψ signifies the amplitude ratio of the reflected s- and p-polarized light while Δ is denoted as the phase difference induced by the reflection [82]. Figure 2.4 shows the schematic view of the measurement setup.

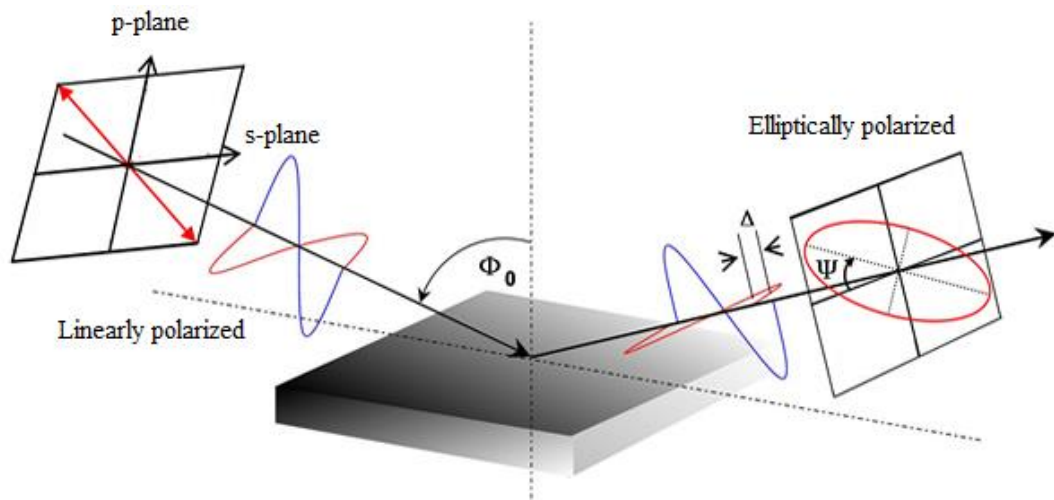


Figure 2.4: Schematic representation of ellipsometric measurement. Linearly s- and p-polarized light is reflected from the sample surface at varied incident angles (Φ_0) producing phase difference (Δ) and different amplitude ratios (ψ) picked up by the detector. The interaction of the light determines the material characteristics in the infrared region [82].

Measured values are, then fitted to a model constructed by the user with parameters such as film thickness and optical oscillator parameters. The least-squares regression algorithm is utilized to calculate corrections to the user defined first-guess parameter values. Thus, with iterative computation, the model is fitted to optical parameters that closely match the measured ellipsometric data [83].

2.2.1. IR-VASE measurements and Characterizations

For characterization purposes, four 6" silicon substrates were sputtered with 100nm gold in order to provide a perfectly reflecting substrate for the dielectric materials of interest. Then two gold coated wafers were deposited silicon dioxide (SiO_2) using two separate recipes in separate PECVD tools. In the same fashion, non-stoichiometric silicon nitride (SiN) was deposited on two wafers using stress-free recipes. Ellipsometric measurement was performed in the $3\mu\text{m}$ - $20\mu\text{m}$ range using J.A. Woollam IR-VASE. Figure 2.5 shows the schematic of the layer stacks for characterization purposes.

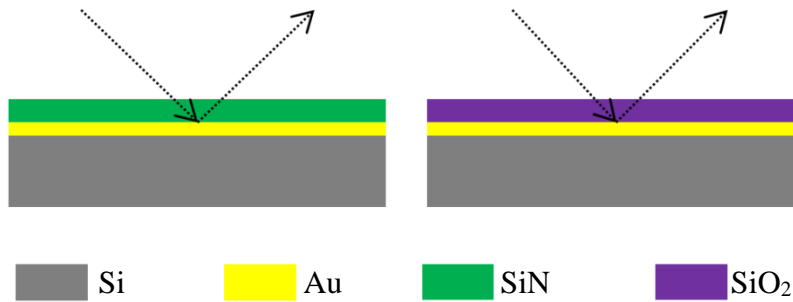


Figure 2.5: Schematic view of the dielectric deposited wafers for IR-VASE measurement.

Note that the gold layer underneath the dielectric layers is thick enough to be optically opaque, hence no light interaction occurs with silicon substrates. Dashed arrows represent polarized the infrared radiation.

Obtained ψ and Δ data are fitted with built-in library oscillator parameters for SiO_2 and SiN . Thickness values are bound within a known range and oscillator functions are fitted to the obtained data. Each spectral measurement is performed at four different incident angles in the range of 40° to 70° with a step of 10° . Figure 2.6 shows the ellipsometric fit result of SiO_2 film on the gold coated substrate. The fit results in an acceptable root mean square error, and thickness uniqueness fit –meaning the fit algorithm is run for neighboring thickness values of the material to see if the parameter fit converges to a global or a local minimum. Presence of a narrow and strong oscillator due to Si-O-Si stretching around $8.5\mu\text{m}$ is expected in general [82]. In parallel with the theory, similar behavior is observed regarding the measured SiO_2 films deposited at METU-MEMS facility.

In the same manner, SiN data obtained are fitted using a general oscillator, and fit quality is checked using uniqueness fit as well. Figure 2.7 shows the ellipsometric fit results of the deposited silicon nitride film.

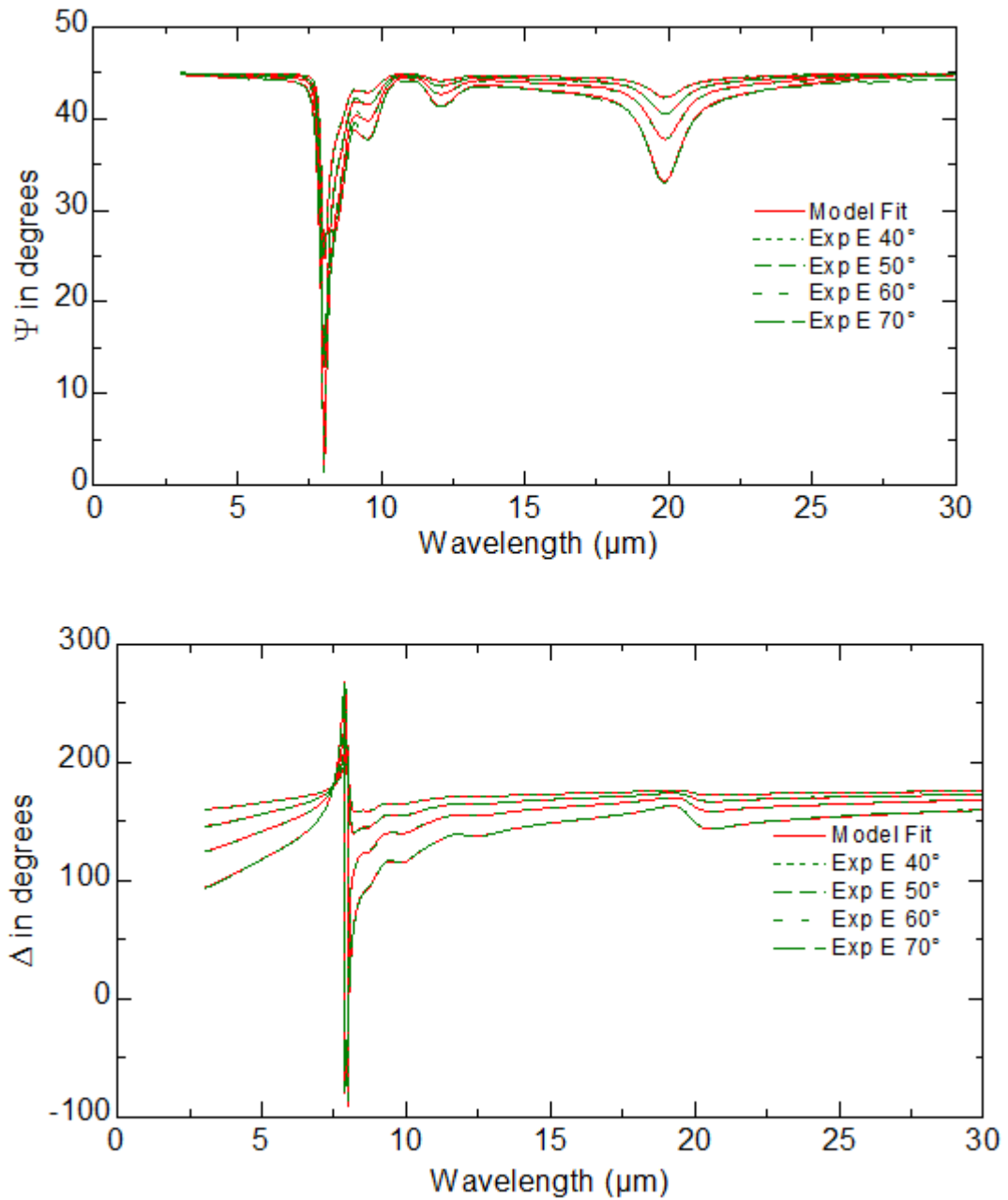


Figure 2.6: Fitted spectral ψ and Δ data of SiO_2 film deposited on gold using PECVD. Note the abrupt change in both plots implying a strong oscillator around $8.5\mu\text{m}$ wavelength.

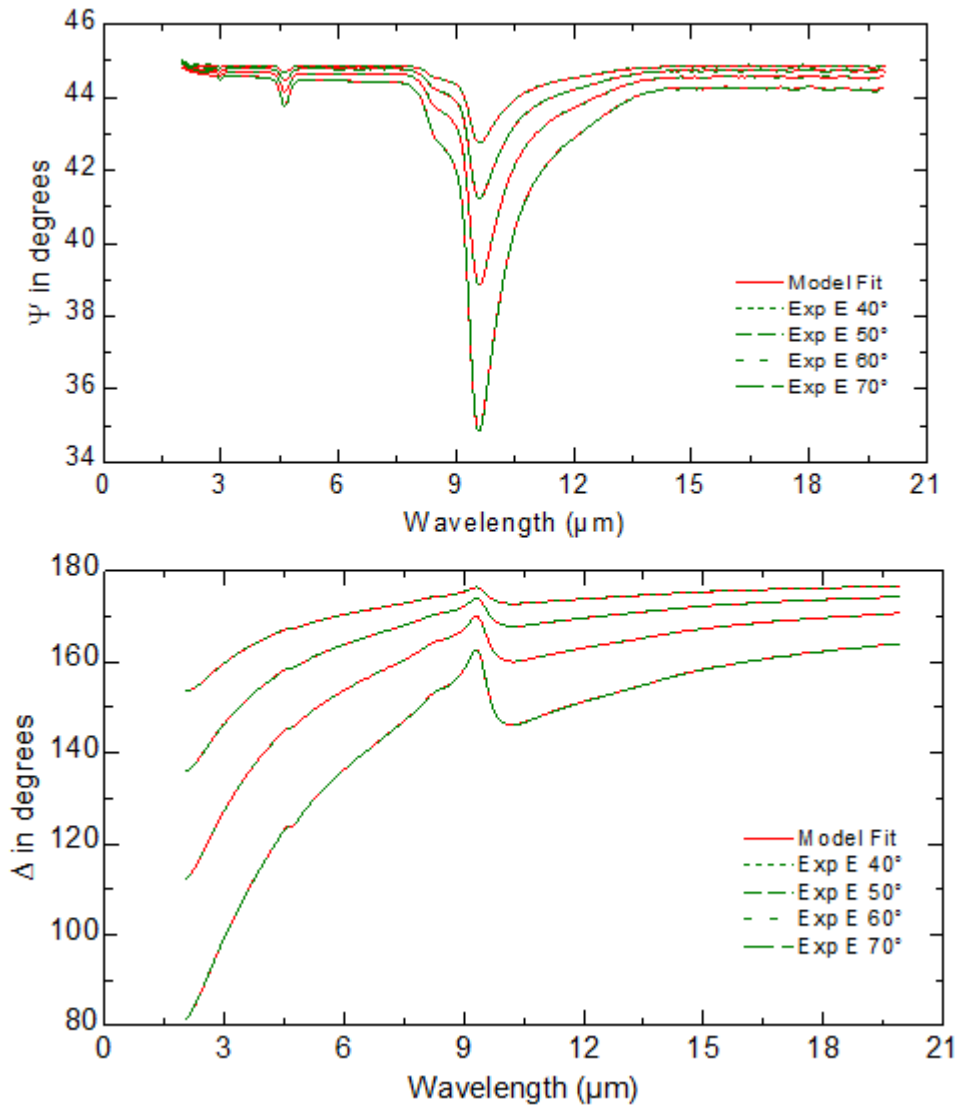


Figure 2.7: Fitted spectral ψ and Δ data of Si_3N_4 film deposited on gold using PECVD. Note the change in both plots implying a broader oscillator around 9 μm wavelength.

Analogous to oxides of silicon, silicon nitride has an optical response around $9\mu\text{m}$ wavelength due to stretching mode of Si-N bonds [84, 85]. Figure 2.8 displays the optical constants that are extracted by fitting the model to the acquired data by ellipsometric means. This result is also consistent with reported values in [86]. It is concluded that the optical characteristics of each dielectric materials using two different PECVD tools result in substantially similar trends.

Although it is possible to adapt the refractive index and the extinction coefficient to specific application needs by altering deposition conditions [87, 88] , the procedure pertaining to such modifications, however, is beyond the scope of this thesis. Therefore, available deposition technologies at the METU-MEMS Research Center are considered only as they are.

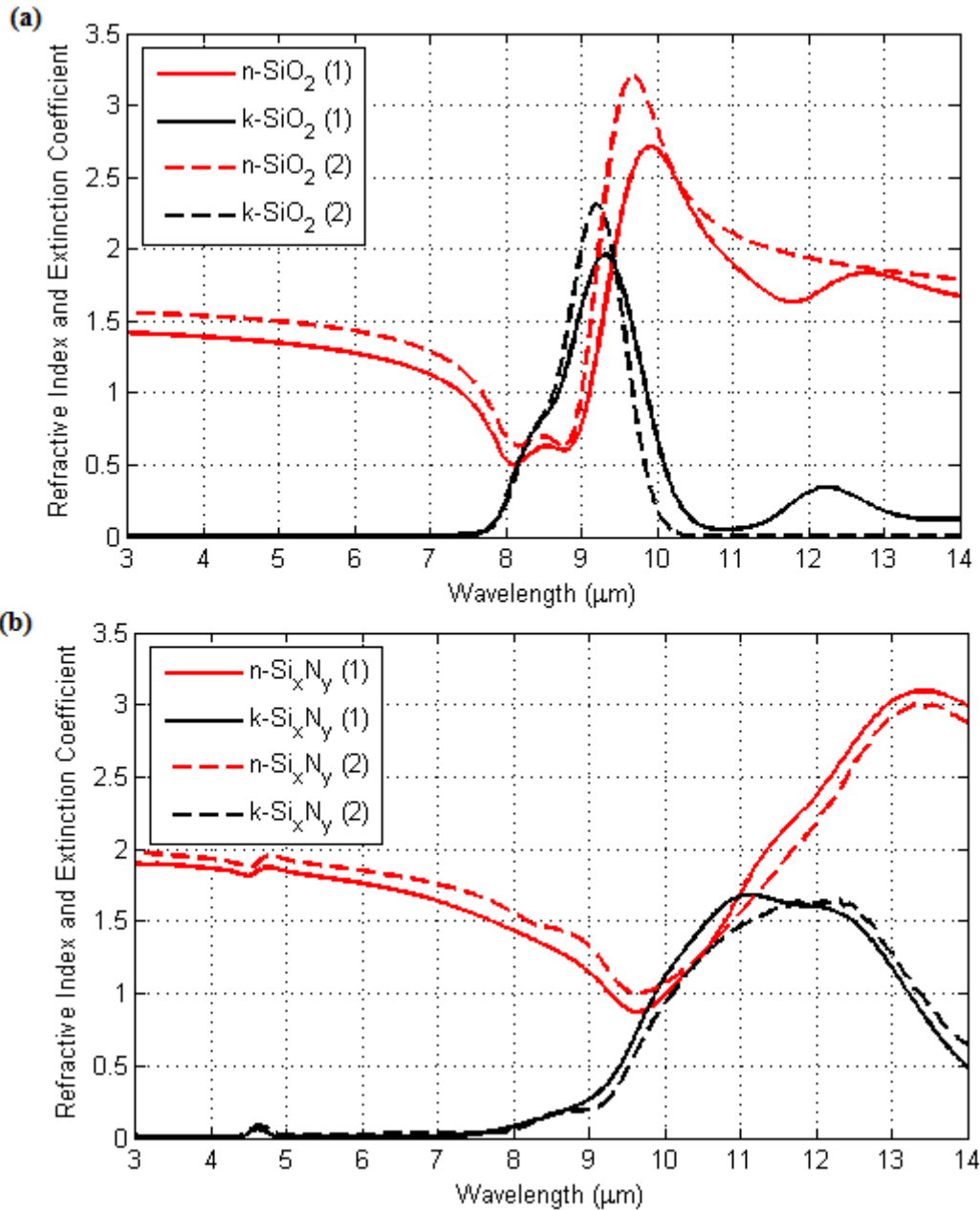


Figure 2.8: Optical constants (refractive index and extinction coefficient) of (a) PECVD SiO₂ and (b) PECVD SiN deposited using two separate tools –solid lines correspond to one tool while the dashed lines correspond to the material deposited using another tool as noted with a number in parenthesis. Note that the optical characteristics of each material is similar regarding the difference in the tool they are deposited in.

When the extinction coefficient of two materials are compared, as Figure 2.9 shows, a definite feature where the absorbing regions of two materials complement each

other. Thus, while silicon dioxide absorbs on the shorter wavelength of the LWIR window, silicon nitride absorbs more around the longer wavelength region utilizing the entire spectrum of interest.

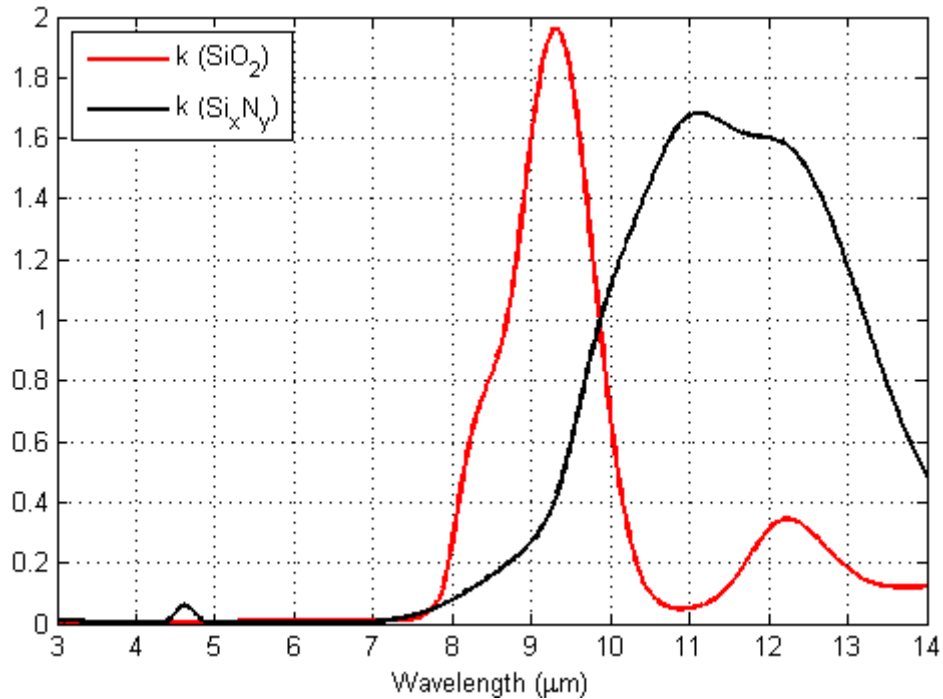


Figure 2.9: Extinction coefficient of SiO₂ and SiN overlaid. Note that the absorbing wavelength regions are complementary for both materials; meaning while SiO₂ absorbs relatively lower wavelengths of the LWIR window, SiN absorbs in the longer wavelength region.

In summary, the optical characteristics (refractive index and extinction coefficient) of PECVD SiO₂ and SiN are obtained and presented. It is concluded that regardless of the deposition tool, optical characteristics were substantially similar. In the next section, these characteristics will be used to simulate the absorption trends of various geometries.

2.2.2. FDTD Simulations of basic 2D umbrella slab

In order to validate the extraction of optical constants and the efficacy of the FDTD modeling, two samples were prepared as schematically shown in Figure 2.5 for reflection measurements. The spectral reflection measurements, $R(\lambda)$, are performed using a Bruker Vertex 70 Fourier Transform Infrared Spectrometer (FTIR) with Hyperion 2000 Microscope attachment utilizing a 15x objective (0.4 numerical aperture) at a normal incidence. Absorption is then calculated as $1 - R(\lambda)$ assuming no transmission through the mirror on the bottom layer due to optically opaque gold layer deposited underneath.

Simulated absorption plots are obtained by mimicking the actual case using a commercial finite difference time domain (FDTD) solver, Lumerical FDTD Solver. Dielectric material optical constants are fed into the solver ensued from the ellipsometric measurements explained in the preceding section. Utter metal geometries concerning the pixel structure are modeled as Perfectly Electrical Conductor (PEC) layers to ease the computation requirement.

The boundary condition configuration is setup in a fashion to emulate the FTIR reflection measurements. Since the measured samples are unpatterned, the system is reduced to 2D configuration where the lateral dimension of the simulation is set to periodic boundary condition assuming infinitely large area. The bottom boundary condition is selected to be perfectly reflective since the deposited gold thickness is around 100nm beneath the dielectric layers. The top boundary condition is set to a perfectly matched layer (PML) meaning that any electric field that encounters the boundary is absorbed with no reflection; hence mimicking the reality where only the signal reflected exclusively from the surface of the dielectric is accounted for. Figure 2.10 shows the overlaid simulated and measured spectral response of SiN and SiO₂ samples that are deposited on gold substrate for zero transmission.

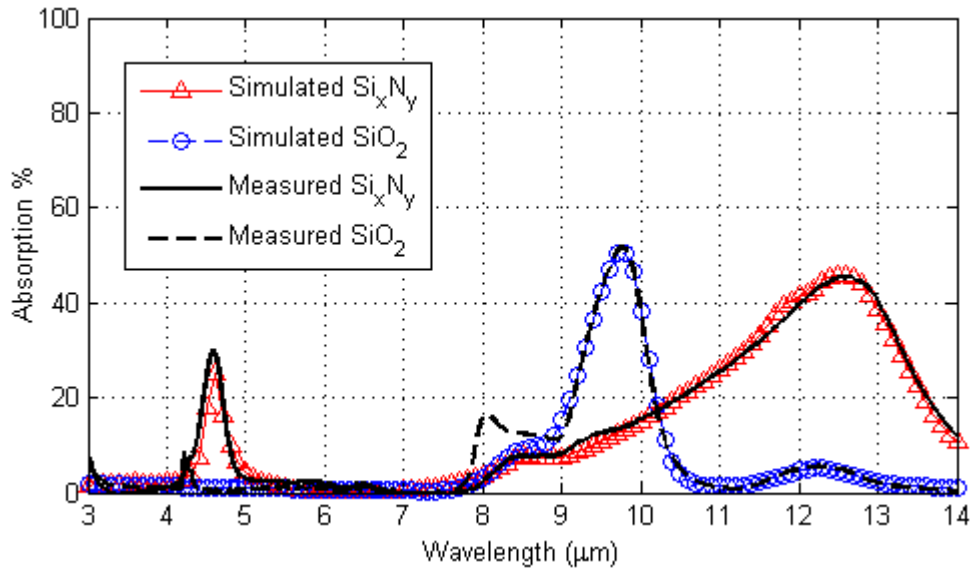


Figure 2.10: Comparison of the FDTD absorption simulation results (colored and marked) and the FTIR measurements (lines) of the SiO₂ film (dashed lines) and SiN film (solid lines). The films are coated on optically opaque gold with thickness values of 600 nm and 620 nm for SiO₂ and SiN respectively.

It is shown that the simulated absorption spectra are in accord with the measured spectra for the simple 2D geometry within the wavelength range of 3-14 μm . This result confirms the successful optical constant extraction where these constants will be used to simulate more complex geometries. The shoulder occurring in the FTIR measurement of the SiO₂ film is greater than expected probably due to rounding of the extracted parameters and the fitting procedure applied by the FDTD software tool.

Initial 2D simulations for proof of concept are performed with thickness and gap variations for the umbrella layer. Previous studies concerning the low-cost detector geometry had concluded that given a pixel pitch, more infrared power is absorbed when the thickness of the top oxide is increased [46]. The reason is simply the power absorbed per unit volume does not change; however the effective volume of the pixel increases with increasing thickness, hence the total power absorbed increases. With increasing thickness of the pixel, thermal mass increases immensely, as a result, the time constant of the pixel increases.

Consequently, depositing SiN slab on top the low-cost pixel with no geometry would increase the absorption at the expense of higher thermal mass. On the other hand, addition of air gap between two surfaces generate a Fabry-Pérot resonance effect that enhances the absorbed radiation by trapping light in the cavity created between the surfaces [89-92]. Therefore, using air gap as the cavity, one can utilize the resonant effect without sacrificing from the increased thermal mass of the sensor.

The first optimization sweep takes place as the justification of the air gap; thus two dielectric slabs, SiO₂ and SiN in a 2D configuration are simulated with varying gap between them in the range of 0 to 3μm, where 0μm gap means the dielectric slabs are touching. Both dielectric materials (SiO₂ and SiN) are used as the umbrella layer in the exact configuration to justify the benefit the complementary extinction coefficient presented in Figure 2.9. Figure 2.11 sows the schematic representation of the 2D simulation configuration.

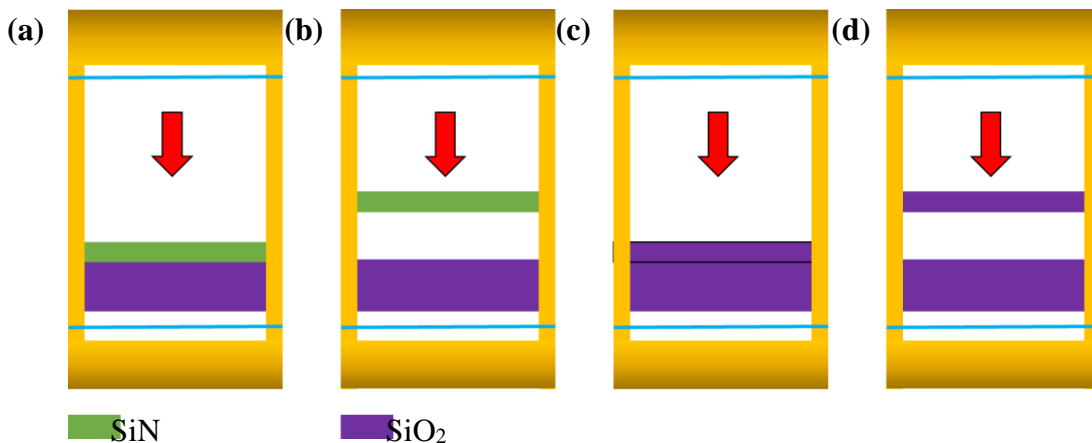


Figure 2.11: Schematic representation of the FDTD simulation setup for the varying air gap size of umbrella layer (SiN and SiO₂) on the SiO₂ low-cost pixel surface. Incident plane wave (red arrow) is placed normal to the surface while the reflection and transmission data monitors (blue lines) are spanned through the unit cell above the light source and underneath the structure respectively.

The boundary differentiation (bottom and top boundaries are PML) and the direction of the incident light (red arrow pointing downwards) are marked as well as the reflection and transmission data monitors (blue lines above the plane wave source and

below the entire structure). Each dielectric layer is simulated as the umbrella layer while the bottom layer is kept as oxide since the detector mainly consists of silicon dioxide deposited in the CMOS line.

The gap is varied with steps of 0.5 μm up to 3 μm totaling 7 spectral lines for each umbrella material simulation setup. The thickness of the bottom SiO_2 layer was simulated to be 1 μm while the umbrella layer, is simulated with a thickness of 0.4 μm as an arbitrary value. Figure 2.12 shows the FDTD simulation results of the varying gap simulation, when the umbrella layer is chosen to be SiO_2 , which is the same as bottom layer as depicted in Figure 2.11 (c), (d).

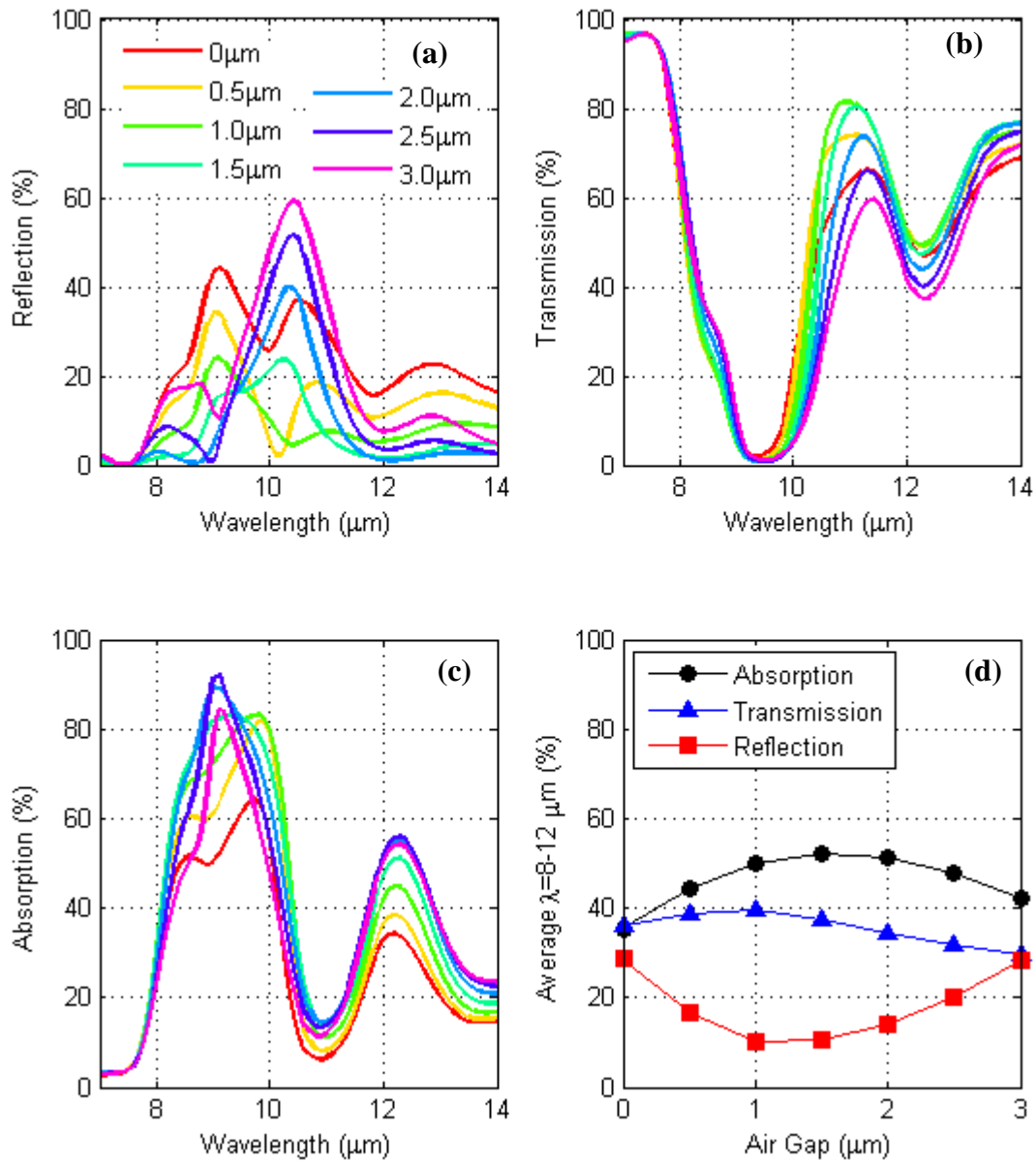


Figure 2.12: 2D FDTD simulation results when both the bottom and the umbrella layers are selected to be SiO₂. The simulated (a) reflection, (b) transmission, (c) absorption, and (d) the average of all three in the LWIR window is calculated and plotted.

It is observed from the figure that if the umbrella material is chosen to be SiO₂, which is the same as the pixel dielectric layer, then increasing gap reaches a global maximum of average absorption for 1.5 μm gap due to significant decrease in the total reflection of the geometry. Further increase in the gap causes reflection to increase again, hence the average absorption drops to values close to where it was for no air gap geometry. Therefore, addition of the gap does increase the absorption in the LWIR band only for 12 % but no significant contribution is performed by the air gap especially in the higher wavelengths of the LWIR window, especially around 11 μm since the extinction coefficient of SiO₂ is almost zero around these wavelength values.

The exact simulation is run, with the umbrella layer is changed to SiN as depicted in Figure 2.11 (a), (b). Figure 2.13 depicts the FDTD simulation results in the same fashion.

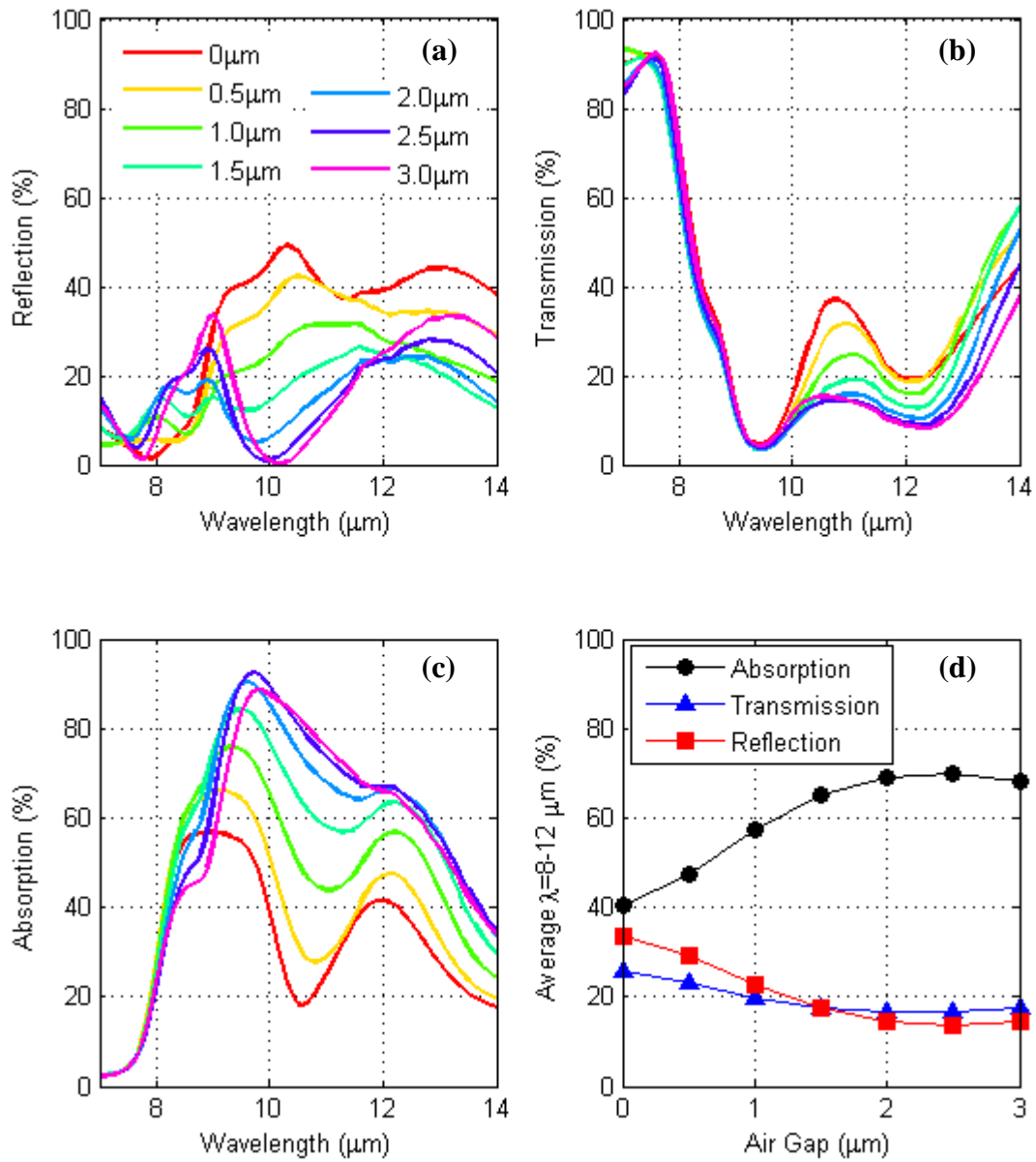


Figure 2.13: 2D FDTD simulation results when the bottom layer is SiO₂ and the umbrella layer is selected to be SiN. The simulated (a) reflection, (b) transmission, (c) absorption, and (d) the average of all three in the LWIR window is calculated and plotted. Note that there is a maximum point in the average absorption when the air gap is around 2.5 μm.

When the umbrella layer is SiN there are substantial differences produced. Firstly, the reflection is significantly reduced around 10 μ m wavelength due to cavity resonance with an average of 30% to 18% in the LWIR window, which is almost 2 fold enhancement. Transmission, in the same manner, is reduced around 10-11 μ m wavelength as seen in the plot. Therefore, the absorption is increased from 40% to 72% in the 8–12 μ m wavelength range. It is worth mentioning that the improvement in the absorption originates from the low reflection and high extinction coefficient of SiN around 11 μ m wavelength. It is also observed that the local maximum of the average absorption is observed when the gap is 2.5 μ m, which corresponds to quarter wavelength of interest (10 μ m) as reflection decrease is the most apparent.

The exact simulation is run with the same configuration but varying pixel slab thicknesses (bottom SiO₂ layer) that is underneath the umbrella layer. The thickness of the bottom slab is changed from 1 μ m to 4 μ m with steps of 1 μ m totaling 4 sets of simulations. Figure 2.13 depicts the spectral and average data for 1 μ m bottom slab and 0.4 μ m umbrella layer. Figure 2.14, Figure 2.15, and Figure 2.16 shows the three sets of plots depicting the results for 2 μ m, 3 μ m, and 4 μ m bottom slab thicknesses respectively.

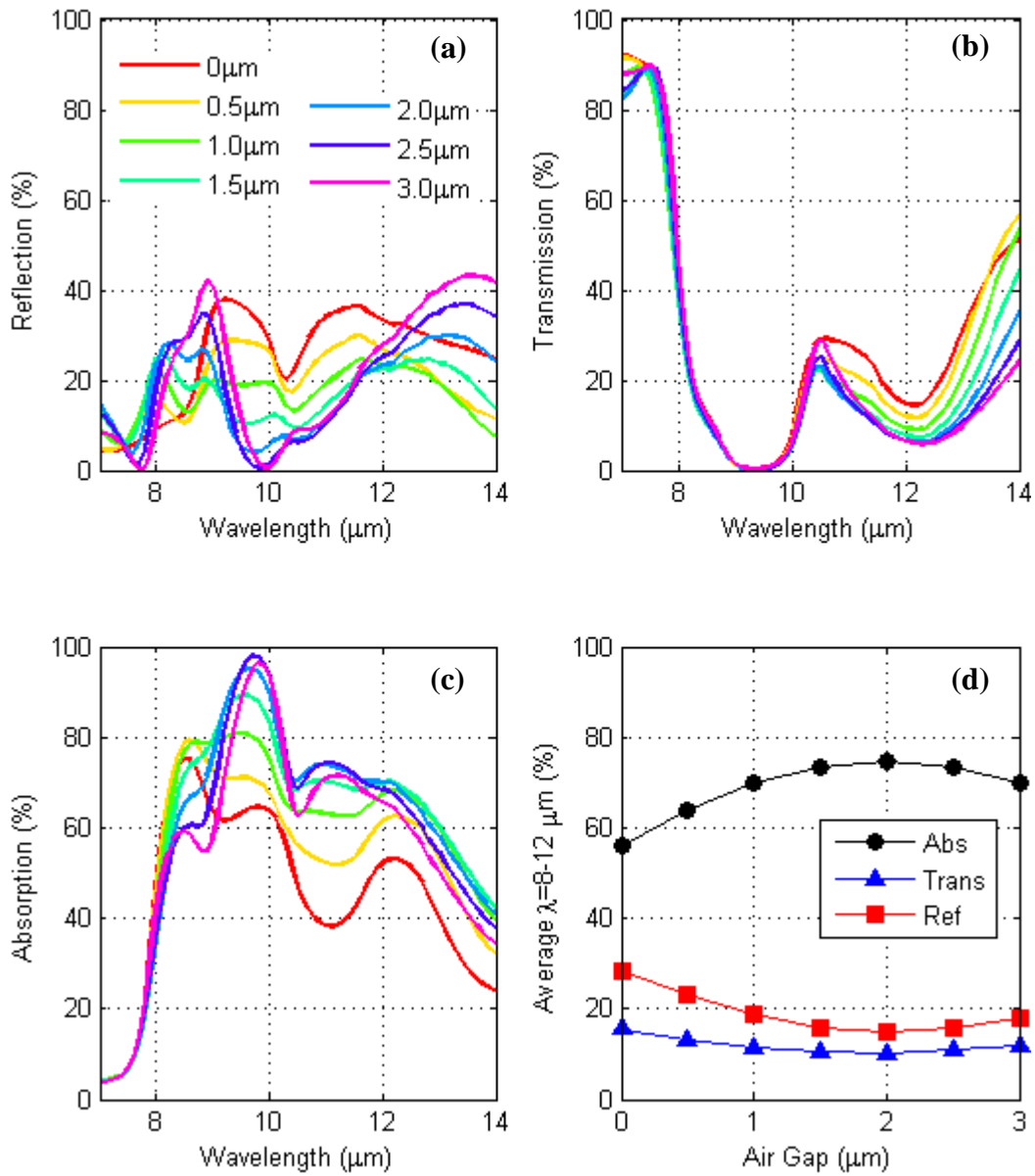


Figure 2.14: 2D FDTD simulation results when the bottom SiO_2 thickness is $2 \mu\text{m}$ and the umbrella layer is selected to be SiN . The simulated (a) reflection, (b) transmission, (c) absorption, and (d) the average of all three in the LWIR window is calculated and plotted.

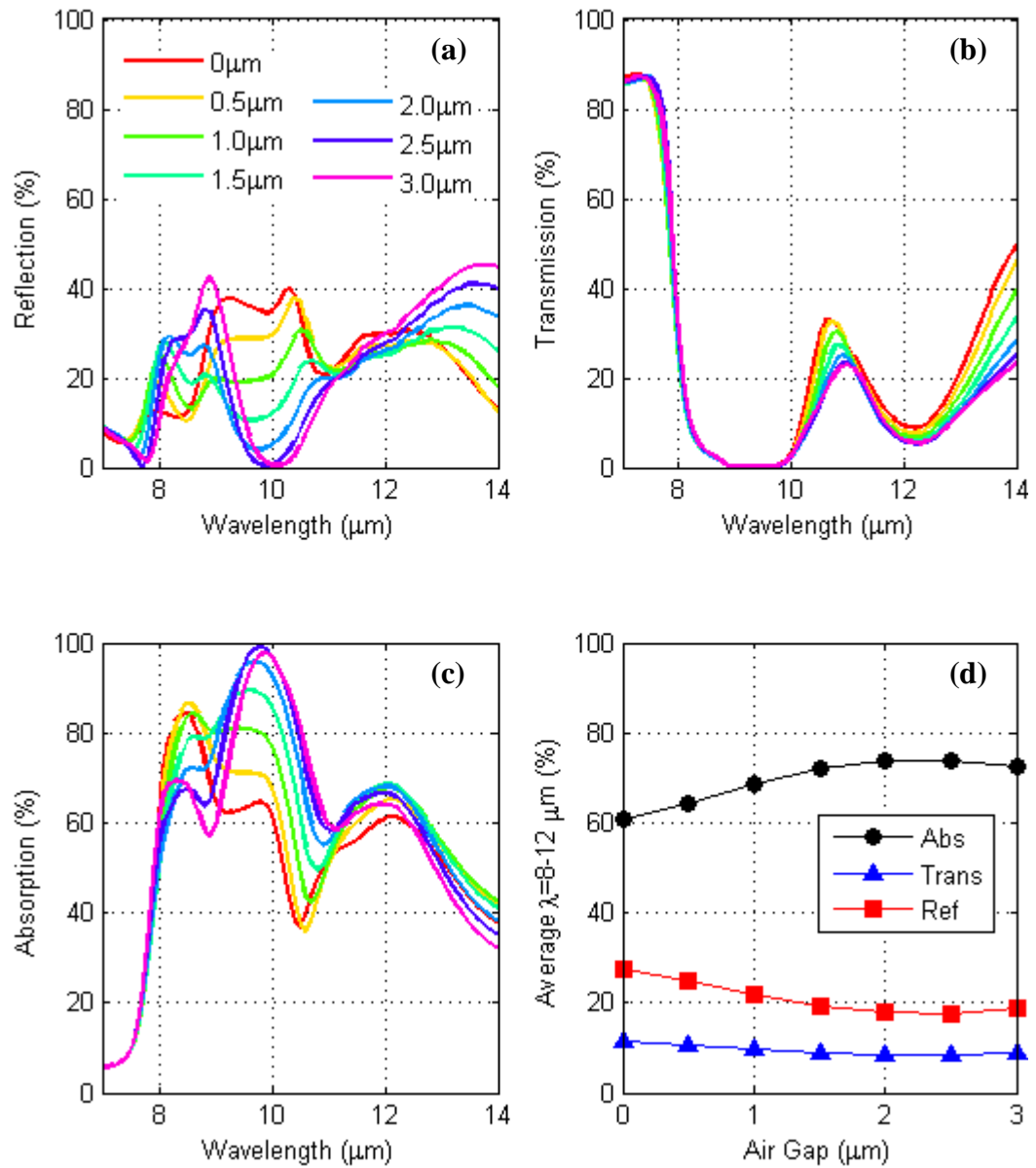


Figure 2.15: 2D FDTD simulation results when the bottom SiO_2 thickness is 3 μm and the umbrella layer is selected to be SiN . The simulated (a) reflection, (b) transmission, (c) absorption, and (d) the average of all three in the LWIR window is calculated and plotted.

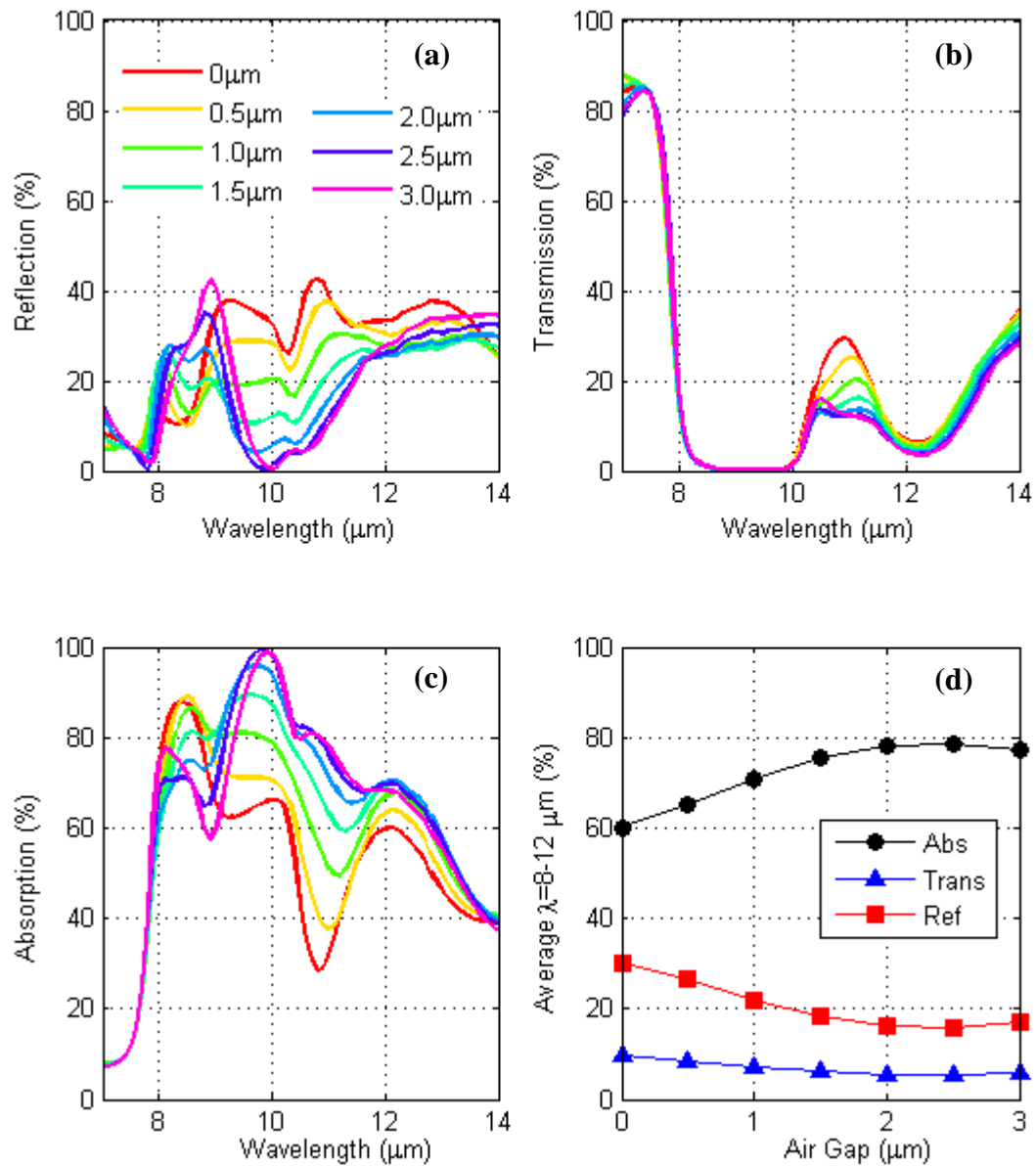


Figure 2.16: 2D FDTD simulation results when the bottom SiO₂ thickness is 4 μm and the umbrella layer is selected to be SiN. The simulated (a) reflection, (b) transmission, (c) absorption, and (d) the average of all three in the LWIR window is calculated and plotted.

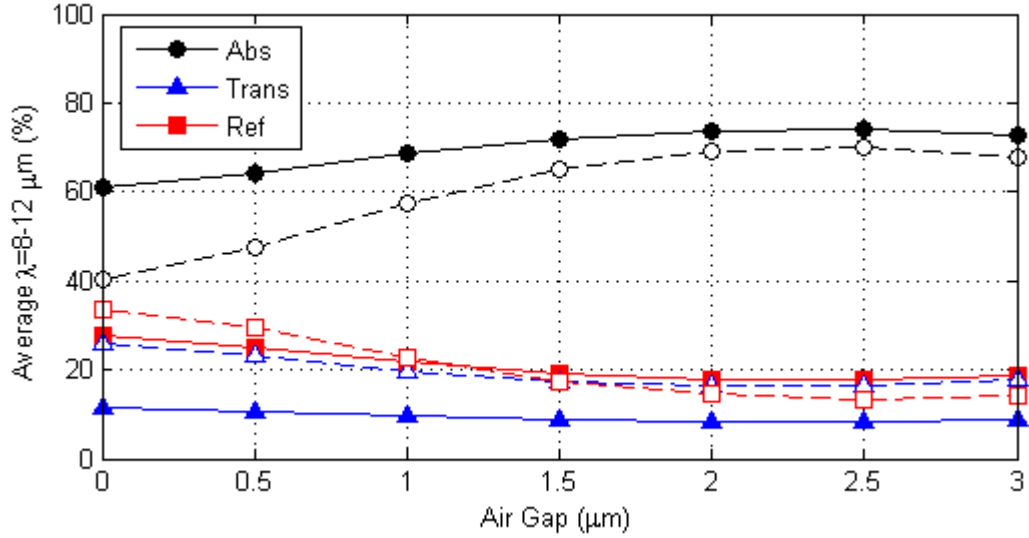


Figure 2.17: Average absorption, transmission, and reflection plots calculated in LWIR window of SiN umbrella layer with 1 μm bottom SiO₂ layer (color-filled markers with solid lines) compared with the averages calculated in LWIR window of SiN umbrella layer with 3 μm bottom SiO₂ layer (white-filled markers with dashed lines).

It is observed that as the thickness of the bottom SiO₂ layer is increased, there is less difference between the total absorbed power before and after umbrella integration since the thicker SiO₂ layer already absorbs more even without umbrella layer. On the contrary, the thicker SiO₂ layer results in notable thermal time constant increase. Therefore, it is conceivable to keep the bottom pixel layer as thin as possible and integrate a high fill factor structure to obtain the same improvement without sacrificing from the thermal mass increase.

Another 2D simulation sweep has been executed using the same geometry and varying gap configuration. This sweep, however, includes varying umbrella layer thickness instead of varying bottom layer thickness. Five different umbrella layer thickness values are used starting from 0.2 μm to 1.0 μm with steps of 0.2 μm . While varying the umbrella thickness, the bottom slab thickness is kept constant at 2 μm . This configuration, also different from the preceding simulations, comprise a metal boundary condition on the bottom (expressed with light blue color) that reflects the entire intensity it encounters with regardless of the wavelength of the light. Reflection

data, $R(\lambda)$, are collected from the monitor placed behind the IR plane wave source; since there is no transmission spectral absorption is calculated as $1 - R(\lambda)$. Figure 2.18 shows the schematic representation of the 2D simulation setup with noted boundary conditions and relative geometric details.

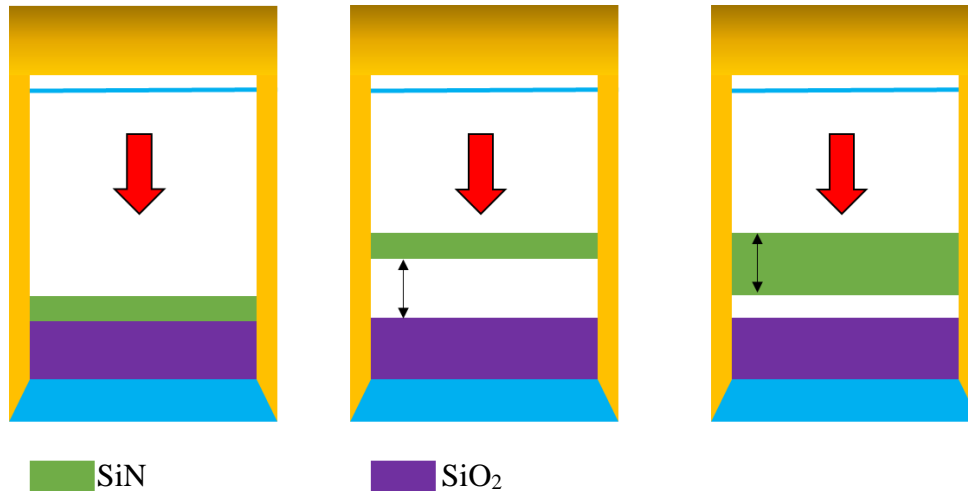


Figure 2.18: Schematic view of the 2D FDTD simulation run with varying gap between the bottom slab and the umbrella, as well as varying umbrella thickness. Note that the bottom boundary condition is chosen to be metal, meaning that it will reflect the incoming radiation at the boundary fully, regardless of the wavelength.

Instead of depicting all the spectral results, the average absorption in the $8 - 12 \mu\text{m}$ wavelength is calculated and represented as data points. For each distinct air gap value, five different thickness umbrella simulated average absorption is calculated and plotted as the independent variable as seen in Figure 2.19.

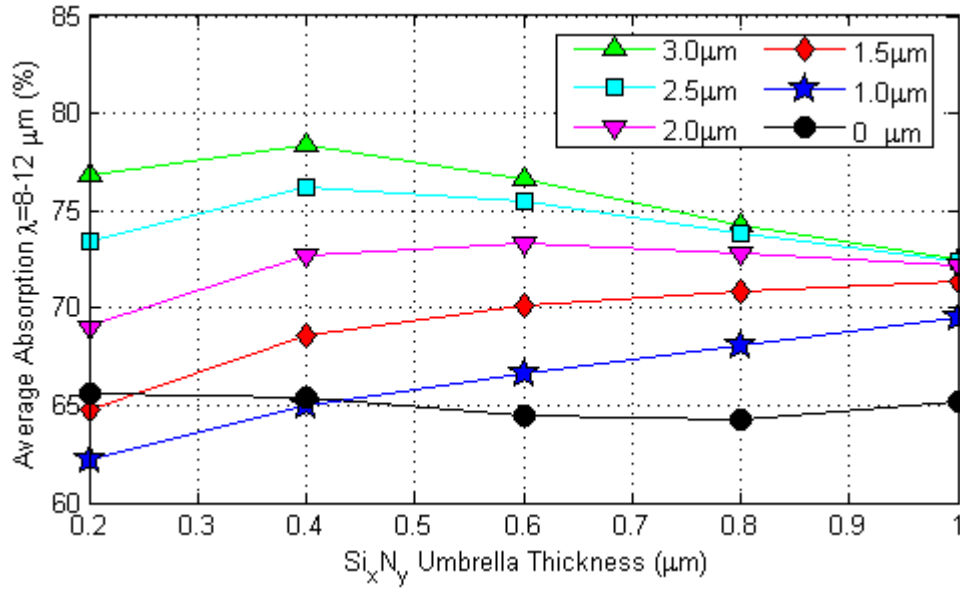


Figure 2.19: 2D FDTD simulation results of varying gap and thickness of the SiN umbrella layer on top of 2 μm SiO₂ pixel layer.

As a summary of the section hitherto, SiN has proven to be the better umbrella material compared to SiO₂ in optical domain as well as the mechanical domain. Although the previous 2D simulations were performed with no complex geometries, the configuration assumes either no reflection apart from the material surfaces, or no transmission due to metal boundary condition as shown in Figure 2.18.

In simple form, it is conceptually easy to demonstrate one dimensional effects such as thickness, or gap size in the vertical dimension. However, other parameters, as well as the single dimension parameters may be affected by the specific geometry. Thus, 3D simulations are performed to observe the effect of additional umbrella layer on a low-cost pixel geometry as demonstrated in the next section considering merely SiN as the umbrella layer.

2.2.3. 3D FDTD Simulations of low-cost Pixel Geometries

The 3D models of the low-cost pixels are established with simplified geometries. Figure 2.20 depicts the geometry and provides the size information of the 50- μm and the 70- μm low-cost pixels. Thickness of the frame and the pixel body (t_1) is modeled

as $4\ \mu\text{m}$ while the arm thickness (t_2) is $2\ \mu\text{m}$ while the Metal-1 layer (m) has a thickness of $0.72\ \mu\text{m}$ for both $50\text{-}\mu\text{m}$ and $70\text{-}\mu\text{m}$ pixels. The lateral dimensions of the pixels are defined as period (p) $50\text{-}\mu\text{m}$ and $70\text{-}\mu\text{m}$ for the pixels corresponding to the pitch. The active area, pixel body (b), is modeled as $34\ \mu\text{m}$ and $42\ \mu\text{m}$ for $50\text{-}\mu\text{m}$ and $70\text{-}\mu\text{m}$ low-cost pixels respectively while the thickness of the each silicon dioxide block adds up to a thickness of $4\ \mu\text{m}$ as detailed design step in a SOI-CMOS line is described in [48]

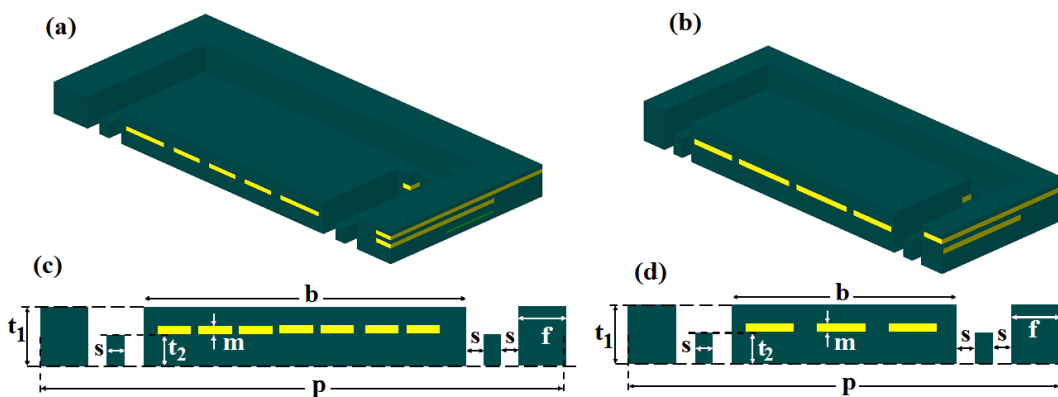


Figure 2.20: 3D model of low cost pixels (a) $70\text{-}\mu\text{m}$ pixel perspective view, (b) $50\text{-}\mu\text{m}$ pixel perspective view. Cross-sectional views of the (c) $70\text{-}\mu\text{m}$ pixel and (d) $50\text{-}\mu\text{m}$ are presented along with denoted dimension information.

The same simulation software is used to compute the 3D model of the $50\text{-}\mu\text{m}$ and $70\text{-}\mu\text{m}$ low-cost pixels. Fundamental assumptions that construct the boundary condition necessities were duplicated in the 3D simulation models as well. Figure 2.21 depicts the snapshot of the simulation software with the model of $50\text{-}\mu\text{m}$ low-cost pixel. The top and the bottom boundary conditions are selected as PML as explained before. The Metal-1 layer acts like a reflector although it does not cover the entire unit cell.

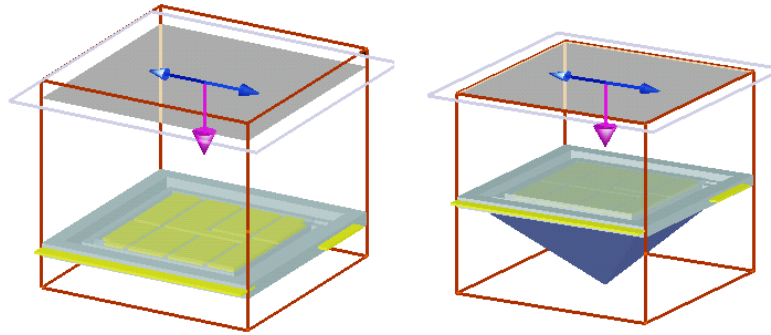


Figure 2.21: Snapshot of the 50- μm low-cost pixel 3D model that is used in the FDTD solver software where in (a) the inverted pyramid effect of the TMAH etching is not accounted for while in (b) the inverted pyramid surface is added. Only the oxide layers and Metal-1 layer is modeled for both simulations.

The same model as shown in Figure 2.21 is constructed with inverted pyramid surfaces of silicon. The result of the two simulations are compared in Figure 2.22.

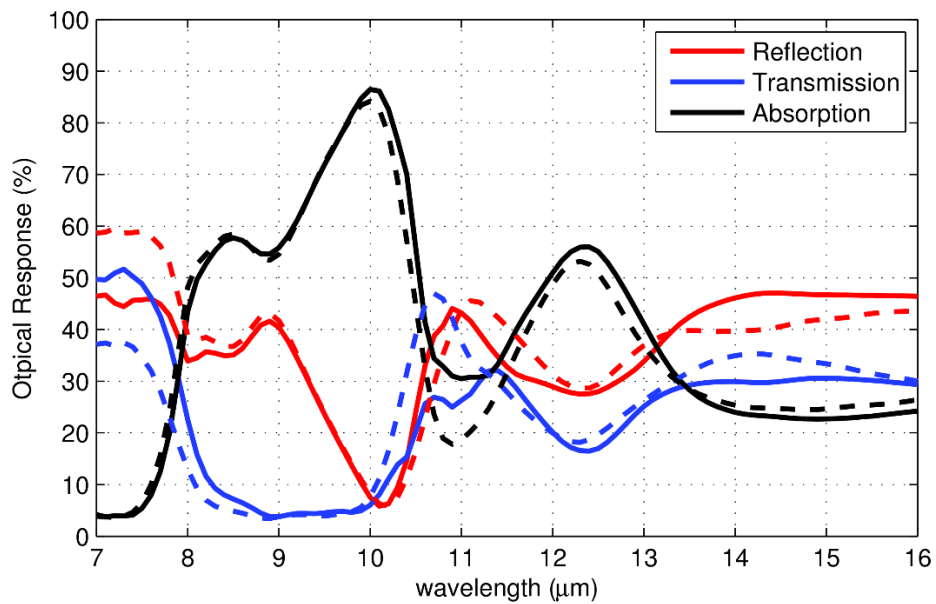


Figure 2.22: Optical response comparison of the 50- μm low-cost pixel. Note that the solid lines represent the added inverted pyramid surface as shown in Figure 2.21 (b) while the dashed lines represent the simulation results correspond the results obtained without the inverted pyramid effect as seen in Figure 2.21 (a).

As seen in Figure 2.22, it is worth mentioning that the addition of inverted pyramid shape increases the computational load remarkably since the mesh number increases with cubic relation related to the size increased of the simulation window. Conveniently, the optical response does not change significantly while excluding the inverted pyramid; thus the following simulations will be performed without the inverted pyramid geometry.

In the first simulation set, 50- μm pixels are added umbrella layers with anchors of 4 square openings. Each square opening has width of 5 μm . The thickness of the umbrella is varied from 200nm to 800nm with steps of 200nm for each simulation. Figure 2.23 shows the snapshot of the simulated low-cost geometry with the added umbrella structure atop.

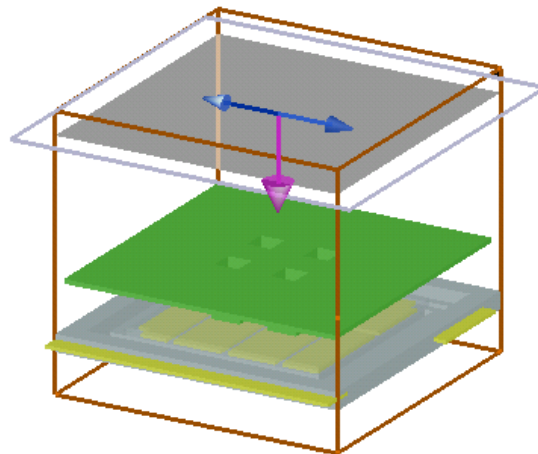


Figure 2.23: Snapshot of the simulated 50- μm low-cost pixel including the umbrella structure that spans 48 μm throughout the unit cell; standing on the pixel with 4 square posts with 5 μm square openings.

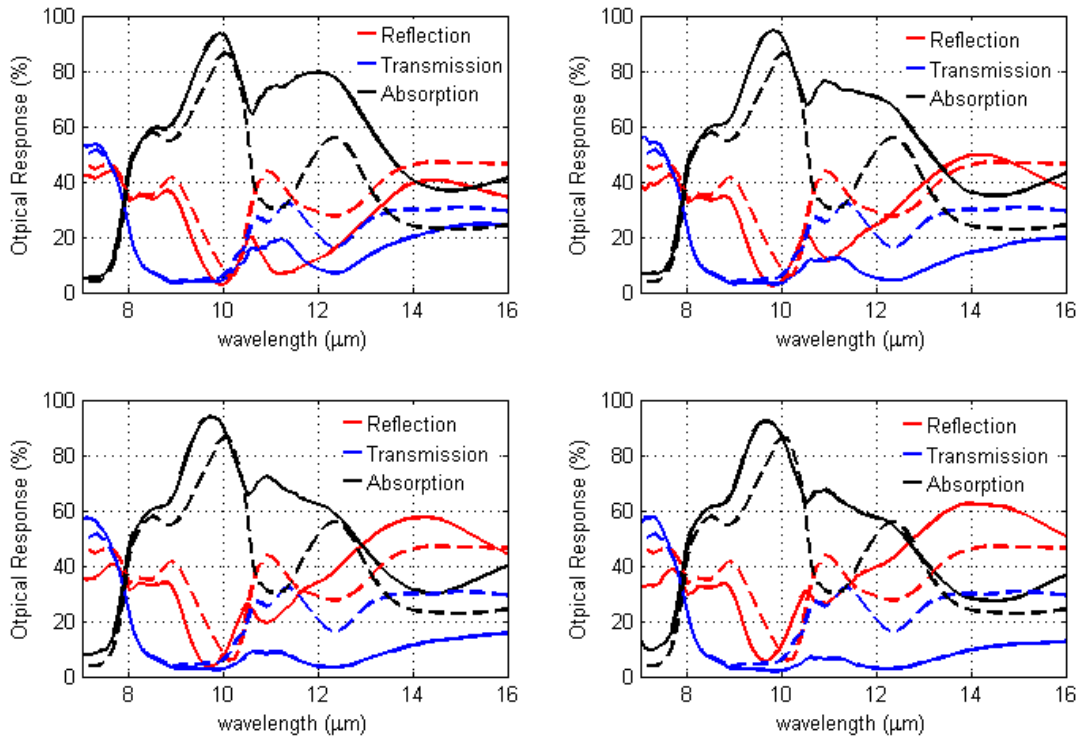


Figure 2.24: Simulated absorption, reflection, and transmission plots of the 50- μm low-cost pixel with various umbrella structure having thickness values of (a) 200 nm, (b) 400 nm, (c) 600 nm, and (d) 800 nm. The dashed lines on each plot is the simulated spectra of the same pixel geometry with no umbrella structure integrated.

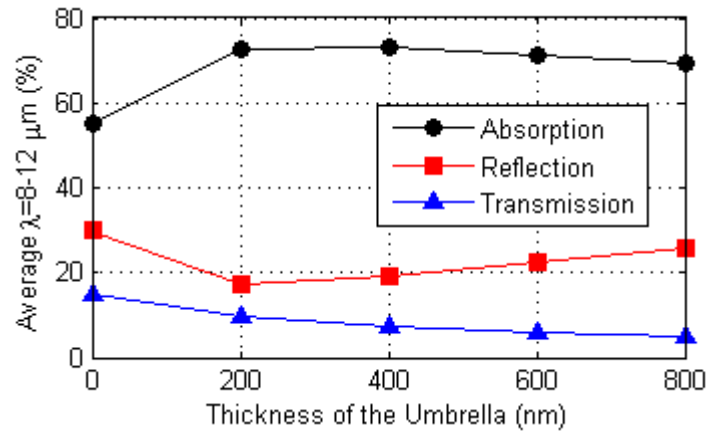


Figure 2.25: Computed average optical response of the 50- μm low-cost pixel with and without umbrella structures while varying the umbrella layer thickness in the LWIR window.

It is concluded that around wavelengths of 10–12 μm , absorption is improved due to addition of the umbrella layer. Averages of absorption, transmission, and reflection are calculated in the LWIR window and plotted in Figure 2.25.

While the 50- μm low-cost pixel absorbs 55% of the incoming radiation, with 400 nm thick and 48 μm wide SiN umbrella structure the average absorption is increased to 73%. Although FDTD simulation results approximates the power absorbed by the radiation; the optical response is obtained from the entire geometry while the temperature sensitive part of the detector is the pixel body exclusively. Although it is computationally possible to calculate only the power absorbed by an arbitrary shape in the simulation, considering the unit cell size of the specific case, the computational load is beyond realistic levels. Therefore, the same simulation arrangement is used in the FDTD solver to simulate only the pixel body in the same unit cell size (meaning, the arm and the frame structures are deleted), including varying umbrella layer thickness values. For the 50 μm pixel, the pixel body comprises the 34 μm x 34 μm square area with the thickness value provided as seen in Figure 2.20.

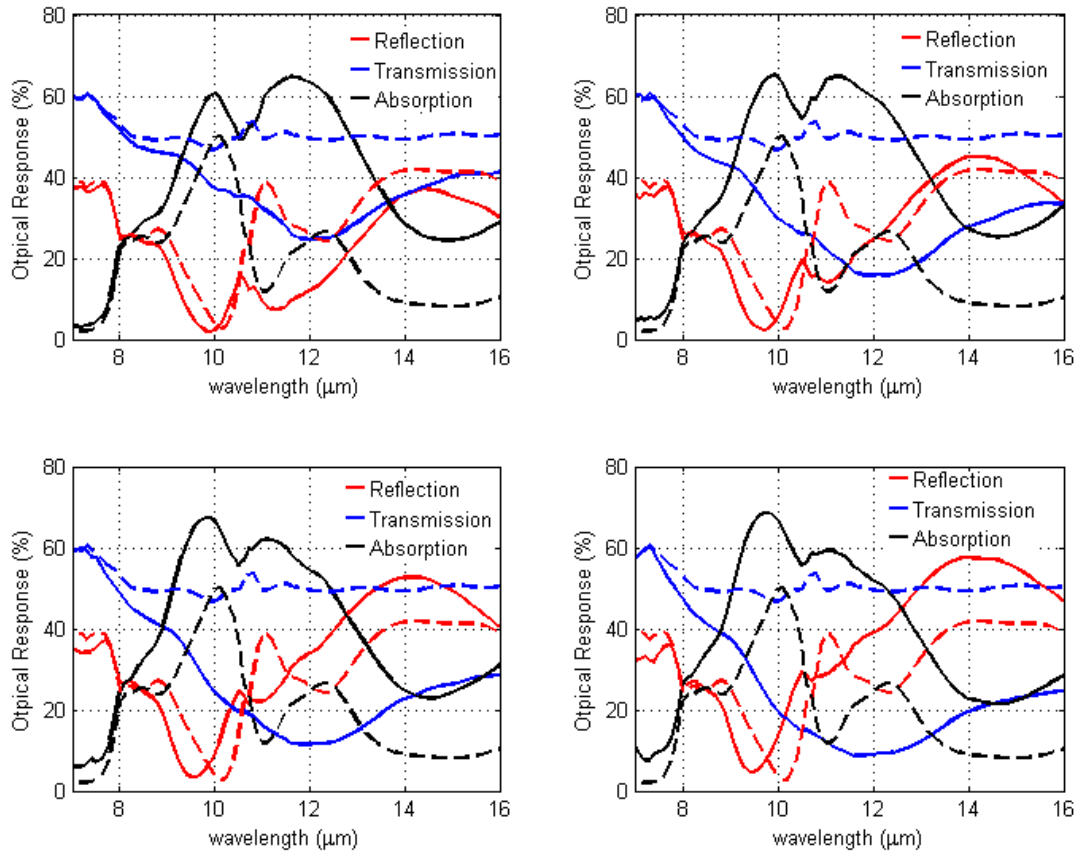


Figure 2.26: Simulated absorption, reflection, and transmission plots of the 50- μm low-cost pixel having only the pixel body with various umbrella thickness values of (a) 200 nm, (b) 400 nm, (c) 600 nm, and (d) 800 nm. The dashed lines on each plot is the simulated spectra of the same pixel geometry with no umbrella structure integrated.

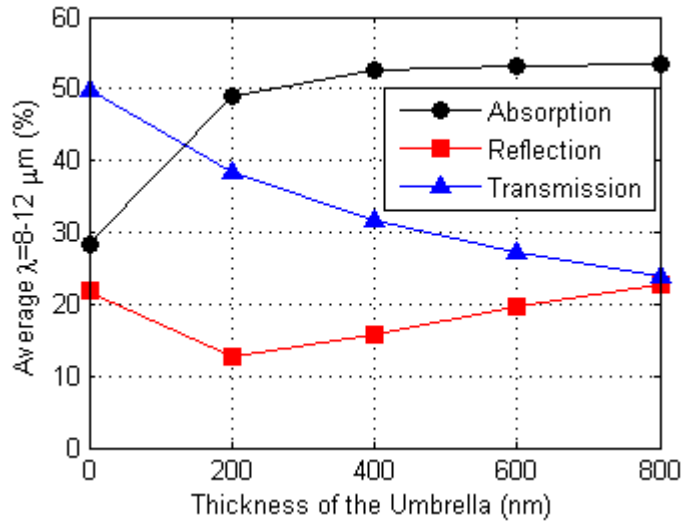


Figure 2.27: Computed average optical response of the 50- μm low-cost pixel consisting of only the pixel body ($34\ \mu\text{m} \times 34\ \mu\text{m}$) with and without umbrella structures while varying the umbrella layer thickness in the LWIR window.

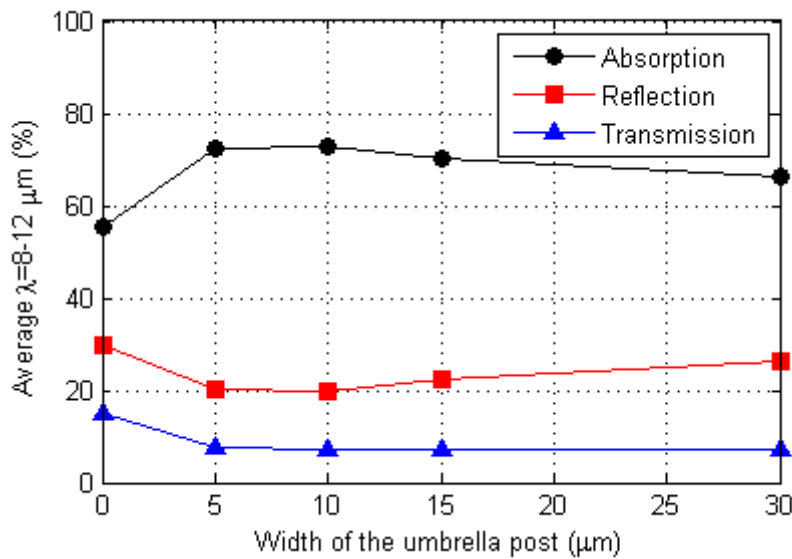


Figure 2.28: Computed average optical response of the 50- μm low-cost pixel with varying the 0.4- μm thick umbrella post size that is shaped square. 0 μm width means there is no umbrella structure at all. Note the decrease in absorption as the post width comprises 78 % of the pixel body.

It is observable in Figure 2.27 that with the addition of the umbrella structure the average absorption in the region of interest increases from 29% to 50% and above with varying umbrella thickness values.

Finally, a set of umbrella post size simulations are run on a 50- μm pixel geometry. One square post is used to support a 0.4 μm thick SiN umbrella on the low-cost pixel with 34 μm x 34 μm body. The width of the square post is changed from 5 μm to 30 μm . The resulting plots are calculated to obtain the average absorption, reflection, and transmission in the LWIR range as presented in Figure 2.28. It is shown that as the square width increases on the pixel body, there is less area for the cavity resonance resulting in lower absorption due to higher reflection.

In summary, 2D geometrical simulations provide a good starting point to comprehend the optical behavior of layer stacks. However, other geometry specific effects are computed using 3D simulation setups. Within the realistic computational needs, the 50- μm pixels are simulated under simplified arrangements. It is concluded that addition of the air gap generates a cavity resonance that enhances the power absorbed by the entire structure. Although Figure 2.25 and Figure 2.27 provide results that are not perfectly in accord; it is evident that the addition of the umbrella structure within surface micromachining dimension boundaries will improve the efficiency of the detector. At a simpler level, the fill factor of the 50- μm pixel is increased from 46% to 92% while the fill factor of the 70- μm pixel is increased from 36% to 94%. Considering the thicknesses of the pixel body and the umbrella structure are significantly different, the contribution with the increased fill factor is not linearly proportional. Enhancement weight of the umbrella structure will be discussed in Chapter 4 in a detailed manner.

2.3. Transient Thermal Simulations

The addition of extra layers to the already existing detector stack will contribute to the thermal mass. The thickness of the material will determine the contribution as well as the span. Although, reported specific heat of the oxides of silicon have lower values compared to nitrides of silicon, the contribution is not significant due to significantly

higher pixel thermal mass [79, 93]. More importantly, the heat generated on the umbrella layer by the infrared absorption will be transferred to the detector body where the temperature sensitive elements are located via the anchors of the umbrella layer. Therefore, the thickness of the deposited umbrella layer is important as it will affect the heat transfer, and in return the overall thermal conductance (G_{th}) of the pixel. It is, however, reported that the thermal conductivity of bulk SiO₂ film and SiN film are comparable [79, 93-98].

While designing low-cost detectors, overall G_{th} is computed through thermal simulations [46, 48], the exact configuration and FEM simulation tool is used to compute the thermal properties of additional umbrella layers. Firstly, the low-cost pixel is constructed using the data provided in the fabrication design kit by the CMOS foundry [46, 48, 60]. The constructed pixel is simulated with the built in material characteristics. Then, umbrella structures with different thickness values are added to the low-cost detector and transient thermal simulation is performed on pixels with varying umbrella thickness values, anchor size and numbers.

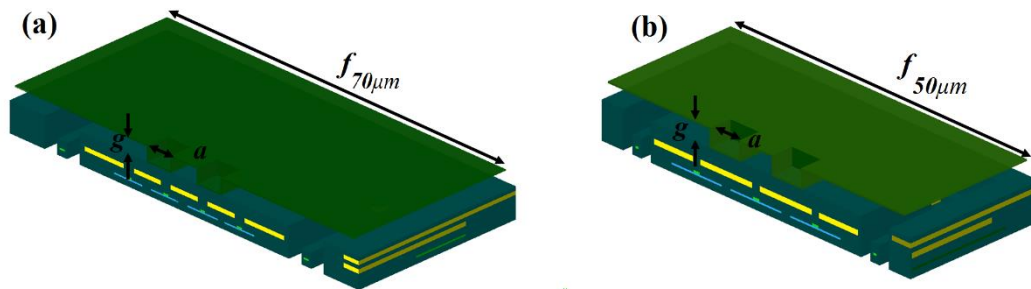


Figure 2.29: Snapshot of the CoventorWare FEM modeling of the (a) 70- μm pixel and (b) 50- μm pixel. Note that the active region silicon layers (light blue) and poly-silicon interconnects (light green) that are embedded in the pixel body are modeled as well.

Transient thermal simulations are run for 400 ms to allow the temperature stabilization for a better data fit performance. Each pixel is given the exact same amount of power as an initial condition, regardless of the presence of umbrella structure or its geometry. All initial temperature values are set to 300 K and transient solver is set to compute the final temperature distribution under given input power. The following transient

temperature plots are constructed by taking the temperature of the sensitive element in the pixel body, not the temperature of the umbrella structure itself.

2.3.1. Thickness simulations

For each pixel structure, the umbrella thickness is swept from 200 nm to 800 nm with intervals of 200 nm while the other parameters are kept constant. As depicted in Figure 2.29, on the 50- μm low-cost detector, the umbrella spans with a frame width of ($f_{50\mu\text{m}}$) 48 μm while the same parameter for 70- μm detector ($f_{70\mu\text{m}}$) is 68 μm . For both structures, the air gap thickness (g) is 2.5 μm and the post width (a) is 5 μm . There are four square posts designed to hold the umbrella structures that are placed symmetrically around the center point of the pixel.

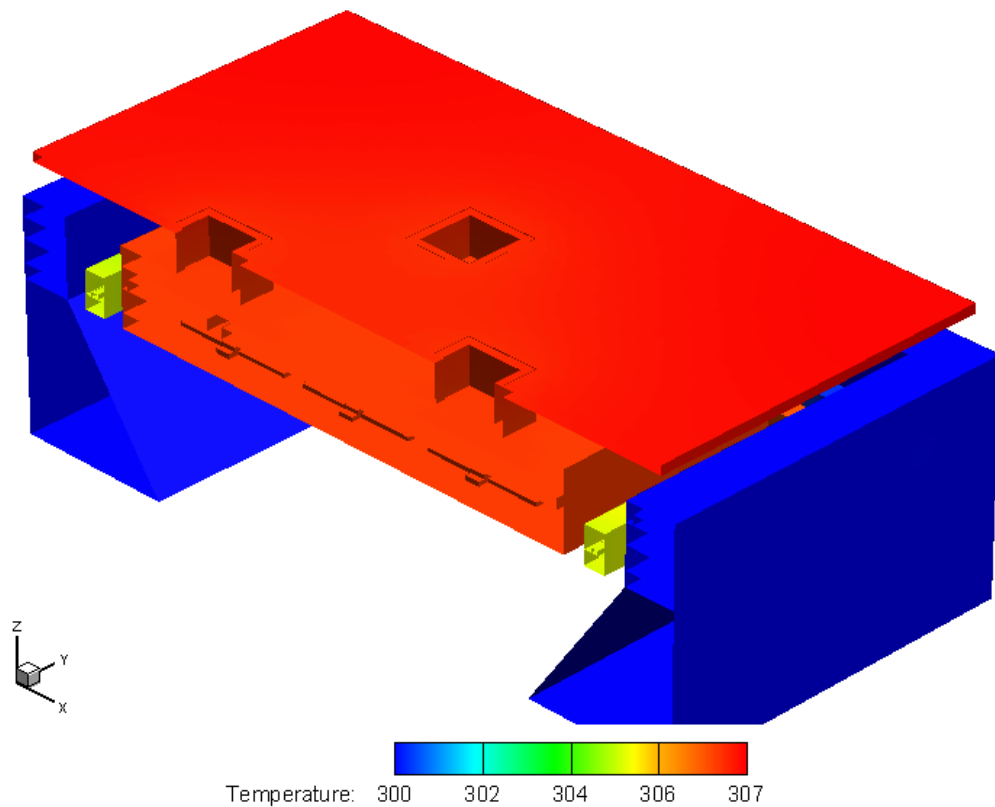


Figure 2.30: Snapshot of the temperature distribution of 50 μm low-cost pixel comprising 4 square posts to support a 600-nm thick SiN umbrella structure.

Figure 2.31 and Figure 2.32 exhibits the plotted data points of 70- μm and 50- μm pixels overlaid with the simulations with no umbrella structures. Results are fitted to an exponential function that is shown in Equation 2.1 in order to extract the time constant and the overall G_{th} of each detector with the addition of umbrella structure, where a signifies the temperature difference between the initial state (300 K) and the steady state, and b represents the time constant of the transient system.

$$T(t) = a (1 - e^{-t/b}) + 300 \quad 2.1$$

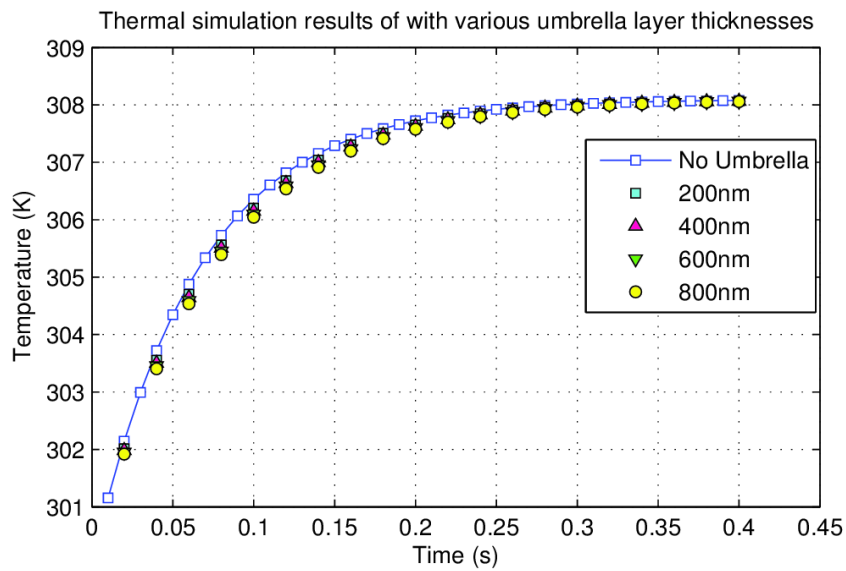


Figure 2.31: Computed transient thermal response of the 70- μm pixel with and without the umbrella structure. It is evident that the addition of umbrella structure with varying thickness values do not change the transient response substantially.

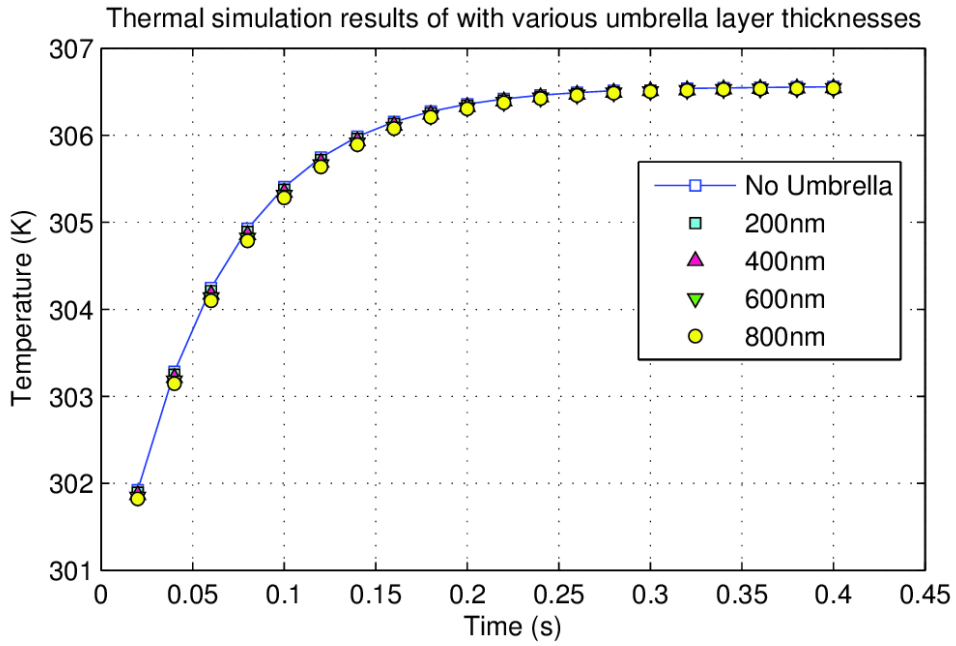


Figure 2.32: Computed transient thermal response of the 50- μm pixel with and without the umbrella structure. It is evident that the addition of umbrella structure with varying thickness values do not change the transient response substantially.

It is concluded that the overall G_{th} of the pixels are not altered with varying the thickness of the umbrella layer. The time constant, on the other hand, exhibits an expected result; that is increasing trend with increasing the thickness of the umbrella. Table 2.1 lists the computed time constant values as a result of the thermal simulations performed on both 50- μm and 70- μm low-cost pixel geometries.

Table 2.1: Extracted time constant data of 70- μm and 50- μm low-cost pixels while including umbrella structures of different thicknesses compared with pixels including no umbrella structure.

	Umbrella Thickness	Time Constant
	(nm)	(ms)
70-μm Low-cost pixel	No Umbrella	65 ± 0.01
	200	69 ± 0.1
	400	70 ± 0.1
	600	71 ± 0.1
	800	73 ± 0.1
50-μm Low-cost pixel	No Umbrella	56 ± 0.01
	200	58 ± 0.1
	400	59 ± 0.1
	600	60 ± 0.1
	800	61 ± 0.1

2.3.2. Anchor variation simulations

The same umbrella geometry is used to test the heat transfer characteristics by changing the number of posts that the umbrella layer is connected to the pixel body. Theoretically, as the number of posts increase, thermal condition rate is increased due to increased contact area. On the other hand, more posts mean less surface area for cavity resonance. Therefore, the post number should be as minimal as possible while providing enough thermal conductance to the pixel body where the temperature sensitive elements are located. Figure 2.33 illustrates the placement of various number of posts for each umbrella structure that is 600 nm thick on a 70 μm pixel pitch (p) with a span (f) of 68 μm and post width (a) of 5 μm . Figure 2.34, shows the average temperature of the sensitive element in the body, plotted against time for each number of posts integrated to the umbrella.

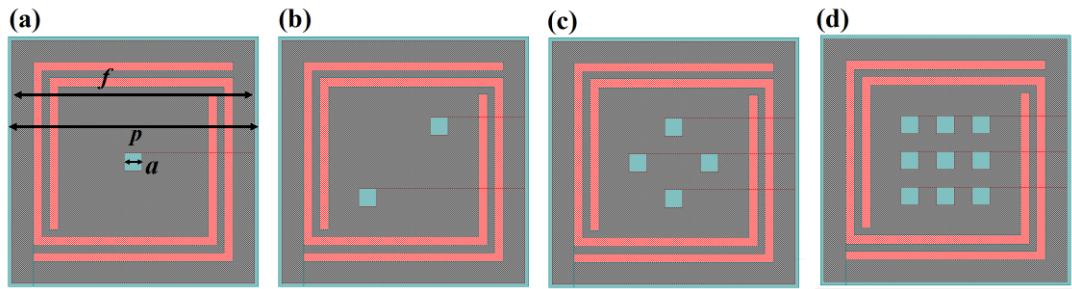


Figure 2.33: GDS model schematic of the 70- μm low-cost pixel and the umbrella structure with varying post numbers. Note that the period (p) of the pixel is 70- μm while the umbrella spans (f) 68 μm standing on a post size (a) of 5 μm .

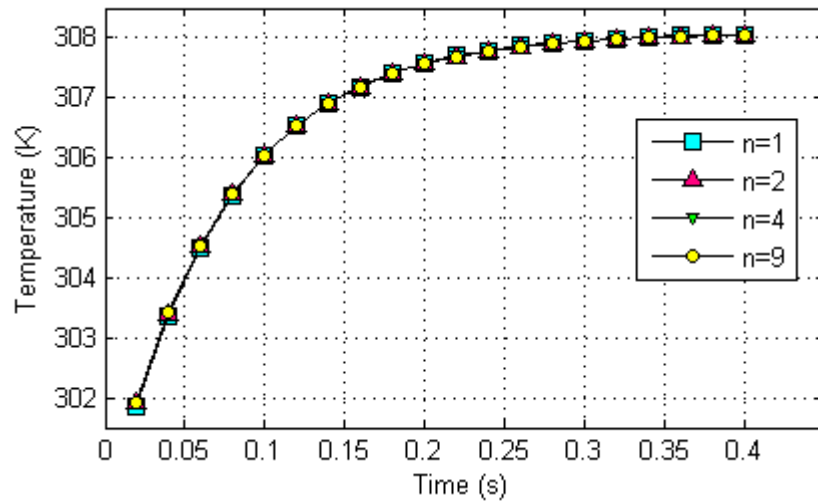


Figure 2.34: Thermal simulation results of the 600 nm thick umbrella structure integrated to the 70- μm low-cost pixel with various post numbers connecting the umbrella to the pixel body. It should be noted that the results of each simulation are almost identical.

Temperature plot of the umbrella structures with increasing number of connecting posts conclude that thermal conduction through one post that is 5 μm wide square is sufficient. Additional posts may be required for mechanical stability as it will be discussed in the fabrication section.

In the same manner, 600 nm thick umbrella structures are also tailored to 50- μm low-cost detectors with a span (f) of 68 μm and anchor size of (a) 5 μm as shown

schematically in Figure 2.33. The computed transient temperature of the sensitive element is plotted for each design in Figure 2.35 for the 50- μm low-cost pixel.

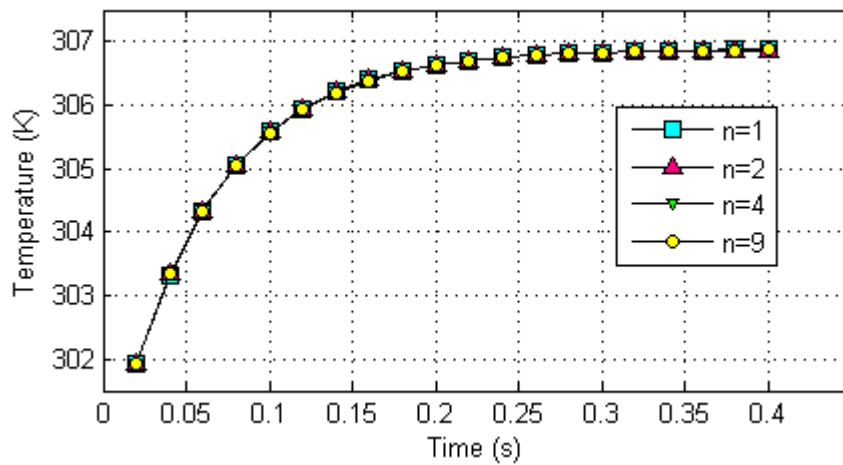


Figure 2.35: Thermal simulation results of the 600 nm thick umbrella structure integrated to the 70- μm low-cost pixel with various post numbers connecting the umbrella to the pixel body. It should be noted that the results of each simulation are almost identical.

In conclusion, the previous section attains that the integrated umbrella layer for both low-cost pixel geometries should have at least 400 nm thickness to contribute significantly to the optical response. By comparing the time constant results of pixels with umbrella structures that in the neighborhood of 400 nm thickness, it is concluded that 600 nm thickness does not increase thermal mass substantially. In addition, considering fabrication necessities where 600-nm thick umbrella layers are required instead of 400-nm thick layers, the performance downgrade is negligible in terms of thermal properties.

It should be considered that the thermal conductivity of SiN is considered to be 1 W/mK which is within the lower bound of the measured values in the literature. Therefore, even with such low thermal conductivity values, it is established that increasing the surface contact of the umbrella by means of number of posts or anchor size does not yield better thermal conduction at the given thickness values.

CHAPTER 3

FABRICATION OF UMBRELLA STRUCTURES

The low-cost detectors that are considered in this study are produced in CMOS foundries while post-CMOS processes were developed in the METU-MEMS Research Center. Utilization of MEMS surface micromachining tools enable the integration of 3D structures on the pre-designed low-cost detectors. Therefore, there are main concerns that forms the fabrication limits. The most fundamental one of them is the CMOS compatibility. Post-CMOS processes that require very high temperature treatments, or chemicals that damage the passivation dielectric or interconnecting metals cannot be used to realize additional geometries on the low-cost detectors. Another important concern emerges from the “low-cost” nature of the detector fabrication as well as the preservation of the modularity of the integrated umbrella structure. Thus, the integrated umbrella structure must retain positive qualities pertaining to the production cost and the ease of fabrication, including a comfortable range of fabrication error tolerance.

This chapter explains the steps taken to realize the designed umbrella structures on 50- μm and 70- μm low-cost detectors. Firstly, series of dummy fabrication optimizations are presented along with the central challenges that are encountered. Then the solution to these challenges are conveyed through juxtaposition also supported by scanning electron microscopy (SEM) images and sketches. Finally, the successful integration of umbrella structures onto 70- μm and 50- μm detector FPAs are demonstrated.

3.1. Dummy fabrication with amorphous-Silicon (a-Si) sacrificial layer

The first realization trials of the umbrella design are performed using dummy structures that are fabricated in one step etching of a silicon wafer. 50- μm and 70- μm pixel geometries are defined identical to the corresponding lateral dimensions of the low-cost pixels. Figure 3.1 shows the schematic of the drawn low-cost pixel while Table 3.1 provides the dimension information for both low-cost detectors. The period of the pixel is denoted as p while the body width is b . The arm width is w_a and the spacing between the body-arm-frame geometry is w_s , which is also symmetric.

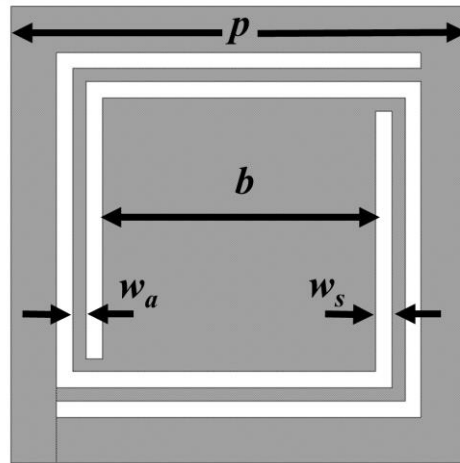
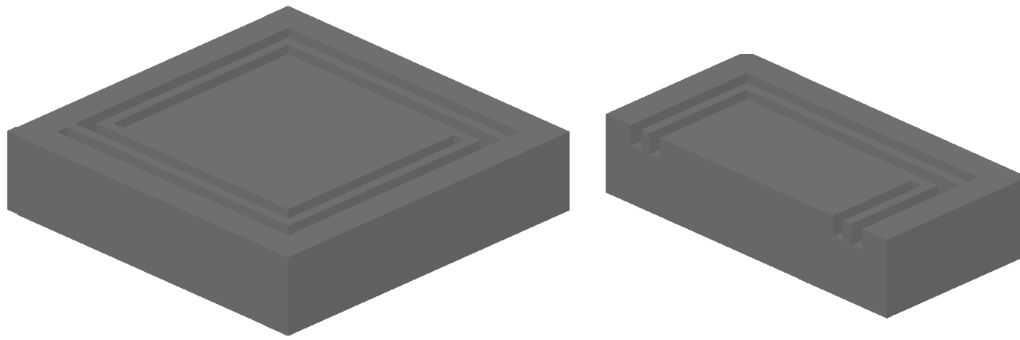


Figure 3.1: Schematic representation of the 2D pattern of low-cost pixel geometry. The period of the pixel is denoted as p while the body width is b . The arm width is w_a and the spacing between the body-arm-frame geometry is w_s , which is also symmetric.

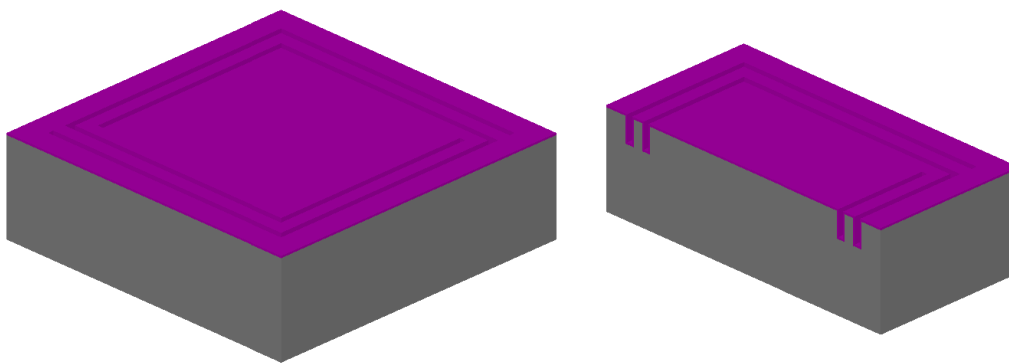
Figure 3.3 shows the full perspective view of the fabrication steps modeled on the FEM modeling software CoventorWare for the 50- μm low-cost pixel. A plane cut view is also included on the right hand side to depict the cross-sectional view of the process steps. It should be noted that the schematic fabrication steps are not modeled to emulate the fabrication imperfections.

Table 3.1: Lateral dimension information provided for the low-cost pixel geometries. These dimensions are used to define the structures in the FEM modeling as well as the lithography of the real structures.

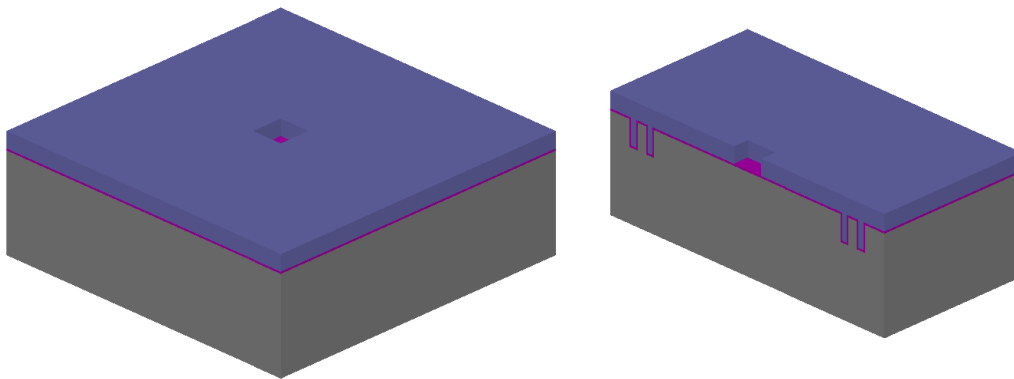
	50-μm Pixel	70-μm Pixel
	(μm)	(μm)
p	50	70
b	34	42
w_a	1.5	2
w_s	1.5	2.5



a) Formation of arms

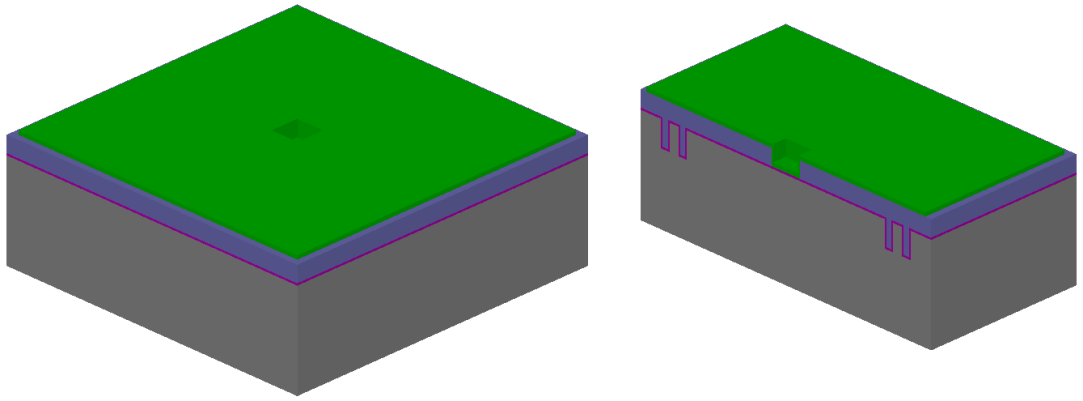


b) Oxide etch stop

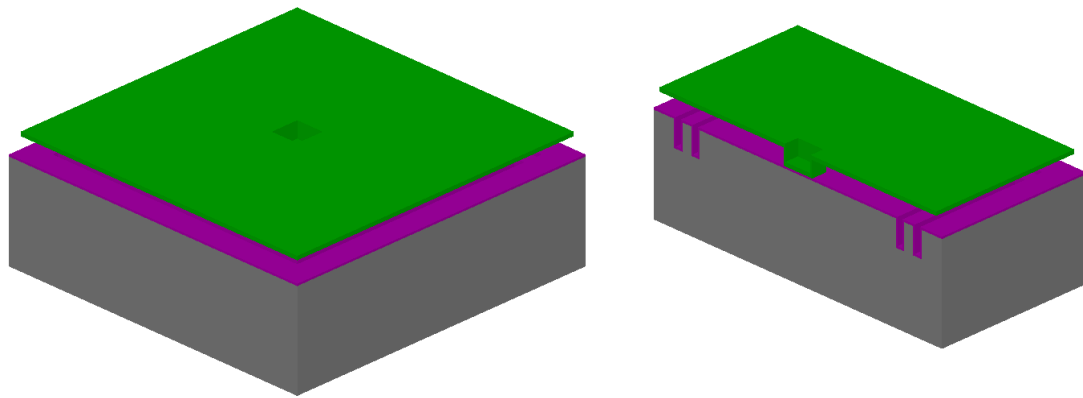


c) Sacrificial layer deposition and patterning

Figure 3.2: Schematic view of the full unit cell as well as the cross-section of the dummy structure fabrication on bare silicon wafer.



d) Umbrella layer deposition and patterning



e) Release of the sacrificial layer

Figure 3.3: Schematic view of the full unit cell as well as the cross-section of the dummy structure fabrication on bare silicon wafer. (continued)

In the first step, the Si wafer is patterned and etched to emulate the low-cost pixel arm structure in deep reactive ion etching (DRIE) tool. A thin SiO₂ layer is deposited to act as an etch stop layer. Since the low-cost detector surface is also CMOS passivation SiO₂, it is an appropriate approach. Then sacrificial layer is deposited (2.5 μm high from the surface) by completely filling the grooves opened in the first step assuming perfectly conformal coating. Then the sacrificial layer (a-Si) is patterned and anchor points are etched until the wafer surface. Following, the umbrella layer (SiN) is deposited with a desired thickness value where the anchor openings act like posts for the deposited layer. Penultimately, the umbrella layer is patterned to separate each one in the array of pixels using dry etching techniques. Finally, the release step is performed using XeF₂ etching system in order to completely remove the a-Si layer.

Realization of arrays of umbrella structures on 50-μm and 70-μm low-cost detectors follow the same procedure in principle. However, the resulting fabrication imperfections are inevitable as observed in the SEM images –although these imperfections do not prevent the desired structure to be built. The etching of pixel geometry on Si wafer results in wider arm spacing (w_s) and narrow arm widths (w_a) than designed.

Optimization of each process step is achieved though simple trials. Although forming the arm trenches is trivial in MEMS domain, completely filling the trenches without utilizing conformal coating technologies is problematic. Figure 3.4 shows the SEM images of 50-μm and 70-μm dummy pixels. The low-cost geometry is simulated on the Si wafer with only one step etching. The arm widths, however, get narrower due to imperfections in the directional etching.

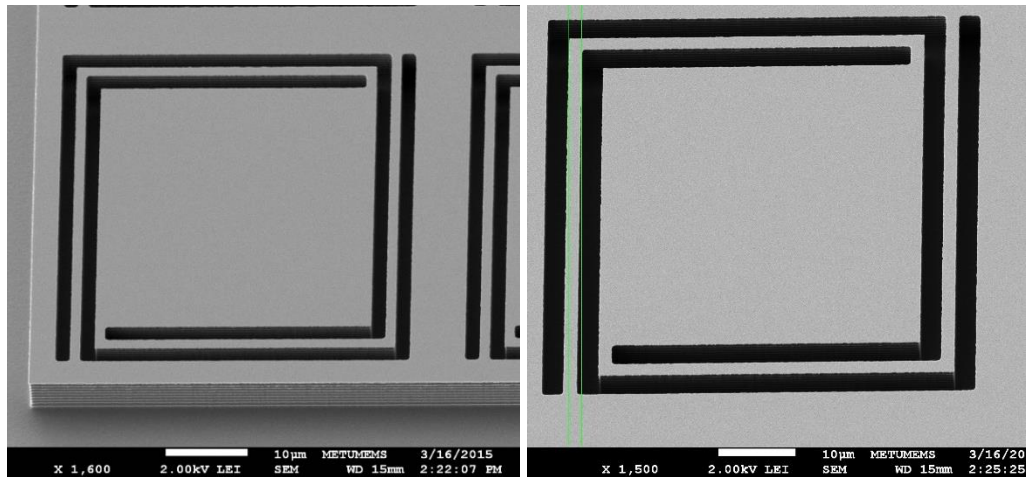


Figure 3.4: SEM images of (a) 50- μm dummy pixel and (b) 70- μm dummy pixel etched in DRIE in one step to form the arm grooves.

Since low pressure chemical vapor deposition (LPCVD) tools cannot be used due to high process temperature ($\sim 800^\circ\text{C}$) needs, PECVD coating profile was observed under various recipes and process duration. Instead of filling the trenches, the spacing between the arms is blocked by non-conformal coating to prevent gas flow into the trenches while depositing the umbrella material. The desired blocking effect is achieved after depositing a-Si layer that is $2.5\ \mu\text{m}$ thick from the pixel surface, which defines the air gap formed underneath the umbrella structure.

Figure 3.5 shows the failed umbrella fabrication due to not being able to block the trenches prior to umbrella material deposition. Thus, the umbrella material is coated along the sidewalls of the trenches preventing the release of the sacrificial layer completely. On the other hand, Figure 3.6 shows effective blocking of the trench openings so that the SiN layer deposited on top does not cover the trenches.

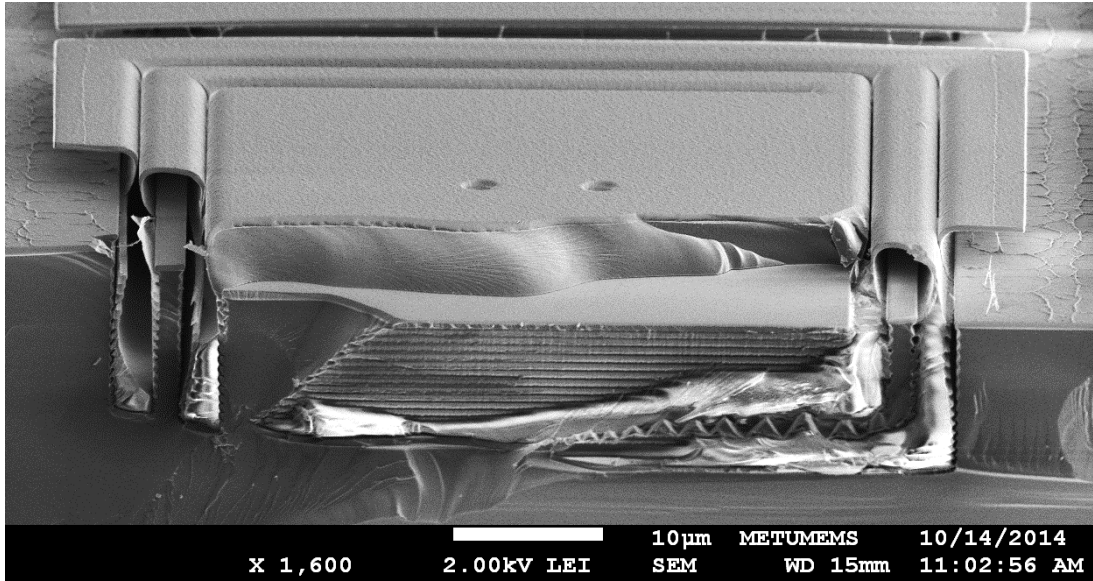


Figure 3.5: SEM image of a 70- μm dummy pixel after the release process. Note, however, that the sacrificial layer underneath pixel body region is not etched since umbrella layer covers the side walls of the arm trenches due to not being able to seal the arm spacing properly.

The umbrella frames are formed with lithography and etched in reactive ion etching (RIE) tool to form independent umbrella structures on each pixel. As observed in Figure 3.6, silicon nitride umbrella layer is etched separating one umbrella structure from the adjacent one.

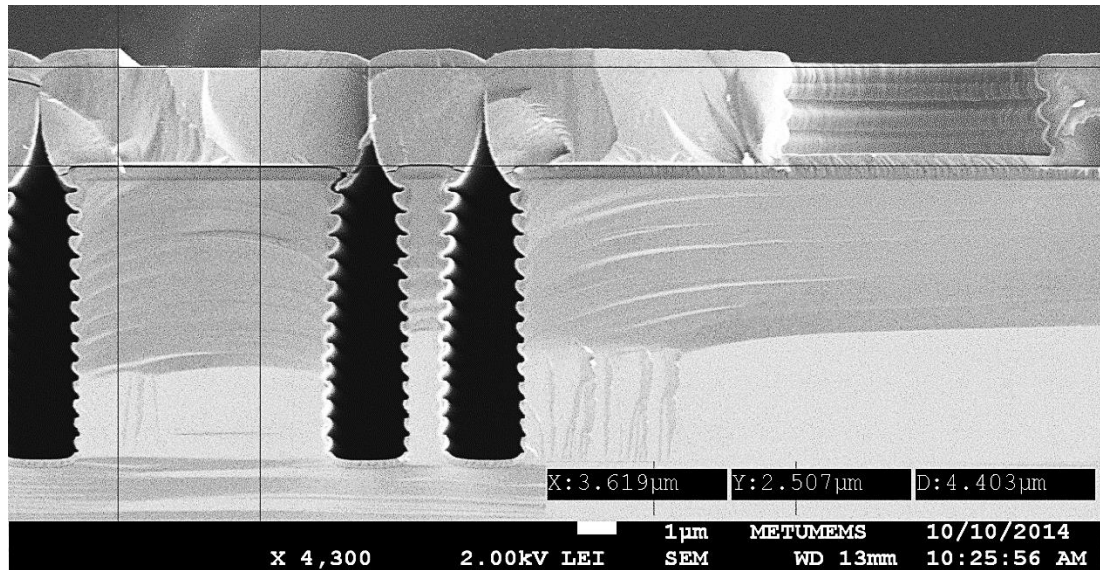


Figure 3.6: SEM image of a 50- μm dummy pixel before release process. Note that the umbrella layer continuously spans above the arm spacing not getting into the trenches. Moreover, the umbrella frames are formed and etched separating each one with a distance of 2.5 μm for this particular dummy structure.

The release procedure is optimized using XeF_2 and varying the dilution ratio of the XeF_2 gas with nitrogen gas (N_2). The etching is performed in pulsed steps of 5 seconds rather than continuous flow in order to protect the silicon nitride umbrella layer. As the final process step, a short (5 s) exposure to vapor HF is preferred to eliminate the oxide residues ensued from the release step. Figure 3.8 shows SEM images of the completed dummy umbrella structures. At the anchor defining step, numerous anchor sizes and different numbers and distributions are experimented to experience the fabrication tolerance of different structures in array format so the FPA format is emulated.

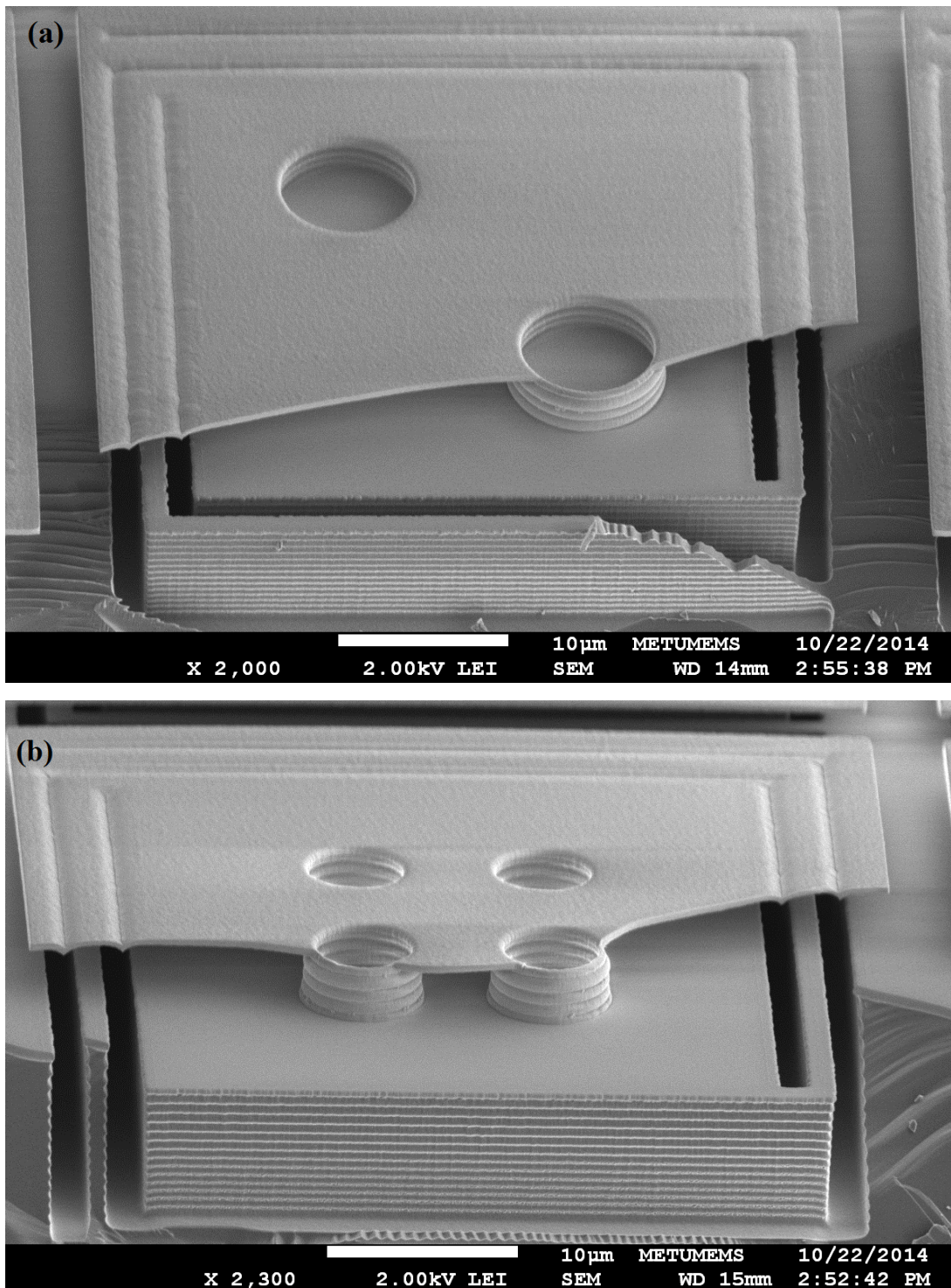


Figure 3.7: SEM images of dummy pixels integrated with 600-nm thick silicon nitride layer umbrella. There are various post size and numbers employed in (a) post diameter is 5 μm with of circular posts, (b) post diameter is 3 μm on four circular posts, and in (c) post size is 30 μm which is a single square resting on the pixel body.

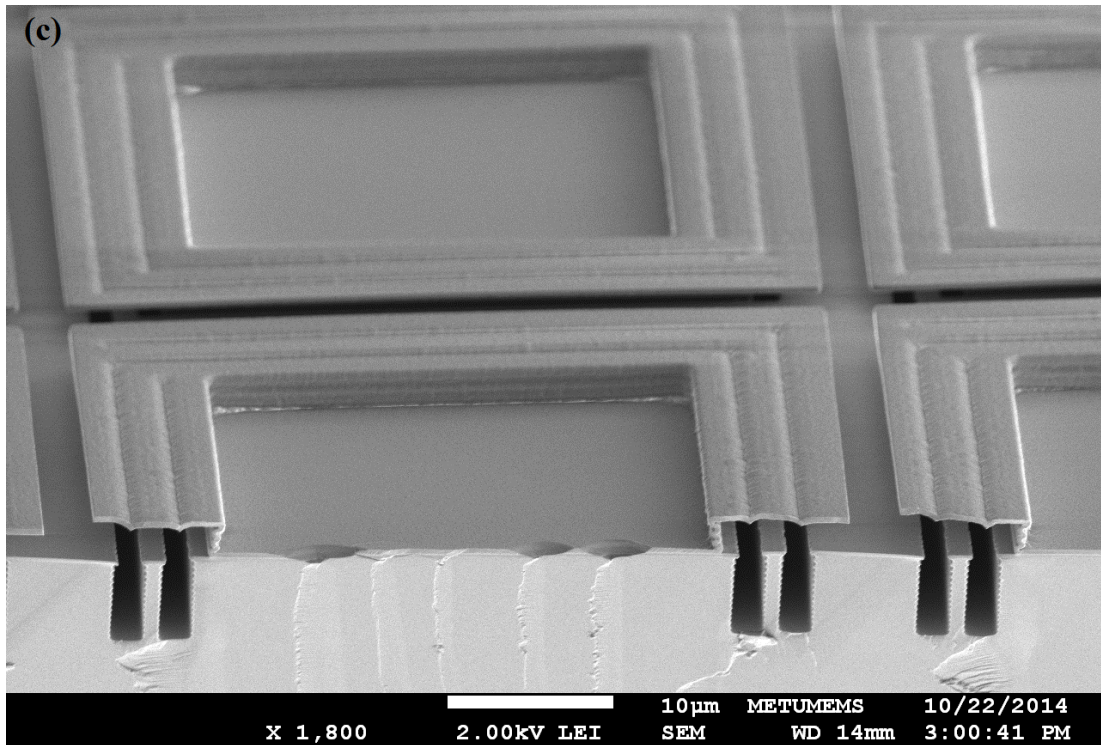


Figure 3.8: SEM images of dummy pixels integrated with 600-nm thick silicon nitride layer umbrella. There are various post size and numbers employed in (a) post diameter is $5\ \mu\text{m}$ with of circular posts, (b) post diameter is $3\ \mu\text{m}$ on four circular posts, and in (c) post size is $30\ \mu\text{m}$ which is a single square resting on the pixel body. (continued)

3.2. Die level CMOS with a-Si sacrificial layer

Following the successful dummy fabrication of umbrella structures, CMOS dies with detector periodicities of $70\ \mu\text{m}$ and $50\ \mu\text{m}$ are deposited a-Si layer in the exact PECVD tool, using the same recipe. However, different arm topology of the low-cost pixels, the lower height of the arm relative to the pixel wall and the pixel body, precludes blocking of the trenches between the arms.

Two fundamental approaches are investigated towards solving the deposition problem. The conformality of the coating is adjusted by changing the process pressure in the chamber. Although the pressure is decreased to obtain more conformal coating as to fill the trenches, the efficacy of this method is observed to be unproductive. The second approach is to increase the process pressure to obtain more non-conformal coating, where the blocking of the arm spacing gets more probable without increasing

the height of the sacrificial layer from the surface too much. The latter approach yields similar results; hence the sealing of arms is not possible unless significant amount of a-Si is deposited on the pixels.

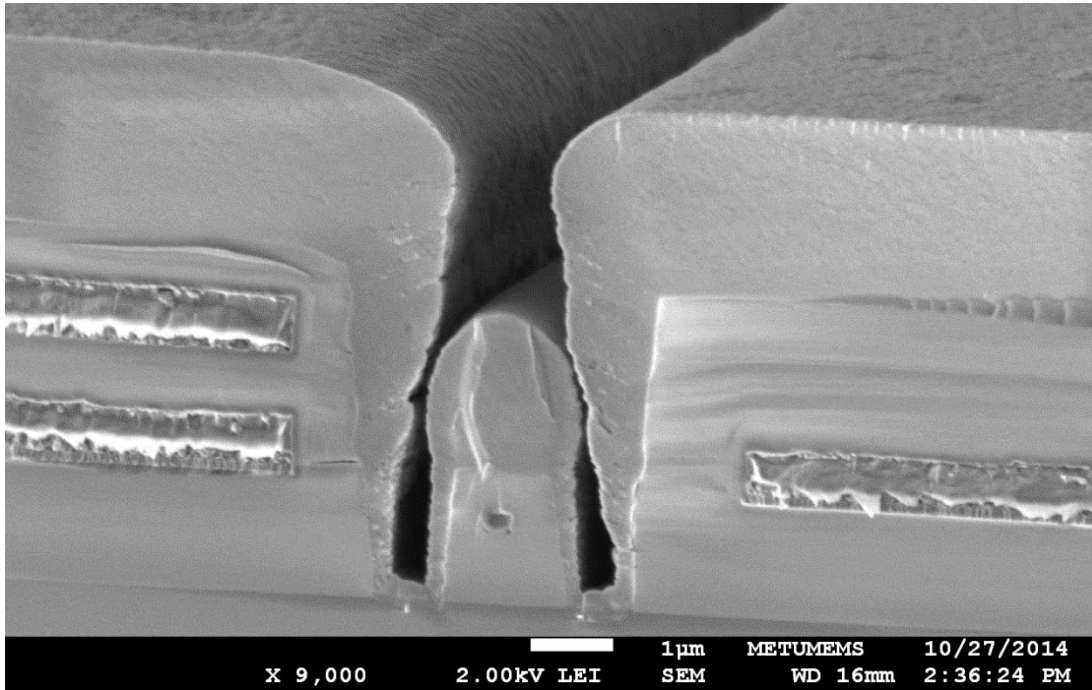


Figure 3.9: SEM image of the cross-section of the 70 μm low-cost pixel after depositing 3 μm thick a-Si as the sacrificial layer in the most non-conformal method using PECVD. There is a wide opening atop the arm that prevents proper umbrella material deposition as the succeeding step.

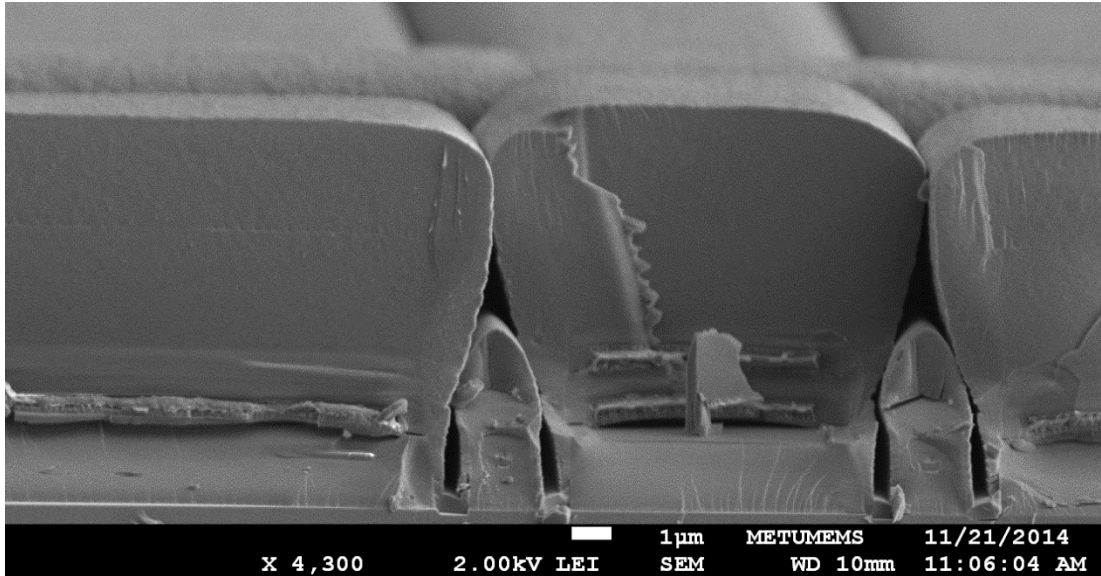


Figure 3.10: SEM image of the cross-section of the 50 μm low-cost pixel after depositing 6 μm thick a-Si as the sacrificial layer in the most non-conformal method using PECVD. The complete sealing of the arm spacing is only possible after 6 μm a-Si deposition, which is not a realistic air gap height for the considered umbrella geometry.

It is evident that depositing a-Si as the sacrificial layer is not adequate to meet the fundamental needs for the subsequent fabrication steps. Therefore, filling the trenches of the low-cost topology with a polymer-like material is investigated as the solution to the problem. In addition, new dummy pixels that emulate the low-cost geometry realistically are fabricated that is explained in the next section.

3.3. Dummy fabrication with PI layer

New dummy substrates are prepared to fully mimic the low-cost pixel topology with the arm height lower than the pixel body and the pixel wall. Instead of one step etching, two steps of patterning and etching are performed in the RIE tool to form the arms first, then lowering the arm height by masking other features on the substrate. Figure 3.11 shows the SEM image of fabricated dummy structures.

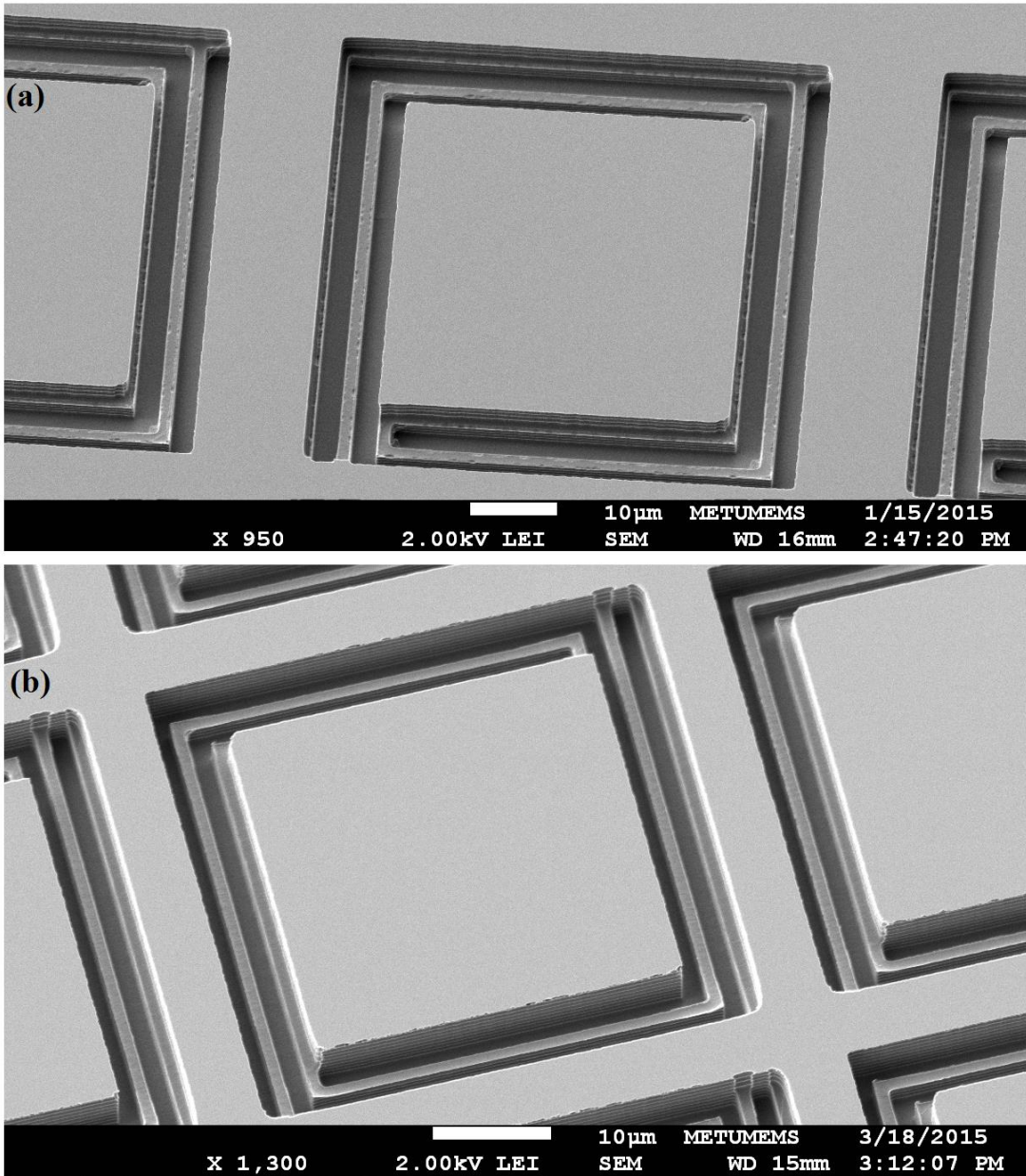


Figure 3.11: SEM images of modified (a) 50- μm dummy pixel and (b) 70- μm dummy pixel. Even though there is a slight alignment problem of the second etching patten, the arm height is reduced to realistic levels relative to the pixel frame and the body.

The previous related studies conducted at the METU-MEMS facilities [22, 35, 99] had employed polyimide as the sacrificial layer. Once polyimide is cured in oven at 350°C, it can withstand temperatures around 300°C without thermally decomposing [22]. PI 2556 by HD Microsystems is used to fill the trenches of the low-cost pixel topology. Since it can be spin coated, the thickness of the sacrificial layer can be adjusted by spin speed. Optimization of the sacrificial layer coating had been performed previously [35] on a silicon wafer. Although PI 2610, can achieve the desired thickness value, around 2.5 μm , its wetting properties are weak due to high solid content; hence filling the trenches with PI 2610 resulted in air gaps. PI 2556 is spun at 2000 rpm on the dummy structures and excellent wetting of the polymer is observed. The desired thickness value is established through spin coating the polymer second time after a 5 minute soft bake at 130°C on a hot plate. Therefore, the trenches are filled as required, and 2.6 μm thickness is attained after curing.

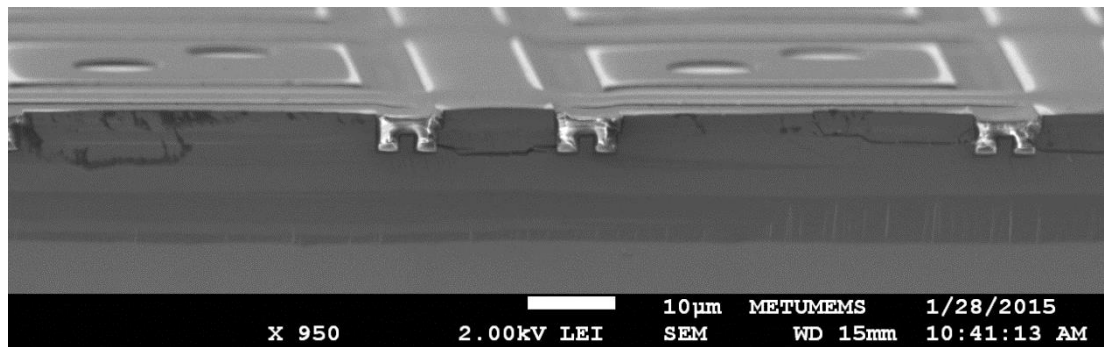
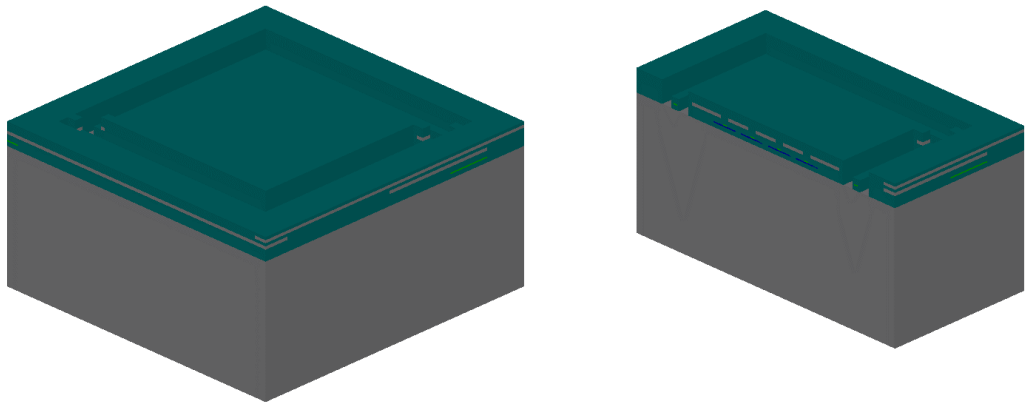


Figure 3.12: SEM image of the cross-section of 70- μm dummy pixel after top layer of the cured PI 2556 is removed. Note that the arm spacing is completely filled with the polymer acting as desired.

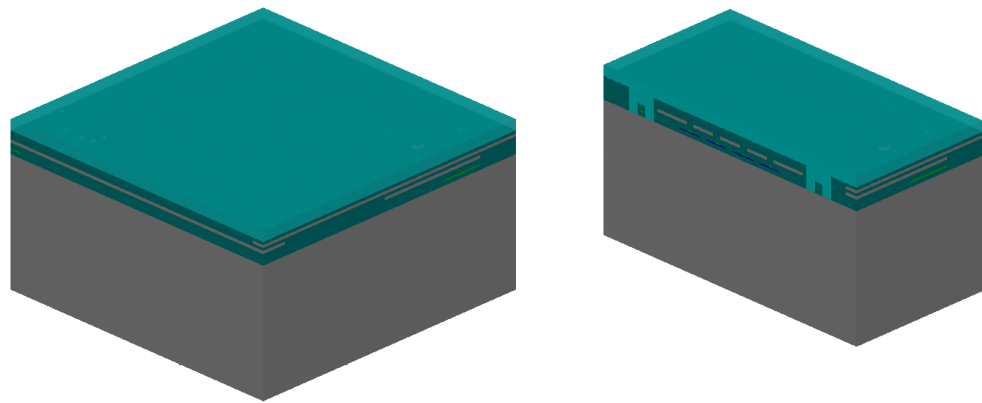
3.4. CMOS fabrication with PI sacrificial layer

Upon confirming the capabilities of PI 2556 as the new sacrificial layer, CMOS detectors are integrated with umbrella structures on the FPAs on wafer level. Firstly, CMOS detectors with the array size of 160x120 with 70 μm pixel pitch, that had undergone third revision [48], are integrated with umbrella structures. After a successful run, another CMOS detector array with the same size but 50 μm pixel pitch

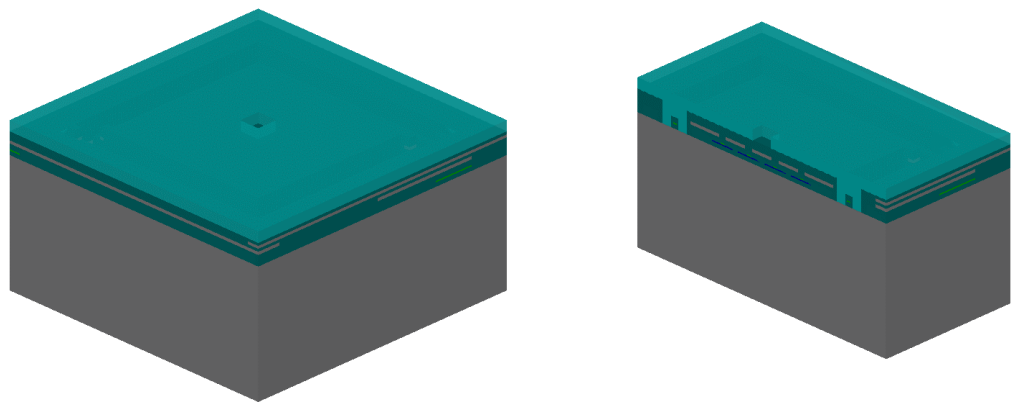
is integrated with the umbrella design. The CMOS sensor fabrication details for each detector array have been provided in the previous investigations. The post-CMOS process of these detectors are performed firstly to reveal the arms of the pixels. Then underneath the pixel is removed to suspend the pixels using isotropic etchant TMAH [46, 48]. Right before the release step, after the pixel arms are revealed, umbrella fabrication procedure steps in. The details of each process step is disclosed in the following subsections. However, a generic schematic process flow is presented in Figure 3.14.



a) Low cost pixel before release process

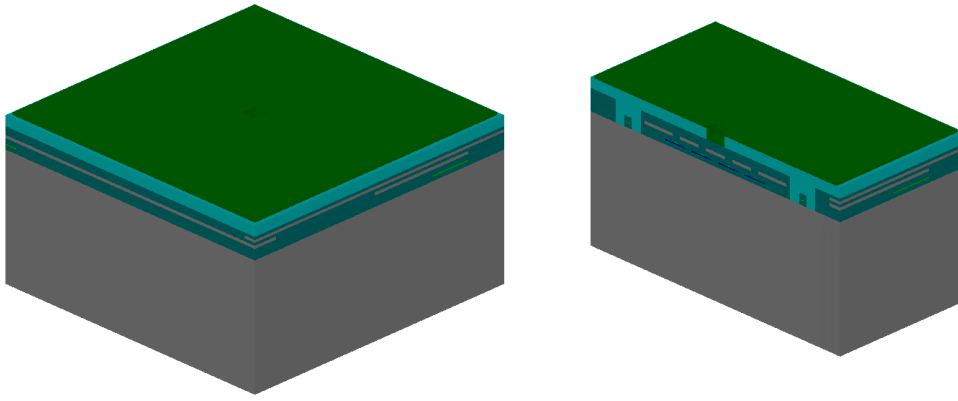


b) Sacrificial layer coating

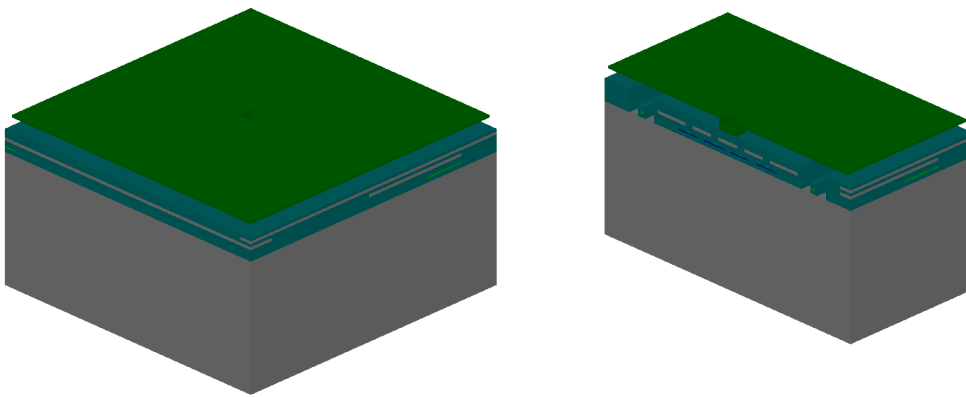


c) Anchor patterning and etching

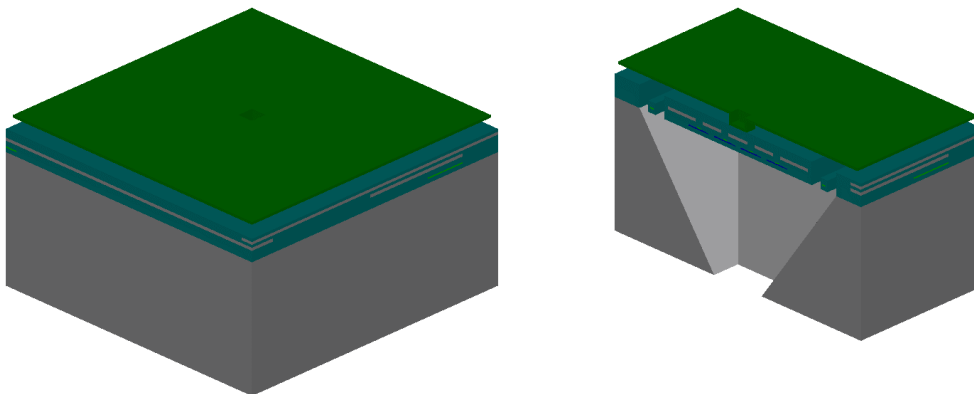
Figure 3.13: Schematic process flow of the low-cost pixel umbrella integration on a $70\ \mu\text{m}$ pitch pixel with single square post.



d) Umbrella layer deposition and frame etching



e) Sacrificial layer release



f) Pixel release in TMAH

Figure 3.14: Schematic process flow of the low-cost pixel umbrella integration on a $70\ \mu\text{m}$ pitch pixel with single square post. (continued)

3.5. Umbrella structure integration onto 70- μm pitched pixels

Integration of the umbrella structures onto low-cost detectors takes place in wafer level. Before coating the sacrificial polymer layer, as the first post-CMOS process, the arms are exposed but still resting on the silicon substrate with etch openings. Figure 3.15 shows the SEM image of the arms of a low-cost detector with 70 μm pitch.

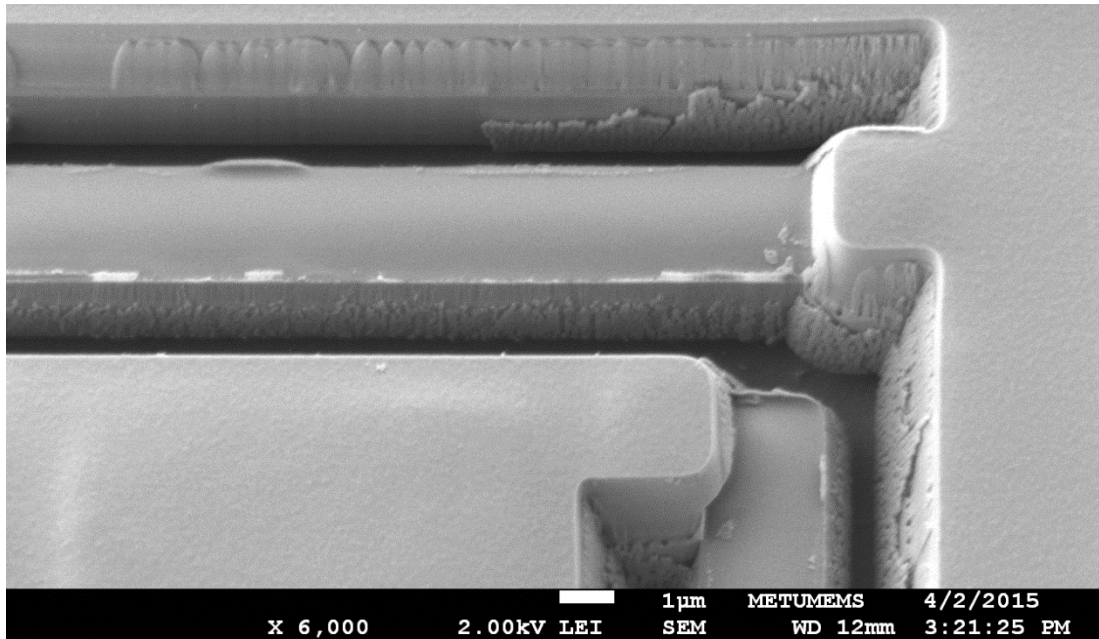


Figure 3.15: SEM image of the 70- μm pitched low-cost pixel before coating sacrificial layer.

PI 2556 is spin coated at 2000 rpm with static dispose, then soft-baked on a 130°C hot plate. Following the first soft-bake, a second layer of PI 2556 is spin coated at the same speed. A second soft-bake is performed prior to curing in a nitrogen purged oven at 350°C for one hour at a ramp rate of 2 °C/hr to allow stress free curing. After curing is complete, a very thin (~30 nm) SiO₂ layer is deposited to utilize as a hard mask during sacrificial layer etching of the anchor patterns. The oxide mask is etched then the sacrificial layer is etched on the same tool consecutively using similar recipe parameters. Figure 3.16 shows the SEM image of a part of the array after etching the anchor patterns on the sacrificial layer. It is worth mentioning that the arm topology

of the low-cost pixels are reflected –although smoothed on the surface due to polymer properties.

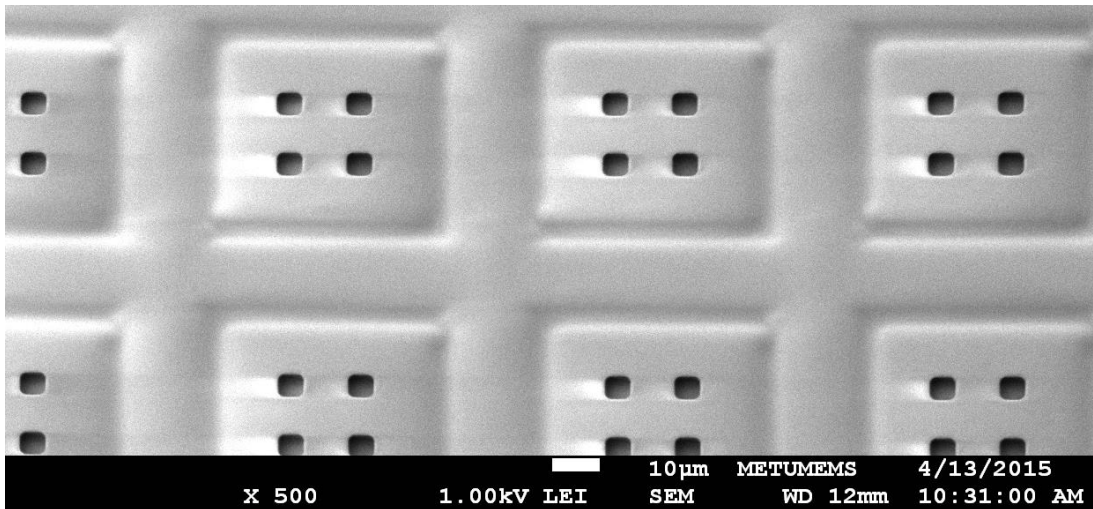


Figure 3.16: SEM image of the 70- μm pitched low-cost pixels after etching the anchor openings on the sacrificial layer. Note that there are four posts on each pixel body and the arm topology is still visible.

Following the anchor formation, thin SiO_2 layer is removed completely in the same tool. Next, silicon nitride that is 600 nm thick is deposited using the stress free recipe in the PECVD tool. Then, each umbrella span is defined through photolithography and etched in the RIE tool until the sacrificial layer underneath is exposed.

Then the wafer is diced to access each die separately as the proceeding steps can be performed in die level. Umbrella structures are released in oxygen plasma since the cured polymer can easily be removed as stated in the previous studies [22, 35, 99]. There are number of parameters to consider at this point regarding the successful release of umbrella structures as well as the release of the low-cost pixels. Figure 3.17 depicts the low-cost pixels with 70 μm pitch. It should be noted that the sacrificial layer is not completely removed in the figure, where polymer is seen as the bright region due to charging effect of the polymer in the SEM. Also, the anisotropic etching starts below the arms where silicon is exposed to TMAH at the beginning. The “V” shaped grooves can be observed where the etching starts.

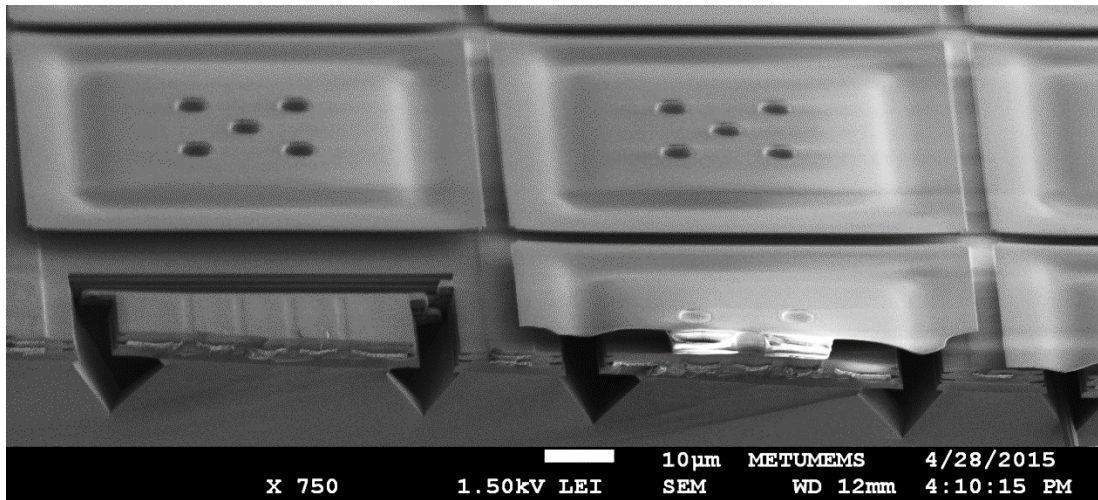


Figure 3.17: SEM image of the cross-section of a 70- μm pitched low-cost detector array with integrated umbrella structures. Note that the sacrificial layer is not completely removed around the posts. Also, the pixel is not completely released since it is connected to the substrate although anisotropic etching has started below the arms.

Early trials of the pixel release procedure in TMAH are performed while the umbrella layers were completely released in oxygen plasma. However, fully suspended umbrella layers are weakened at the anchor edges during TMAH etching times that lasts 160 minutes. Therefore, the umbrella layers are partially released while leaving some of the sacrificial layer around the posts as mechanical support. After the pixels are fully released, the remaining polymer is eliminated in oxygen plasma. However, since the arm spacing of the pixels are narrower than designed due to the initial post-CMOS process, release time of the pixels harm the silicon nitride layers. Some of the umbrella structures are detached from the pixels as some of them are buckled due to stiction as can be observed in Figure 3.18 (b).

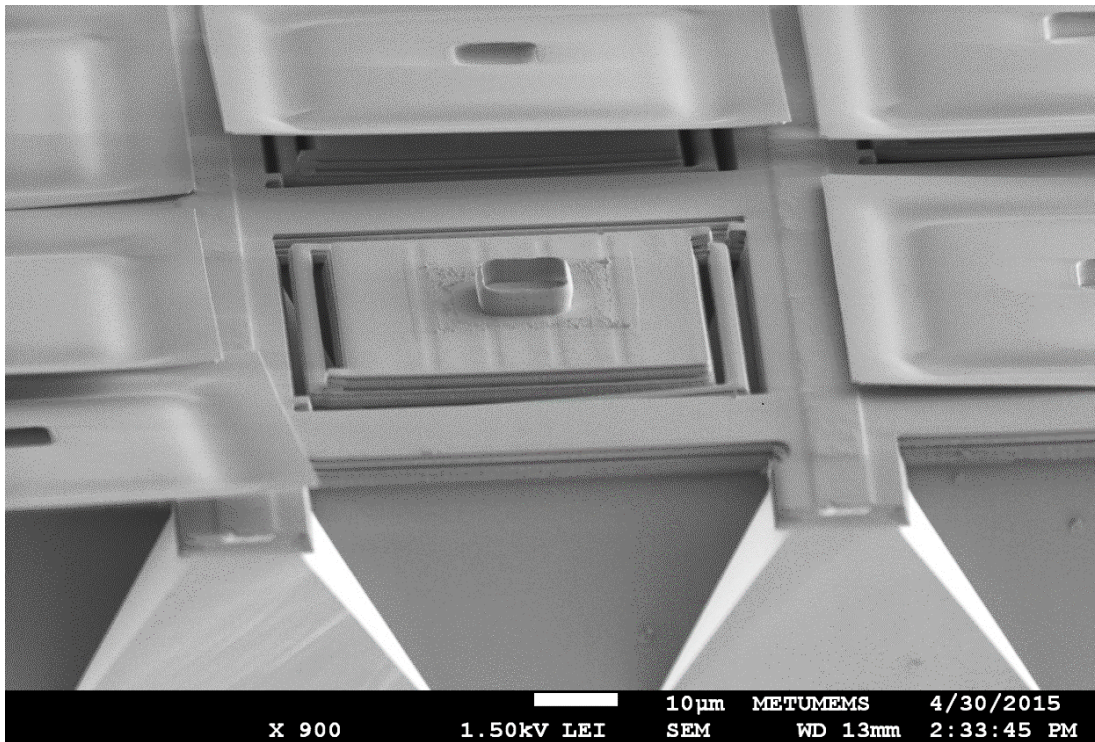
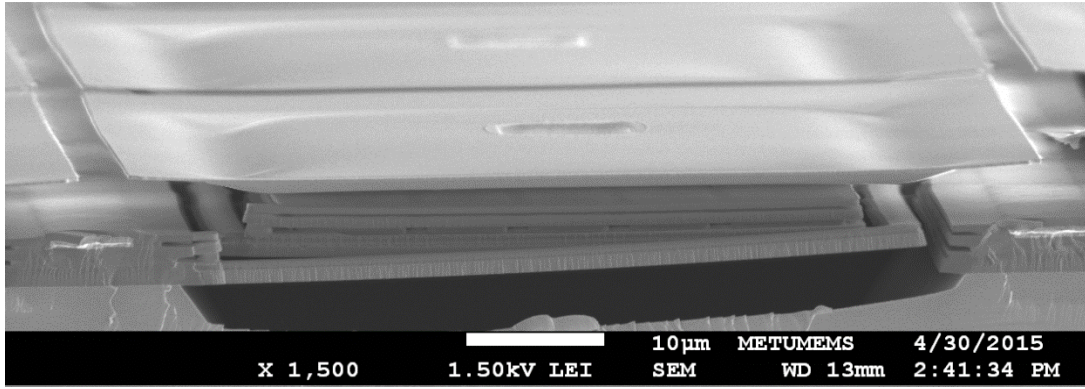


Figure 3.18: SEM images of the completed umbrella structures on low-cost pixels with 70 μm pitch. Note that in (b) some umbrella structures are detached from the post where it connects due to thinning during TMAH etching, while some are stuck to the surface while drying due to stiction problem.

3.6. Umbrella structure integration onto 50- μm pitched pixels

Integration of the umbrella structures onto the low-cost pixels with 50 μm pitch and array size of 160x120 is performed similar to the previously optimized case, as elaborated in the subsection before. As the arms of the pixels are revealed, sacrificial layer is spin coated twice and cured with the same temperature programming. After curing, SiO₂ mask is deposited and patterned. Using the SiO₂ mask, the anchors are etched in the RIE tool. Then, 600 nm thick silicon nitride layer is deposited on the wafer. The umbrella frames are patterned and etched before the wafer is diced. As access to individual dies are enabled after dicing, die level umbrella and pixel release trials are investigated.

The arm spacing that acts as the initial release region of the TMAH etching, has wider opening on these particular detectors due to more perpendicular sidewall profile of the pixel wall and the arms. Therefore, the initial pixel release trials in TMAH are experimented with fully released umbrella structures. As expected, the release time of each die in TMAH is measured to be around 80 min, which is half of the release time required for the pixels having 70 μm pitch with the same array size. Since the silicon nitride layer is not harmed in shorter duration immersed in TMAH, umbrella structures throughout the entire FPA survives the release process. Passive drying of the pixels in alcohol or water after the release procedure results in significant buckling of the pixels –not the umbrella geometries themselves. Buckled pixels, expectedly, causes the umbrella layers to stick onto the substrate. Although annealing has been proven to be effective up to certain extent by past experiments, it is both costly, and not well controlled. Instead, drying the released dies in critical point dryer (CPD) is suggested. It is concluded that the pixels after a fruitful CPD process in ethanol, about 99.8% of the pixels are dried without visible buckling problem. Figure 3.19 shows the SEM image of completed umbrella integration onto low-cost pixels with 50 μm pitch.

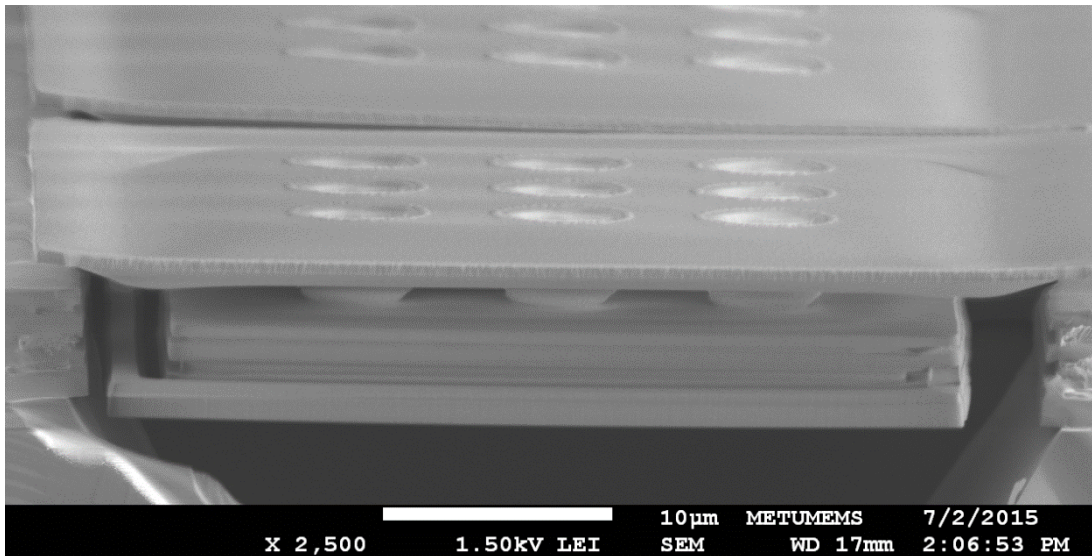


Figure 3.19: SEM image of the low-cost pixel with 50 μm pitch after being fully released in TMAH. Note that this particular design includes 9 circular posts that connect the umbrella to the pixel body.

Differently from the previous fabrication of umbrella on low-cost detectors with 70 μm pitch, there are 4 different regions on the FPA each consisting of rows of 30 with 160 pixels in columns. Figure 3.20 shows the schematic representation of the FPA divided into four categories labeled from “A” to “D”. The first region on each die has no umbrella attached while the other three has different designs, where Design #2 includes perforations on the umbrella to ease the oxygen plasma release time, which is proved to be effective. This arrangement allows a fair comparison of the umbrella contribution to the responsivity of the detector when the FPA is tested under uniform blackbody illumination. Figure 3.21 shows another SEM image of the suspended low-cost detector pixels with and without umbrella structure on the same FPA, as designed.

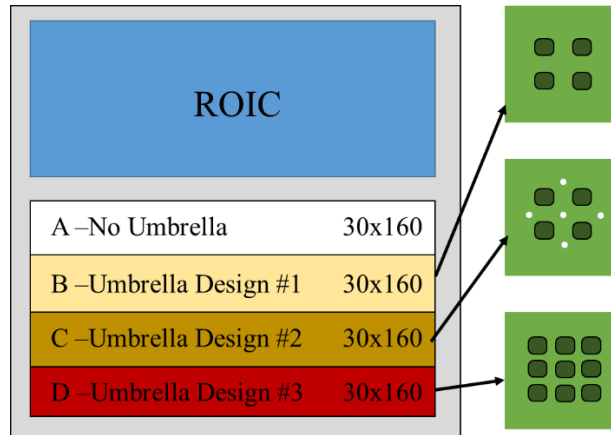


Figure 3.20: Schematic representation of the placement of different umbrella designs with a row of 30 on the low-cost FPA with a size of 160x120 pixels

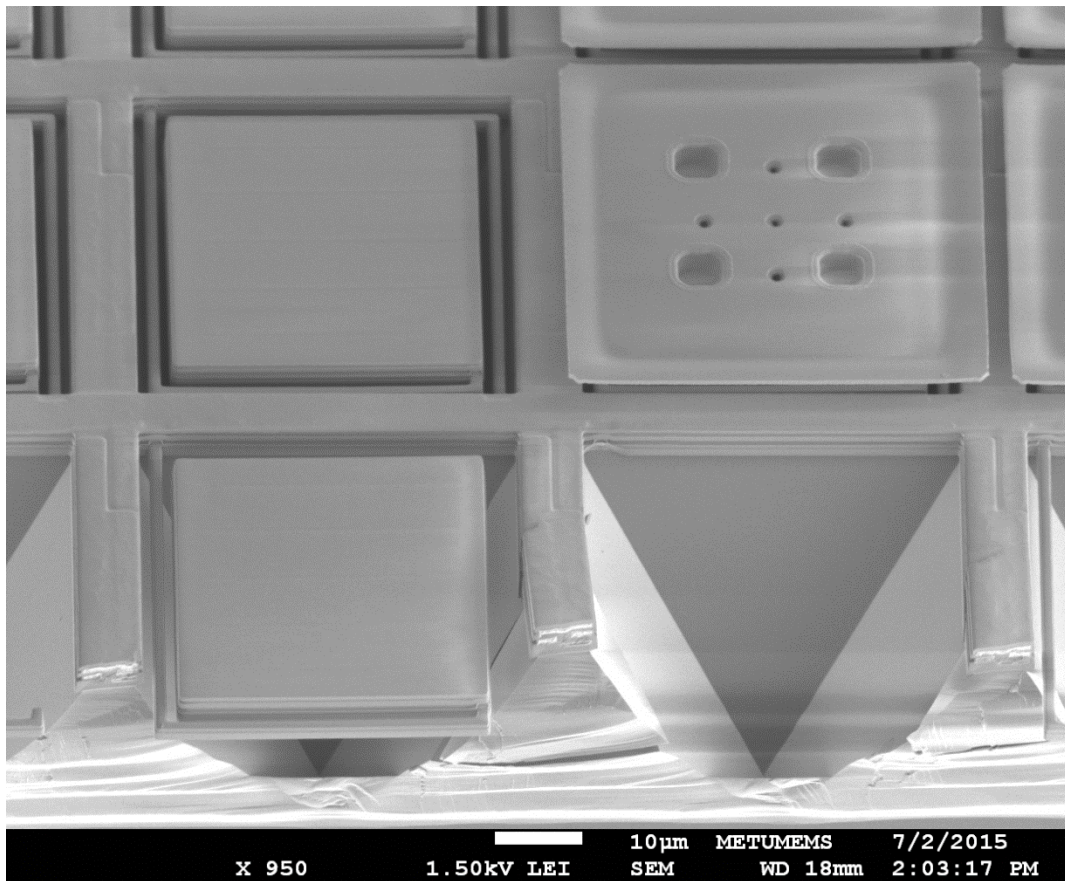


Figure 3.21: SEM image of the low-cost pixel with 50 μm pitch after being fully released in TMAH, where inverted pyramid geometry can be seen as the result of anisotropic wet etching. Also, the FPA is designed to have umbrella structures (with perforations) and pixels having no umbrella for a fair comparison.

Suspended dies, are placed on 84-pin leadless chip carrier (LCC) packages with the help of epoxy; then bonded using wire-bonder tools on appropriate pinouts for testing the dies in vacuum condition. Before electronic tests, the dies are optically tested with Fourier Transform Infrared Spectroscopy (FTIR). Therefore, next chapter explains the test setup of the uncooled microbolometer FPAs and the resulting performance of the detectors.

CHAPTER 4

PERFORMANCE EVALUATION TESTS

Contribution of umbrella structures to the integrated microbolometer arrays are evaluated in two ways. Firstly, an optical evaluation of the FPAs are performed by measuring the infrared response of the umbrella structures on the FPA using an FTIR tool. This measurement indicates the infrared response of the entire system meaning, which does not imply that every dip in the reflection spectrum is transduced into measurable signal by the detector since some of the light will be transmitted or reflected from the frames of the pixels and arms that are both not thermally connected to the temperature sensitive element. Secondly, detectors are tested under vacuum conditions

4.1. Measured FTIR Results

The fabricated dies are tested using the same FTIR tool that is mentioned at the beginning of Chapter 2. The reflection spectra $R(\lambda)$ of the low-cost FPAs are measured in the infrared window, then absorption is calculated as $1 - R(\lambda)$ assuming no transmission through the bottom of the substrate. Since low-cost detectors with 70 μm pitch have all the pixels integrated with umbrella on the same FPA, a different die of the exact generation low-cost FPA is used to compare the optical response of the pixels. Figure 4.1 shows the spectral response of the 70- μm pixels in array format that are integrated with umbrella compared to the plain pixels with no umbrella structure attached.

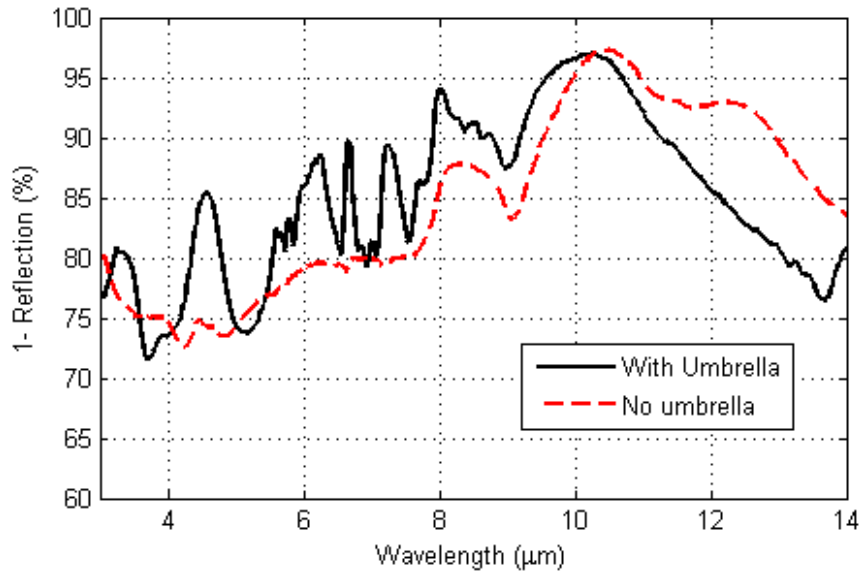


Figure 4.1: Measured FTIR response of the low-cost detector with 70 μm pitch in array format. Pixels with umbrella structure and without umbrella structure are compared. It should be noted that different umbrella designs yield almost identical results.

Addition of the umbrella does not yield a strong increase in the 10 – 12 μm wavelength range, mostly because the absorption around this region is already above 90%. There are number of parameters that can explain the discrepancy between the simulated and the measured results. Firstly, the geometry is approximated in the FDTD modeling with no topology effect taken into account. Second most important point in question is the material detail as well as the optical characteristics match. It should be noted that poly-silicon interconnects and doped diode silicon regions are modeled due to lack of material information. In addition, the silicon oxide layer that makes up most of the detector is deposited in the CMOS foundry where the oxide quality, hence the optical characteristics might slightly be different. There is, however, a 4 % increase of the average absorption in the LWIR range when umbrella structure is added. The air gap generates oscillating reflection dips that are reflected in the absorption.

In a similar fashion, contribution of the umbrella structure is presented via FTIR measurements of the low-cost detector FPA with 50 μm pixel pitch. On these dies, however, there are 4 different regions of which one does not employ the umbrella structures as seen in Figure 3.20. The regions with different umbrella post patterns

yield indistinguishable results. The contribution of umbrella structure to the optical response is presented in Figure 4.2 integrated onto low-cost pixels with 50 μm pitch.

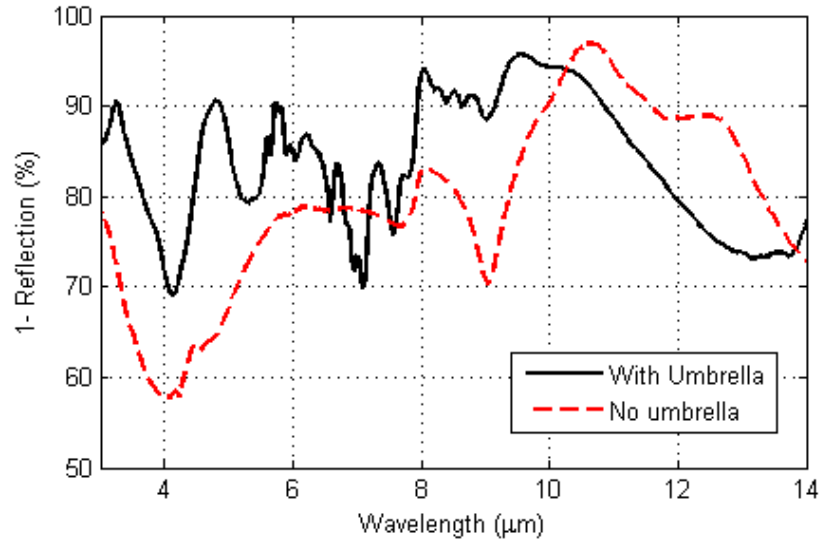


Figure 4.2: Measured FTIR response of the low-cost detector with 50 μm pitch in array format, measured on the same die. Pixels with umbrella structure and without umbrella structure are compared. It should be noted that different umbrella designs yield almost identical results in optical domain.

Parallel to the previous results, addition of the umbrella does not yield a strong increase in the 10-12 μm wavelength range, again mostly because the absorption around this region is already above 90%. There is significant increase in the 3-5 μm wavelength region (labeled as MWIR). Moreover, there is visible increase in the 8-10 μm wavelength region. The oscillatory response that is present is the addition of air gap between the pixel surface and the umbrella structure. The average absorption in the LWIR window is improved by 4 %. Although the increase in the average absorption may not seem substantial in both cases, it should be noted that fill factor is not accounted for these comparisons. It can be further elaborated that the optical response obtained from the areas other than that the pixel body on the FPA is utterly ineffectual since there is no contribution to the signal generated. On the contrary, the umbrella layer spans most of the space between pixels and the absorbed radiation is

transferred to the temperature sensitive element embedded into the pixel body. As a reminder, the low-cost pixels with 70 μm pitch have fill factor of 36 %, and the umbrella structure improves the fill factor to 94 % while the fill factor of the low-cost detectors with 50 μm pixel pitch is increased from 46 % to 92 %. Therefore, the effective power utilized by the sensor is more than reflected on the optical response figures. Next section provides responsivity tests conducted with controlled black body radiation tool in order to demonstrate the concrete improvement by the addition of umbrella structures.

4.2. Responsivity Tests

Since low-cost detectors with 70 μm pitch do not have pixels without umbrella structures on the same FPA, various dies are tested under the same conditions with and without umbrella structures in order to obtain an average measurement. Each die, after being suspended, are attached onto an 84-pin LCC package. Then each die is placed into a dewar with camera electronics in order to capture images. A blackbody is placed in front of the dewar that is equipped with an F/1 lens. Series of frames are recorded under the blackbody temperatures of 20 $^{\circ}\text{C}$ and 30 $^{\circ}\text{C}$ respectively. The difference between the captured images are processed in MATLAB to produce the responsivity and NETD histograms. A more detailed test setup and electronics are elaborated in [48].

Firstly, number of FPAs comprising 70 μm pitch pixels with no umbrella structures are tested and almost identical results are obtained under the same bias conditions. Figure 4.3 shows the responsivity and the NETD histogram of a measured die. The resulting average values and distributions for three different dies are highly similar including the noise count that is not presented here. In addition, the dewar vacuum level is set to 15 mTorr for both measurements. The exact same procedure is then applied to the same generation dies that are fabricated with umbrella structures. The entire FPA is constructed with 600-nm thick umbrella structures freestanding on low-cost pixel bodies with 4 square posts with a size of 5 μm . Figure 4.4 shows the responsivity and the NETD histogram of a measured die that is integrated with umbrella structure.

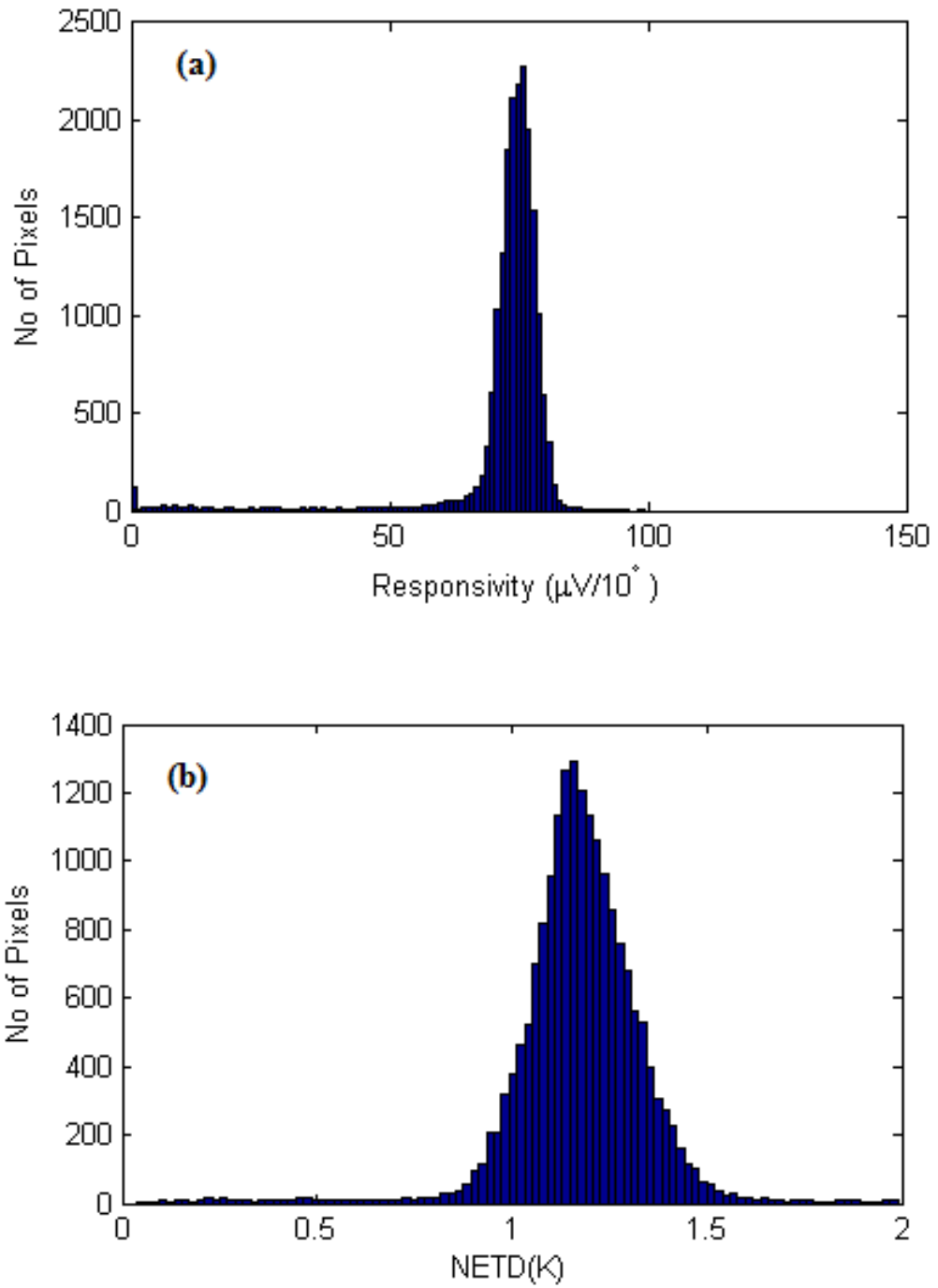


Figure 4.3: Measured (a) input referred responsivity and (b) NETD of the 160 x 120 array of FPA with 70 μm pitch pixels. The peak responsivity occurs at 70 $\mu\text{V} / 10^\circ\text{C}$ resulting a peak NETD of 1.16 K.

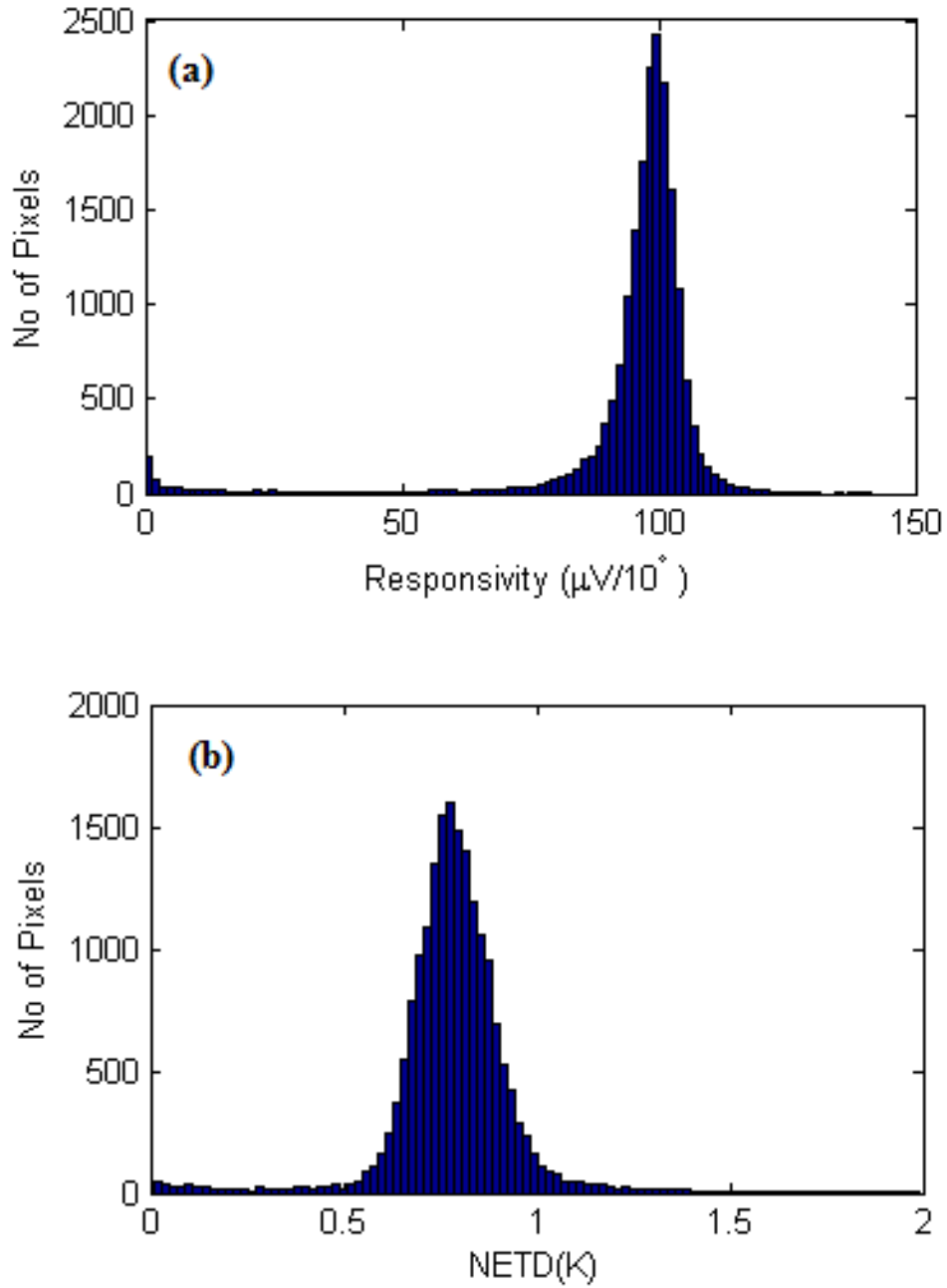


Figure 4.4: Measured (a) input referred responsivity and (b) NETD of the 160 x 120 array of FPA with 70 μm pitch pixels with umbrella structures integrated that are 600 nm thick comprising 4 posts with a size of 5 μm . The peak responsivity occurs at 100 $\mu\text{V} / 10^\circ\text{C}$ resulting a peak NETD of 774 mK.

The resulting responsivity after the integration of umbrella structures with a thickness of 600 nm, increases by a factor of 1.4, where the FPAs with no umbrella result in a peak input referred responsivity of 70 $\mu\text{V}/10^\circ\text{C}$, and the FPAs with integrated umbrella structures yield a peak input referred responsivity of 100 $\mu\text{V}/10^\circ\text{C}$. The decrease in the peak NETD is almost the same, considering the system level noise performance of all measurements are not identical but highly similar.

Low-cost detectors with 50 μm pitch are also tested under same conditions, however, a single die test reveals the true contribution of the umbrella layer since pixels with and without umbrella structures are located on the same die. Figure 4.5 shows the responsivity map of the FPA. It is conspicuous that the top 30 rows of pixels have no umbrella and the responsivity is visibly lower compared to the pixels with umbrella structures. Another observation reveals that within the regions incorporating different types of post numbers and distributions as schematically represented in Figure 3.20, there is no visible difference.

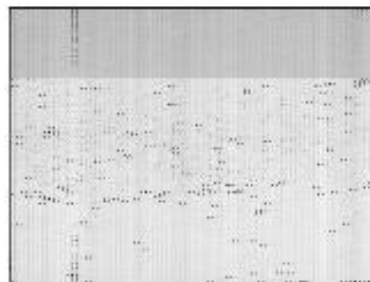


Figure 4.5: Responsivity map of the low-cost detector with 50 μm pixel pitch. Note that that the top 30 rows of the FPA has darker color, indicating that the responsivity of this region is lower than the rest of the FPA. Moreover, within the different umbrella structures, there seems no visible distinct responsivity result.

The quantitative analysis of this observation, however is presented in Figure 4.6, where responsivity of the array is shown in histogram. It is definite that the smaller distribution marking the lower responsivity region, making up one quarter of the FPA, has average responsivity that is 30 % lower than the region consisting of pixels with

umbrella structure. Figure 4.7 shows the resulting NETD histogram of the FPA, of which the peak NETD is registered as 260 mK whereas the average NETD value is 278 mK.

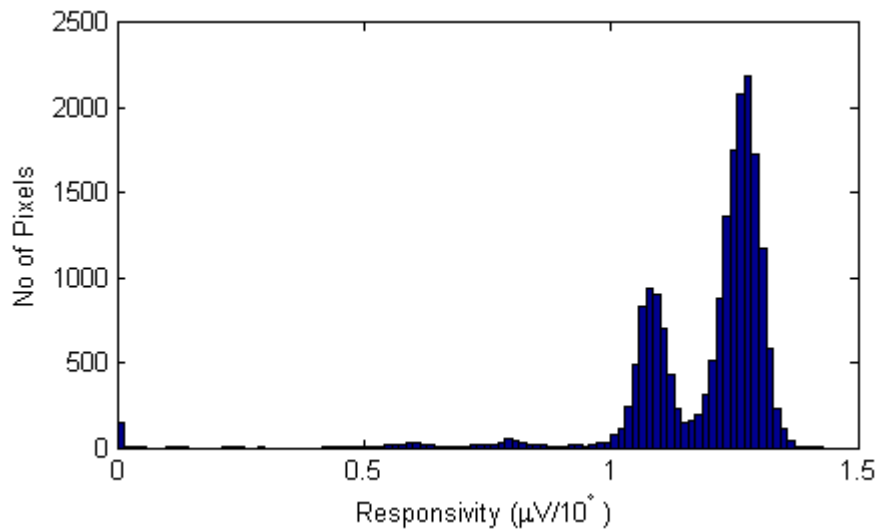


Figure 4.6: Input referred responsivity histogram of the tested low-cost detector with 50 μm pitch. There are two main distributions due to having regions with and without umbrella. The lower responsivity region, making up one quarter of the FPA, has lower number of distribution as well as average responsivity that is 30 % lower.

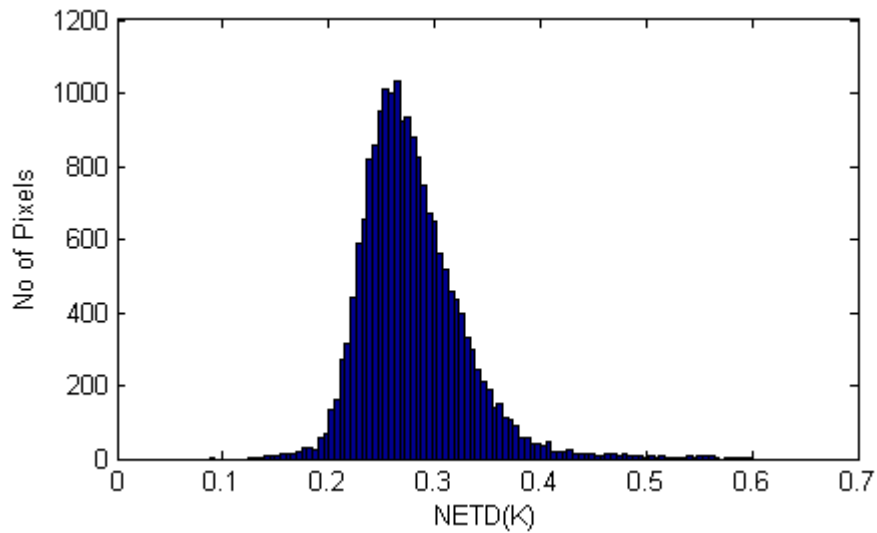


Figure 4.7: NETD histogram of the low-cost pixel with 50 μm pitch with average NETD of 278 mK while the peak NETD is 260 mK. Note that the distribution of pixels generate a tail that broadens the peak towards larger NETD values due to the region with no umbrella integrated.

The tail of the NETD histogram that disrupts the Gaussian distribution towards the higher NETD values is caused by the region with no integrated umbrella structure since the responsivity of these pixels are 30 % lower than the average of the rest of the FPA. The same dies are also tested under different bias conditions to yield lower temperature sensitivity. Although the responsivity of the FPA is reduced due to altered temperature sensitivity of the diodes, the fill factor effect remains as observed in Figure 4.8.

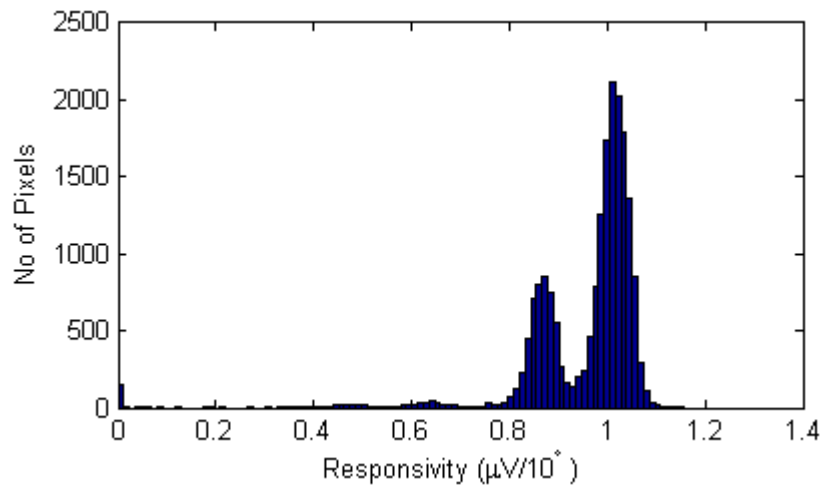


Figure 4.8: Input referred responsivity histogram of the tested low-cost detector with 50 μm pitch under different bias conditions. Two main distributions are observed regardless of the biasing condition, which implies the fill factor contribution to the responsivity.

CHAPTER 5

CONCLUSION AND FUTURE WORK

The investigation of umbrella structure design and integration to already existing two distinct generations of low-cost pixels has been conducted in the scope of this thesis. The figure of merits are briefly introduced pertaining to uncooled infrared detectors. Importance of responsivity and absorption is conveyed. The trend in pixel size reduction is justified in terms of higher resolution and lower fabrication cost. However, as pixel size is reduced, the need for longer and more complex thermal isolation structures increases. Thus, smaller fraction of the sensor unit cell is dedicated to temperature sensitive are, causing the responsivity drop.

Number of studies are presented pertaining to integration of high fill factor structures into uncooled infrared sensor arrays. Among these examples, most microbolometers are commercially available FPAs. In addition, most of the high fill factor structures utilize silicon nitride (SiN) deposited in PECVD due to its mechanical, thermal, and optical properties. There are, however, examples of other materials, or combination of materials presented for certain applications or desired optical response in the infrared regime of interest.

Two probable candidate materials are evaluated in mechanical domain firstly. It is concluded that the residual stress of silicon nitride deposited in PECVD can be tuned to obtain stress free films with very little stress gradient. On the other hand, silicon dioxide deposited in PECVD can be low-stress but the film is more prone to buckling due to stress gradient. Therefore, silicon nitride is determined to have preferable

qualities with regard to mechanical properties as umbrella structures are free-standing on pixel bodies.

Optical characteristics of both silicon nitride and silicon dioxide are measured using ellipsometric means in the infrared regime. Two different PECVD tools are used to deposit both films, and as a result of analysis each dielectric coated using two separate tools are concluded to have greatly analogous optical characteristics. Extracted optical constants through ellipsometric measurements are verified by measuring the reflection spectra of materials coated on gold substrate using FTIR. The measured spectra are compared with the simulated spectra using a commercial FDTD solver. Resulting an ideal match between the simulated and measured spectra, 2D simulations are performed to sweep various combinations of silicon nitride and silicon dioxide incorporating different thickness values and different air gap values to form a resonance cavity. The air gap value range is justified and 3D FDTD simulations are performed to observe the effect of thickness on 50- μm and 70- μm low-cost pixel geometries.

Transient thermal simulations are run for 50- μm and 70- μm low-cost pixels with no additional structures under different input powers and the overall G_{th} and thermal time constant of the pixels are extracted through equation fitting. The obtained values are firstly compared with the previously reported values, then umbrella structures with different thicknesses and post geometries are simulated for both 50- μm and 70- μm low-cost pixels. It is concluded that the addition of umbrella layer does increase the thermal time constant of the pixels 7 % and 9 % for 50- μm and 70- μm low-cost pixels respectively when 600 nm thick silicon nitride layer is added. It is also deduced that there is no noticeable difference in heat transfer when the number of posts are changed from 1 to 9 to yield a better heat transfer.

Realization of umbrella structure with various post size and numbers are successfully completed using a polymer sacrificial layer (PI 2556) and depositing silicon nitride with a thickness of 600 nm. Identical process flows are followed for integration of umbrella on both 70- μm and 50- μm low-cost pixels. The process flow is optimized to include no wet process, and greatly tolerant non-timed steps to ease the fabrication. It

is demonstrated that the umbrella structure is scalable for difference pixels size and geometries.

Performance analysis of the umbrella added FPAs are conducted by recording the optical response of the FPAs using an FTIR. The true contribution of the umbrella structure is assessed by responsivity tests that re conducted in vacuum condition. It is observed that the addition of umbrella increased the responsivity by 30 % and 40 % for 50- μm and 70- μm pixel FPAs.

There are, however, ongoing and future work regarding further enhancement in pixel level. Many of the reported detector structures include an additional layer to maximize the absorption in broadband. There are various approaches to maximize the broadband absorption such as impedance matching through coating thin metal layers [22, 35, 69, 100-102], impedance matching through perforated structures [66, 103-105], using gold-black coatings [106], and metamaterial or plasmonic absorbers [107-112].

Impedance matching by depositing a thin metal layer with a high resistivity is a common method to tune the layer stack of the microbolometers to the impedance of air, which is $377\Omega/\square$ [100, 113]. Preliminary work is done on impedance matching considering the low-cost pixels integrated with the umbrella structures. NiCr sputtering is chosen due to availability.

Since the resistivity of the deposited NiCr layer is not measured within a reasonable certainty different deposition times are applied to a stack of gold/silicon nitride on silicon substrate as depicted in Figure 2.5. Then the FTIR reflection spectra are measured for each stack where the silicon nitride and gold layers are identical but the NiCr layer deposition time changes. Figure 5.1 shows taht with increasing the deposition time, hence thickness, the impedance of the collective system is altered in a way to match closer to the impedance of free space.

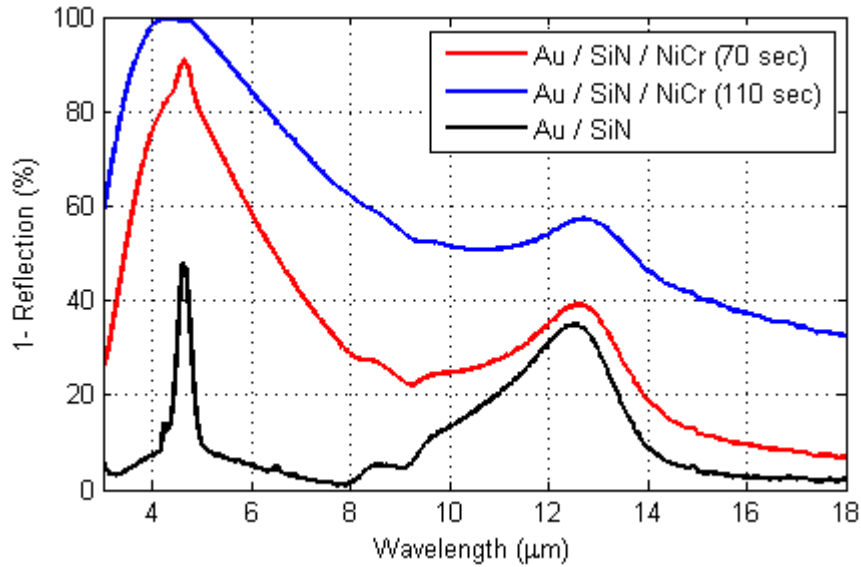


Figure 5.1: Measured FTIR spectra of Au/SiN/NiCr stack where the thickness of the NiCr layer is varied. Note that addition of NiCr increases the absorption significantly.

This preliminary result does not prove any quantitative analysis since the motivation behind it is to work backwards with a cascaded transmission line (CTL) model to define a possible range of the resistivity of the NiCr layer to correctly correlate the thickness and the sheet resistance of the sputtered layer for future processes. Therefore, the ongoing study provides the initial characterization of the NiCr coating. Figure 5.2 shows the same measured FTIR plots of the silicon nitride on gold substrate with and without NiCr atop, overlaid with the computed spectra using CTL. The optical constants of silicon nitride is fed into the CTL code obtained from the extracted data by ellipsometric means as explained in Chapter 2.

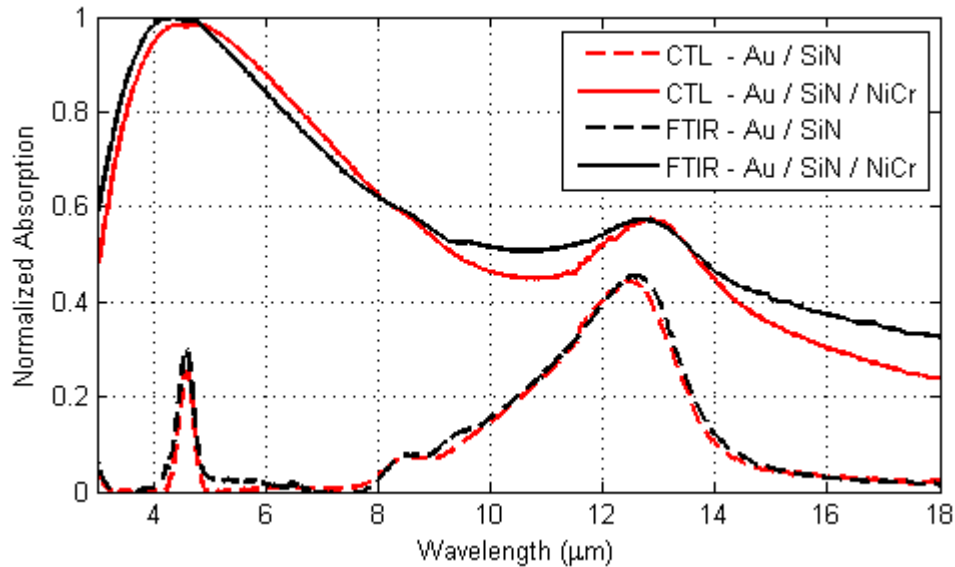


Figure 5.2: Comparison of the computed absorption using CTL and measured absorption spectrum of 620 nm of silicon nitride on gold substrate with and without NiCr coating.

It is observed that the computed absorption spectrum of Au/SiN stack perfectly matches the measured Au/SiN stack. There are, however, minor discrepancies in the Au/SiN/NiCr stack between measured and the computed data. Two major contributions to the discrepancy is responsible, one being the uniformity of the sputtered NiCr film. The second contribution comes from the range of possible sheet resistance values. The plot above is constructed with adding a $300 \Omega/\square$ NiCr parallel to the Au/SiN stack. However, altering the sheet resistance within 10 % uncertainty boundary yields similar results.

In parallel with modeling and characterization, it is crucial to assess the feasibility of the NiCr sputtering in terms of fabrication. Since the outermost layer is the silicon nitride umbrella, NiCr coated surface must withstand the following release procedures, which include exposure to TMAH release more than an hour as well as exposure to oxygen plasma to release the polymer sacrificial layer underneath the umbrella structure. Figure 5.3 shows the measured FTIR spectra of the pieces of same wafer that has Au/SiN/NiCr layer stack. The changes in optical properties after exposure to each process reveals the durability of the sputtered NiCr.

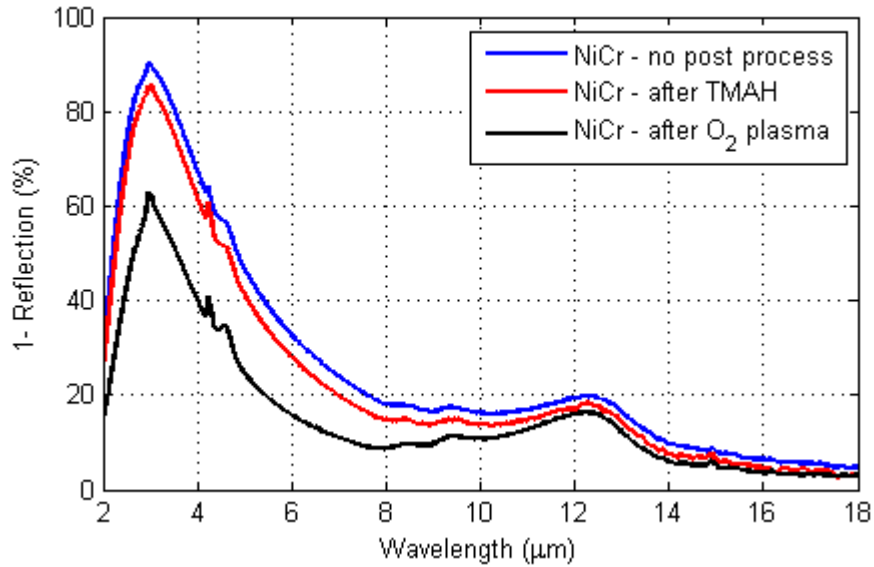


Figure 5.3: Measured FTIR spectra of Au/SiN/NiCr stack before and after being exposed to TMAH release procedure as well as 10 min of oxygen plasma.

It is evident that the umbrella layer release process in oxygen plasma that lasts about 40 minutes will endanger the optical response of the system, most probably due to oxygenation of chrome atoms in NiCr alloy. Therefore, a wafer level sputtering of NiCr after a wafer level oxygen plasma release of the umbrella layer is possible. Following, a TMAH release of the pixels in wafer level is conceivable since the NiCr deposition is performed *a priori*.

As future work that is considered to build upon the established research henceforth, plasmonic integration is a desired subject. Mitsubishi, recently reported plasmonic absorbers that are integrated into umbrella type absorbers on SOI-diode uncooled FPAs [112]. Although shaping the infrared response in narrow bandwidth to obtain multi-color applications are aimed, plasmonic integration is also proven to have broadband applications through singular [107-109] or multiplexed structures on a unit cell [114-118]. Therefore, it is possible to obtain desired infrared response (broadband or narrowband) through integrating patterned metallic structures into SiN dielectric umbrella layer.

In conclusion, this study presents the design and implementation steps of high fill factor structures onto SOI diode uncooled microbolometer FPAs developed by previous studies. The performance enhancement by the contribution of umbrella structures are evaluated, and alternative future works are presented.

REFERENCES

- [1] A. Rogalski, "History of infrared detectors," *Opto-Electronics Review*, vol. 20, pp. 279-308, 2012.
- [2] T. B. Breen, N. R. Butler, M. Kohin, C. A. Marshall, R. Murphy, T. W. Parker, *et al.*, "More applications of uncooled microbolometer sensors," *SPIE's International Symposium on Optical Science, Engineering, and Instrumentation*, 1998, pp. 530-540.
- [3] M. Diakides, J. D. Bronzino, and D. R. Peterson, *Medical Infrared Imaging: Principles and Practices*: CRC press, 2012.
- [4] E. Ring and K. Ammer, "Infrared thermal imaging in medicine," *Physiological measurement*, vol. 33, p. R33, 2012.
- [5] L. Becker, "Influence of IR sensor technology on the military and civil defense," *Integrated Optoelectronic Devices 2006*, 2006, pp. 61270S-61270S-15.
- [6] A. L. Bingham, P. G. Lucey, J. T. Akagi, J. L. Hinrichs, and E. T. Knobbe, "LWIR hyperspectral micro-imager for detection of trace explosive particles," *SPIE Sensing Technology+ Applications*, 2014, pp. 91010Z-91010Z-7.
- [7] A. Whittam, R. Simpson, and H. McEvoy, "Performance tests of thermal imaging systems to assess their suitability for quantitative temperature measurements," qirt.ge.ulaval.ca/archives/qirt2014/QIRT%20202014%20Papers/QIRT-2014-202.pdf [June 28, 2015].
- [8] R. Vadivambal and D. S. Jayas, "Applications of thermal imaging in agriculture and food industry—a review," *Food and Bioprocess Technology*, vol. 4, pp. 186-199, 2011.
- [9] I. B. Pečur and B. Milovanović, "Detecting defects in reinforced concrete using the method of infrared thermography," *CrSNDT Journal*, vol. 1, pp. 3-13, 2014.
- [10] B. C. Arrue, A. Ollero, and J. De Dios, "An intelligent system for false alarm reduction in infrared forest-fire detection," *Intelligent Systems and their Applications, IEEE*, vol. 15, pp. 64-73, 2000.

- [11] A. Rogalski, "Infrared detectors: status and trends," *Progress in quantum electronics*, vol. 27, pp. 59-210, 2003.
- [12] Y. R. Sivathanu and L. K. Tseng, "Fire detection using time series analysis of source temperatures," *Fire Safety Journal*, vol. 29, pp. 301-315, 11// 1997.
- [13] A. Rogalski, "Infrared detectors: an overview," *Infrared Physics & Technology*, vol. 43, pp. 187-210, 2002.
- [14] M. Foote, M. Kenyon, T. Krueger, T. McCann, R. Chacon, E. Jones, *et al.*, "Thermopile detector arrays for space science applications," *Proceedings of the International Workshop on Thermal Detectors for Space Based Planetary, Solar, and Earth Science Applications*, 2003, pp. 2-16.
- [15] A. Schaufelbühl, "Thermal imagers in CMOS technology," *PhD. Dissertation*, Naturwissenschaften Swiss Federal Institute of Technology (ETH), 2002.
- [16] F. Niklaus, C. Vieider, and H. Jakobsen, "MEMS-based uncooled infrared bolometer arrays: a review," *Photonics Asia 2007*, 2007, pp. 68360D-68360D-15.
- [17] A. Rogalski, *Infrared detectors*: CRC Press, 2010.
- [18] R. K. Willardson, E. R. Weber, D. D. Skatrud, and P. W. Kruse, *Uncooled infrared imaging arrays and systems* vol. 47: Academic press, 1997.
- [19] P. W. Kruse, *Uncooled thermal imaging: arrays, systems, and applications* vol. 2003: SPIE press Bellingham, WA, 2001.
- [20] M. A. Kinch, *Fundamentals of infrared detector materials* vol. 76: SPIE press, 2007.
- [21] M. Henini and M. Razeghi, *Handbook of infra-red detection technologies*: Elsevier, 2002.
- [22] M. Y. Tanrikulu, "An Uncooled Infrared Microbolometer Array Using Surface Micromachined MEMS Technology," *Ph.D. Dissertation*, Electrical and Electronics Department, Middle East Technical University, Ankara, 2007.
- [23] M. Kohli, C. Wuethrich, K. Brooks, B. Willing, M. Forster, P. Muralt, *et al.*, "Pyroelectric thin-film sensor array," *Sensors and Actuators A: Physical*, vol. 60, pp. 147-153, 1997.
- [24] P. Muralt, "Micromachined infrared detectors based on pyroelectric thin films," *Reports on Progress in Physics*, vol. 64, p. 1339, 2001.
- [25] R. Hartmann and M. Selders, "High-sensitivity thin-film bolometers," *Sensor'82- Sensor technology and temperature measurement*, pp. 102-116, 1982.

- [26] R. A. Wood, "Uncooled thermal imaging with monolithic silicon focal planes," *SPIE's 1993 International Symposium on Optics, Imaging, and Instrumentation*, 1993, pp. 322-329.
- [27] E. Mottin, J.-L. Martin, J.-L. Ouvrier-Buffet, M. Vilain, A. Bain, J.-J. Yon, *et al.*, "Enhanced amorphous silicon technology for 320 x 240 microbolometer arrays with a pitch of 35 μm ," *Aerospace/Defense Sensing, Simulation, and Controls*, 2001, pp. 250-256.
- [28] J. Yon, A. Astier, S. Bisotto, G. Chamingis, A. Durand, J. Martin, *et al.*, "First demonstration of 25 μm pitch uncooled amorphous silicon microbolometer IRFPA at LETI-LIR," *Defense and Security*, 2005, pp. 432-440.
- [29] M. Moreno, R. Jimenez, A. Torres, and R. Ambrosio, "Microbolometers Based on Amorphous Silicon-Germanium Films With Embedded Nanocrystals," 2015.
- [30] P. De Moor, J. John, S. Sedky, and C. A. Van Hoof, "Linear arrays of fast uncooled poly-SiGe microbolometers for IR detection," *AeroSense 2000*, 2000, pp. 27-34.
- [31] L. Dong, R. Yue, and L. Liu, "An uncooled microbolometer infrared detector based on poly-SiGe thermistor," *Sensors and Actuators A: Physical*, vol. 105, pp. 286-292, 2003.
- [32] V. N. Leonov, N. A. Perova, J. P. Vermeiren, B. Grietens, C. Goessens, P. De Moor, *et al.*, "Optimization of design and technology for uncooled poly-SiGe microbolometer arrays," *AeroSense 2002*, 2002, pp. 122-133.
- [33] M. Almasri, D. P. Butler, and Z. Celik-Butler, "Self-supporting uncooled infrared microbolometers with low-thermal mass," *Microelectromechanical Systems, Journal of*, vol. 10, pp. 469-476, 2001.
- [34] M. F. Almasri, D. P. Butler, and Z. Celik-Butler, "Semiconducting YBCO bolometers for uncooled IR detection," *AeroSense 2000*, 2000, pp. 17-26.
- [35] S. E. Kucuk, "Development of High Fill Factor Uncooled Infrared Detector Pixels," *M.Sc. Thesis*, Electrical and Electronics Department, Middle East Technical University, 2011.
- [36] A. M. Filachev, V. P. Ponomarenko, I. I. Taubkin, and M. B. Ushakova, "Infrared focal plane arrays: state of the art and development trends," 2003, pp. 52-85.
- [37] B. S. Backer, M. Kohin, A. R. Leary, R. J. Blackwell, and R. N. Rumbaugh, "Advances in uncooled technology at BAE systems," *AeroSense 2003*, 2003, pp. 548-556.

- [38] M. Kohin and N. R. Butler, "Performance limits of uncooled VOx microbolometer focal plane arrays," *Defense and Security*, 2004, pp. 447-453.
- [39] E. Mottin, A. Bain, J.-L. Martin, J.-L. Ouvrier-Buffet, S. Bisotto, J.-J. Yon, *et al.*, "Uncooled amorphous silicon technology enhancement for 25- μ m pixel pitch achievement," *International Symposium on Optical Science and Technology*, 2003, pp. 200-207.
- [40] D. F. Murphy, M. Ray, J. Wyles, J. F. Asbrock, C. Hewitt, R. Wyles, *et al.*, "Performance improvements for VOx microbolometer FPAs," *Defense and Security*, 2004, pp. 531-540.
- [41] R. Fraenkel, J. Haski, U. Mizrahi, L. Shkedy, I. Shtrichman, and E. Pinsky, "Cooled and uncooled infrared detectors for missile seekers," *SPIE Defense+ Security*, 2014, pp. 90700P-90700P-10.
- [42] D. Takamuro, T. Maegawa, T. Sugino, Y. Kosasayama, T. Ohnakado, H. Hata, *et al.*, "Development of new SOI diode structure for beyond 17 μ m pixel pitch SOI diode uncooled IRFPAs," *SPIE Defense, Security, and Sensing*, 2011, pp. 80121E-80121E-10.
- [43] S. Takasawa, "Uncooled LWIR imaging: applications and market analysis," *SPIE Sensing Technology+ Applications*, 2015, pp. 94810H-94810H-13.
- [44] S. Eminoglu, M. Y. Tanrikulu, and T. Akin, "A low-cost 128 128 uncooled infrared detector array in CMOS process," *Microelectromechanical Systems, Journal of*, vol. 17, pp. 20-30, 2008.
- [45] S. Eminoglu, D. S. Tezcan, M. Y. Tanrikulu, and T. Akin, "Low-cost uncooled infrared detectors in CMOS process," *Sensors and Actuators A: Physical*, vol. 109, pp. 102-113, 2003.
- [46] E. Inceturkmen, "A Low-cost 128x128 Uncooled Infrared Detector Array in a Standard SOI-CMOS Technology," *M.Sc. Thesis*, Electrical and Electronics Engineering, Middle East Technical University, 2008.
- [47] T. Ishikawa, M. Ueno, K. Endo, Y. Nakaki, H. Hata, T. Sone, *et al.*, "Low-cost 320x240 uncooled IRFPA using a conventional silicon IC process," *AeroSense'99*, 1999, pp. 556-564.
- [48] F. Tankut, "Deveopment and Characterization of Low-cost Uncooled Infrared Sensors For Commercial Applications," *M.Sc Thesis*, *M.Sc. Thesis*, Electrical and Electroncis Department, Middle East Technical University, Ankara, 2013.
- [49] T. Ishikawa, M. Ueno, Y. Nakaki, K. Endo, Y. Ohta, J. Nakanishi, *et al.*, "Performance of 320 x 240 uncooled IRFPA with SOI diode detectors," *International Symposium on Optical Science and Technology*, 2000, pp. 152-159.

- [50] M. Ueno, Y. Kosasayama, T. Sugino, Y. Nakaki, Y. Fujii, H. Inoue, *et al.*, “640 x 480 pixel uncooled infrared FPA with SOI diode detectors,” *Defense and Security*, 2005, pp. 566-577.
- [51] D. Sabuncuoglu Tezcan, S. Eminoglu, O. Sevket Akar, and T. Akin, “A low cost uncooled infrared microbolometer focal plane array using the CMOS n-well layer,” *Micro Electro Mechanical Systems, 2001. MEMS 2001. The 14th IEEE International Conference on*, 2001, pp. 566-569.
- [52] P. W. Norton, M. Kohin, M. Dovidio, and B. S. Backer, “Commercialization of uncooled infrared technology,” 2004, pp. 55-61.
- [53] M. Kimata, M. Ueno, M. Takeda, and T. Seto, “SOI diode uncooled infrared focal plane arrays,” *Integrated Optoelectronic Devices 2006*, 2006, pp. 61270X-61270X-11.
- [54] U. Bakshi and A. Godse, *Electronic Devices and Circuits: Technical Publications*, 2008.
- [55] D. Sabuncuoglu Tezcan, “A CMOS Compatible Uncooled Infrared Detector Focal Plane Array for Night Vision Applications Using MEMS Technology,” *Ph.D. Dissertation*, Electrical and Electronics Engineering Department, Middle East Technical University, 2002.
- [56] D. S. Tezcan, S. Eminoglu, and T. Akin, “A low-cost uncooled infrared microbolometer detector in standard CMOS technology,” *Electron Devices, IEEE Transactions on*, vol. 50, pp. 494-502, 2003.
- [57] S. Eminoglu, “Uncooled Infrared Focal Plane Arrays with Integrated Readout Circuitry Using MEMS and Standard CMOS Technologies,” *Ph.D. Dissertation*, Electrical and Electronics Engineering Middle East Technical University, 2003.
- [58] E. Alpman, “Development of Low-Cost Uncooled Infrared Detector Arrays in Standard CMOS and SOI-CMOS Processes,” *M.Sc. Thesis*, Electrical and Electronics Engineering Department Middle East Technical University, 2005.
- [59] M. B. Dayanik, “Low-Cost High Performance Infrared Detectors in SOI-CMOS Technology,” *M.Sc. Thesis*, Electrical and Electronics Engineering Department, Middle East Technical University, 2007.
- [60] D. Akcoren, “A Low-Cost Uncooled Infrared Detector Array and Its Camera Electronics,” *M.Sc. Thesis*, Electrical and Electronics Engineering Department, Middle East Technical University, 2011.
- [61] Y. Kosasayama, T. Sugino, Y. Nakaki, Y. Fujii, H. Inoue, H. Yagi, *et al.*, “Pixel scaling for SOI-diode uncooled infrared focal plane arrays,” *Defense and Security*, 2004, pp. 504-511.

- [62] D. Fujisawa, T. Maegawa, Y. Ohta, Y. Kosasayama, T. Ohnakado, H. Hata, *et al.*, “Two-million-pixel SOI diode uncooled IRFPA with 15 μ m pixel pitch,” *SPIE Defense, Security, and Sensing*, 2012, pp. 83531G-83531G-13.
- [63] W. Jiang, W. Ou, A. Ming, Z. Liu, and X. Zhang, “Design and analysis of a high fill-factor SOI diode uncooled infrared focal plane array,” *Journal of Micromechanics and Microengineering*, vol. 23, p. 065004, 2013.
- [64] Y. Lv, W. Jiang, and W. Ou, “Study of a Novel FP Microcavity With High Infrared Absorption,” *Sensors Journal, IEEE*, vol. 15, pp. 1756-1760, 2015.
- [65] C. Li, G. D. Skidmore, C. Howard, C. Han, L. Wood, D. Peysha, *et al.*, “Recent development of ultra small pixel uncooled focal plane arrays at DRS,” *Defense and Security Symposium*, 2007, pp. 65421Y-65421Y-12.
- [66] G. D. Skidmore and C. G. Howard, “Pixel structure having an umbrella type absorber with one or more recesses or channels sized to increase radiation absorption,” 2009.
- [67] G. D. Skidmore, C. Han, and C. Li, “Uncooled microbolometers at DRS and elsewhere through 2013,” *SPIE Sensing Technology+ Applications*, 2014, pp. 910003-910003-5.
- [68] S. Tohyama, M. Miyoshi, S. Kurashina, N. Ito, T. Sasaki, A. Ajisawa, *et al.*, “New thermally isolated pixel structure for high-resolution (640 \times 480) uncooled infrared focal plane arrays,” *Optical Engineering*, vol. 45, pp. 014001-014001-10, 2006.
- [69] M. J. Modarres-Zadeh and R. Abdolvand, “High-responsivity thermoelectric infrared detectors with stand-alone sub-micrometer polysilicon wires,” *Journal of Micromechanics and Microengineering*, vol. 24, p. 125013, 2014.
- [70] M. J. Modarres-Zadeh and R. Abdolvand, “A low-noise silicon-based 20 μ m*20 μ m uncooled thermoelectric infrared detector,” *SPIE Defense, Security, and Sensing*, 2013, pp. 87041R-87041R-8.
- [71] S.-B. Ju, Y.-J. Yong, and S.-G. Kim, “Design and fabrication of a high-fill-factor microbolometer using double sacrificial layers,” *AeroSense'99*, 1999, pp. 180-189.
- [72] D. Murphy, M. Ray, J. Wyles, C. Hewitt, R. Wyles, E. Gordon, *et al.*, “640 \times 512 17 μ m microbolometer FPA and sensor development,” 2007, pp. 65421Z-65421Z-10.
- [73] M. J. Madou, *Fundamentals of microfabrication: the science of miniaturization*: CRC press, 2002.

- [74] A. Tarraf, J. Daleiden, S. Irmer, D. Prasai, and H. Hillmer, "Stress investigation of PECVD dielectric layers for advanced optical MEMS," *Journal of Micromechanics and Microengineering*, vol. 14, p. 317, 2004.
- [75] H. Huang, K. Winchester, Y. Liu, X. Hu, C. Musca, J. Dell, *et al.*, "Determination of mechanical properties of PECVD silicon nitride thin films for tunable MEMS Fabry–Perot optical filters," *Journal of Micromechanics and Microengineering*, vol. 15, p. 608, 2005.
- [76] J. Laconte, D. Flandre, and J.-P. Raskin, *Micromachined thin-film sensors for SOI-CMOS co-integration*: Springer Science & Business Media, 2006.
- [77] J. Singh, S. Chandra, and A. Chand, "Strain studies in LPCVD polysilicon for surface micromachined devices," *Sensors and Actuators A: Physical*, vol. 77, pp. 133-138, 1999.
- [78] V. Lindroos, S. Franssila, M. Tilli, M. Paulasto-Krockel, A. Lehto, T. Motooka, *et al.*, *Handbook of silicon based MEMS materials and technologies*: Elsevier, 2009.
- [79] D. Grbovic, N. V. Lavrik, S. Rajic, and P. G. Datskos, "Arrays of SiO₂ substrate-free micromechanical uncooled infrared and terahertz detectors," *Journal of applied physics*, vol. 104, p. 054508, 2008.
- [80] K. J. Winchester and J. M. Dell, "Tunable Fabry-Pérot cavities fabricated from PECVD silicon nitride employing zinc sulphide as the sacrificial layer," *Journal of Micromechanics and Microengineering*, vol. 11, p. 589, 2001.
- [81] R. R. Davies, M. E. McNie, K. M. Brunson, and D. Combes, "Engineering in- and out-of-plane stress in PECVD silicon nitride for CMOS-compatible surface micromachining," 2001, pp. 320-328.
- [82] H. Tompkins, "WVASE32 Software Training Manual, JA Woollam Co," *Inc., Lincoln, NE, USA*, vol. 210, 2006.
- [83] H. Tompkins and E. A. Irene, *Handbook of ellipsometry*: William Andrew, 2005.
- [84] J. Kischkat, S. Peters, B. Gruska, M. Semtsiv, M. Chashnikova, M. Klinkmüller, *et al.*, "Mid-infrared optical properties of thin films of aluminum oxide, titanium dioxide, silicon dioxide, aluminum nitride, and silicon nitride," *Applied optics*, vol. 51, pp. 6789-6798, 2012.
- [85] K. O. Bugaev, A. A. Zelenina, and V. A. Volodin, "Vibrational spectroscopy of chemical species in silicon and silicon-rich nitride thin films," *International Journal of Spectroscopy*, vol. 2012, 2011.
- [86] S. Zhou, W. Liu, C. Cai, and H. Liu, "Comparative investigation of infrared optical absorption properties of silicon oxide, oxynitride and nitride films,"

Seventh International Conference on Thin Film Physics and Applications, 2010, pp. 79950T-79950T-4.

- [87] H. Nagel, A. G. Aberle, and R. Hezel, "Optimised antireflection coatings for planar silicon solar cells using remote PECVD silicon nitride and porous silicon dioxide," *Progress in Photovoltaics: Research and Applications*, vol. 7, pp. 245-260, 1999.
- [88] Y. Wang, X. Cheng, Z. Lin, C. Zhang, and F. Zhang, "Optimization of PECVD silicon oxynitride films for anti-reflection coating," *Vacuum*, vol. 72, pp. 345-349, 2003.
- [89] G. Kang, I. Vartiainen, B. Bai, and J. Turunen, "Enhanced dual-band infrared absorption in a Fabry-Perot cavity with subwavelength metallic grating," *Optics express*, vol. 19, pp. 770-778, 2011.
- [90] G. Hernandez, "Fabry-Perot with an absorbing etalon cavity," *Applied optics*, vol. 24, pp. 3062-3067, 1985.
- [91] S. Shu, Z. Li, and Y. Y. Li, "Triple-layer Fabry-Perot absorber with near-perfect absorption in visible and near-infrared regime," *Optics express*, vol. 21, pp. 25307-25315, 2013.
- [92] H. Zheng, X. Jin, J. Park, Y. Lu, J. Y. Rhee, W. Jang, *et al.*, "Tunable dual-band perfect absorbers based on extraordinary optical transmission and Fabry-Perot cavity resonance," *Optics express*, vol. 20, pp. 24002-24009, 2012.
- [93] P. Eriksson, J. Y. Andersson, and G. Stemme, "Thermal characterization of surface-micromachined silicon nitride membranes for thermal infrared detectors," *Microelectromechanical Systems, Journal of*, vol. 6, pp. 55-61, 1997.
- [94] J. Kuntner, A. Jachimowicz, F. Kohl, and B. Jakoby, *Determining the thin-film thermal conductivity of low temperature PECVD silicon nitride: na*, 2006.
- [95] S. M. Lee and D. G. Cahill, "Heat transport in thin dielectric films," *Journal of applied physics*, vol. 81, pp. 2590-2595, 1997.
- [96] M. Von Arx, O. Paul, and H. Baltes, "Process-dependent thin-film thermal conductivities for thermal CMOS MEMS," *Microelectromechanical Systems, Journal of*, vol. 9, pp. 136-145, 2000.
- [97] X. Zhang and C. P. Grigoropoulos, "Thermal conductivity and diffusivity of free-standing silicon nitride thin films," *Review of Scientific Instruments*, vol. 66, pp. 1115-1120, 1995.
- [98] B. Zink and F. Hellman, "Specific heat and thermal conductivity of low-stress amorphous Si-N membranes," *Solid State Communications*, vol. 129, pp. 199-204, 2004.

- [99] S. Keskin, "A Two-Color Uncooled Infrared Microbolometer Detector with a Tunable Micro-Mirror," *M.Sc. Thesis*, Electrical and Electronics Engineering, Middle East Technical University, 2012.
- [100] E. S. Awad, N. Al-Khalli, M. Abdel-Rahman, M. Alduraibi, and N. Debbar, "Comparison of V₂O₅ Microbolometer Optical Performance Using NiCr and Ti Thin-Films," *Photonics Technology Letters, IEEE*, vol. 27, pp. 462-465, 2014.
- [101] J. Gou, J. Wang, W. Li, H. Tai, D. Gu, and Y. Jiang, "Terahertz Absorption Characteristics of NiCr Film and Enhanced Absorption by Reactive Ion Etching in a Microbolometer Focal Plane Array," *Journal of Infrared, Millimeter, and Terahertz Waves*, vol. 34, pp. 431-436, 2013.
- [102] M. Schossig, V. Norkus, and G. Gerlach, "Infrared responsivity of pyroelectric detectors with nanostructured NiCr thin-film absorber," *Sensors Journal, IEEE*, vol. 10, pp. 1564-1565, 2010.
- [103] A. M. Kennedy and S. H. Black, "Perforated bolometer pixel structure with reduced vacuum requirements," ed: Google Patents, 2013.
- [104] A. Kennedy, P. Masini, M. Lamb, J. Hamers, T. Kocian, E. Gordon, *et al.*, "Advanced uncooled sensor product development," *SPIE Defense+ Security*, 2015, pp. 94511C-94511C-10.
- [105] N. Eigenfeld, J. Gray, J. Gertsch, G. Skidmore, S. George, and V. Bright, "Specific heat capacity of ultra-thin atomic layer deposition nanobridges for microbolometers," *Solid-State Sensors, Actuators and Microsystems (TRANSDUCERS), 2015 Transducers-2015 18th International Conference on*, 2015, pp. 1385-1388.
- [106] E. M. Smith, D. Panjwani, J. Ginn, A. Warren, C. Long, P. Figuieredo, *et al.*, "Enhanced performance of VO_x-based bolometer using patterned gold black absorber."
- [107] A. Bonakdar and H. Mohseni, "Impact of optical antenna and plasmonics on infrared imagers," *Infrared Physics & Technology*, vol. 59, pp. 142-145, 2013.
- [108] O. Erturk, E. Battal, S. E. Kucuk, A. K. Okyay, and T. Akin, "A plasmonically enhanced pixel structure for uncooled microbolometer detectors," *SPIE Defense, Security, and Sensing*, 2013, pp. 87041E-87041E-7.
- [109] H.-S. Park, S. H. Nam, H.-G. Hong, S. Roh, S. Yun, J. Kim, *et al.*, "Newly developed broadband plasmonic absorber for uncooled infrared detectors," *SPIE MOEMS-MEMS*, 2014, pp. 89770I-89770I-6.
- [110] F. Utermohlen, D. B. Etter, D. Borowsky, I. Herrmann, C. Schelling, F. X. Hutter, *et al.*, "Low-cost microbolometer with nano-scaled plasmonic absorbers for far infrared thermal imaging applications," *Micro Electro*

- Mechanical Systems (MEMS), 2014 IEEE 27th International Conference on*, 2014, pp. 572-575.
- [111] S. Ogawa, D. Fujisawa, and M. Kimata, "Three-dimensional plasmonic metamaterial absorbers based on all-metal structures," *SPIE Defense+ Security*, 2015, pp. 94511J-94511J-6.
- [112] D. Fujisawa, S. Ogawa, H. Hata, M. Uetsuki, K. Misaki, Y. Takagawa, *et al.*, "Multi-color imaging with silicon-on-insulator diode uncooled infrared focal plane array using through-hole plasmonic metamaterial absorbers," *Micro Electro Mechanical Systems (MEMS), 2015 28th IEEE International Conference on*, 2015, pp. 905-908.
- [113] M. Y. Tanrikulu, F. Civitci, and T. Akin, "A new method to estimate the absorption coefficient for uncooled infrared detectors," *SPIE Defense and Security Symposium*, 2008, pp. 694027-694027-7.
- [114] J. Hendrickson, J. Guo, B. Zhang, W. Buchwald, and R. Soref, "Wideband perfect light absorber at midwave infrared using multiplexed metal structures," *Optics letters*, vol. 37, pp. 371-373, 2012.
- [115] H. Luo, Y. Cheng, and R. Gong, "Numerical study of metamaterial absorber and extending absorbance bandwidth based on multi-square patches," *The European Physical Journal B*, vol. 81, pp. 387-392, 2011.
- [116] W. Ma, S. Wang, Y. Wen, Y. Zhao, L. Dong, M. Liu, *et al.*, "Uncooled multi-band IR imaging using bimaterial cantilever FPA," *Micro Electro Mechanical Systems (MEMS), 2014 IEEE 27th International Conference on*, 2014, pp. 1225-1228.
- [117] W. Ma, Y. Wen, and X. Yu, "Broadband metamaterial absorber at mid-infrared using multiplexed cross resonators," *Optics express*, vol. 21, pp. 30724-30730, 2013.
- [118] B. Zhang, J. Hendrickson, and J. Guo, "Multispectral near-perfect metamaterial absorbers using spatially multiplexed plasmon resonance metal square structures," *JOSA B*, vol. 30, pp. 656-662, 2013.